Modeling Leakage Losses and Axial Thrust in Rocket Engine Turbopumps

Jonathan Gloger

Development of a numerical model

Modeling Leakage Losses and Axial Thrust in Rocket Engine Turbopumps

by

Jonathan Gloger

to obtain the degree of Master of Science
at the Delft University of Technology,
to be defended publicly on Friday August 31, 2018 at 15:00 AM.

Student number:	4522923	
Project duration:	August 1, 2017 – August, 2018	
Supervisors:	Dr. ir. Matteo Pini	TU Delft
	Dr. ir. Claudio Lettieri	TU Delft
	Dr. Louis Souverein	ArianeGroup GmbH

TU Delft

Abstract

Large-scale liquid rocket engines require high-speed turbopumps to inject cryogenic propellants into the combustion chamber. Modeling the impact of secondary path and leakage flows on the performance and axial thrust of the pump is critical during the early design phase. Previous studies derived simplified models and empirical correlations to model leakage loss and determine the pressure distribution in the side gaps. The prediction capabilities of these models are subject to limitations and uncertainties mainly due to the interaction between impeller exit flow and sidewall gaps especially at partload operation. The effects of the leakage injection on the impeller flow are not fully understood and not captured by analytical correlations from literature. These can have destabilizing and detrimental effects on the hydraulic performance and the head curve, leading to a divergence between model predictions and experimental results.

In this project a reduced order model is developed to capture the effects of the sidewall gaps on turbopump performance and determine the axial thrust on the rotor. High fidelity calculations of the pump and volute are performed to identify the key physical mechanisms associated with loss generation in leakage paths and improve upon existing analytical models found in literature. Axial thrust and leakage losses are modeled numerically with a single passage geometry to capture the interaction of impeller flow and leakage flow through the side gaps at multiple operating points.

It is found that the recirculation of pressurized fluid, leakage mass flow, is the most impactful effect on the performance. The volumetric efficiency is captured within 16% with the analytical model and 6% with the single passage numerical calculations at nominal operation. At partload operation however, the accuracy of both models reduces. Disk friction is under predicted by the investigated analytical model and axial thrust is over predicted. For both effects the reduced numerical model shows promising results that improve the prediction capability around nominal operation and offer a higher flexibility required for the early design phase as compared with the high fidelity, full annulus calculations. For the investigated cases the leakage injection to the impeller flow does not show a destabilizing impact on the characteristic behavior.

Preface

In the course of my project with the ArianeGroup GmbH and the TU Delft I received help and support from many sides. I want to start and thank my supervisor from Delft University Dr. ir. Claudio Lettieri who referred me to the ArianeGroup in Munich and who supported me closely during the whole period of the project. The experiences and learings made at ArianeGroup have helped me grow to become an engineer. I want to thank Dr. Louis Souverein for all his support and help as well as Josef Goergen who supported me especially on the numerical methods. My colleague students whom I shared an office with were extremely supportive and helpful on a daily basis. Special thanks to Can Araz and Stefan Zeller with whom I spent the largest part of my project period with and who helped me with numerical simulations, programming and with their good experience and knowledge on radial machinery. Michael Reichl and Nicklas Pflueger constantly helped me in the process as well. Luisa Prasch was supporting me throughout the project during the time at ArianeGroup and afterwards. Even though she constantly blocked my CFD-licenses she is the best thing that happened to me during my time in Munich.
My fellow students Hugo Bento, Jaydeep Koradiya, Sagarika Banerji, Kaushik Radhakrishnan and Marco Palermo were supportive from distance in Delft. After all I had a very exciting but also demanding period in which I was lucky enough to meet many supportive and inspiring people, some of which I am happy to consider as friends now. Special thanks to my family who were always giving me support and motivation to focus on the tasks at hand and without whom I could not have studied at Delft University of Technology.

Jonathan Gloger
Delft, August 2018

Contents

List of Tables

List of Figures

Nomenclature

Greek Letters

α	Flow angle in stationary frame
β	Flow angle in rotating frame
β	Fluid rotational speed
δ	Angle at wall
η	Efficiency
λ	Friction coefficient
ν	Dynamic viscosity
ω	Angular rotor velocity
ϕ	Flow coefficient
Ψ	Head coefficient
ρ	Density
σ	Slip factor
τ	Shear stress
θ^*	Momentum thickness
ζ	Loss coefficient (Denton & Gülich)

Roman Letters

b_c	Coriolis acceleration
b_z	Centrifugal acceleration
c	Velocity in stationary frame
c_d	Dissipation coefficient
c_f	Friction coefficient
c_p	Pressure coefficient
$C_{f,W/R}$	Ratio of friction coefficients
d	Diameter
F	Force
f	Loss coefficient (Brennen)
g	Gravitational constant
H	Enthalpy
H	Head

k	Rotation factor
L	Reference Length
l	Seal length
M	Torque
N	Number of blades
n	Rotational speed [rev/min]
P	Power
p	Pressure
P_{RR}	Disk friction power
Q	Volumetric flow rate
r	Radius
Ro	Rossby number
S	Entropy
s	Seal width
s	solidity
U	Reference velocity
u	Circumferential velocity
W	Width of channel
w	Velocity in rotating frame
x	Distance
Y	Specific work

Subscripts

Q_1	Location: impeller entrance
Q_2	Location: impeller exit
Q_i	Inlet
Q_M	Mean
Q_m	Meridional
Q_u	Circumferential
Q_{ax}	Axial
Q_E	Free stream
Q_{inc}	Incidence
Q_{La}	Impeller
Q_R	Rotor
Q_{shaft}	Shaft

Q_{sl}	Streamline
Q_{sp}	Seal
Q_{stat}	Static
Q_{th}	theoretical (mostly referring to Euler's turbine equation)
Q_{tot}	Total
Q_W	Wall

1 Introduction

1.1. Motivation

Turbopumps are key components in liquid propellant rocket engines. They are necessary to attain high combustion chamber pressures at low tank pressure. Knowledge on their behavior in nominal and off-design load points contributes to the optimization of the engine performance and hence reduced propellant consumption and increased partial payload [5].

The application in rocket engines entails a list of specific requirements some of which are: low mass and small geometry but high power levels and high efficiencies. The pumped media bring further challenges to the design of the pumping system. Especially the sealing components face high requirements with low temperature propellants and hot turbine gases on high rotational speeds [24]. The low lubrication characteristics of cryogenic fuels and oxidizers in combination with high numbers of revolutions poses strains on bearings. Axial forces on the rotor furthers the strain. The major reason for axial thrust on the rotor is the different pressure force generated in the clearances between radial impellers and their casing [21]. The correct modeling of these forces can therefore help speeding up the design process in early stages and lead to an improved reliability and longer service life which gains significance due to the current trend towards reusable rocket engines in the space propulsion industry.

The flow behavior in these impeller sidewall gaps is governed by the rotation of the shrouds and the through-flow that occurs due to leakage flow from high to low pressure regions around the impeller. The leakage flow causes performance reductions and changes in behavior of the pump at design and off-design operation. Especially at low flow coefficients which are typical of turbopumps in rocket engines the losses due to leakage have an increased impact on the performance [22]. During the design process the sidewall gaps need to be considered for performance estimations and thrust balancing. The leakage mass flow through the sealing gaps increases the effective mass flow of the main pump component which should be taken into account when optimizing the passage design for nominal operation. The correct modeling of the loss mechanisms in secondary flow paths and understanding of the effects on the hydraulic performance helps improving the pump design towards higher efficiencies.

1.2. Scope of research

At first a review of the relevant literature is carried out to investigate the existing models presented in literature. In order to achieve the research objective which is to understand the key mechanisms of losses and thrust in turbopumps for rocket engines and to identify the common models for losses and thrust along with the remaining uncertainties, several research questions can be developed.

- **"Which are the existing models for axial thrust and losses due to secondary flow paths in turbopumps and how well can the effects be captured?"**
- What are main loss mechanisms in turbopumps and how are losses determined?
- What are the secondary losses due to leakage flow paths and how are losses determined and dissected?
- How are the existing loss and thrust models built up and what are the remaining uncertainties for the individual effects emphasized in literature?

After identifying the main loss mechanism the questions of the individual modeling and determination of loss come up.

The loss mechanisms due to leakage are often differentiated between disk friction losses and leakage losses. "However, a close interaction is in effect between the main flow at the impeller outlet, the flow in the impeller sidewall gaps, leakage through annular seals and the disk friction losses. The interaction is difficult to capture either experimentally or numerically" [21].

Based on the literature research the thesis project aims to investigate the effect of secondary flows on pump performance and axial thrust in more detail, dissecting the loss mechanisms due to secondary flow paths. Quantifying the losses based on numerical high fidelity simulations will give answer to the question of how the individual losses scale. The project objective will be to develop a reduced order numerical model that captures the effects of the impeller sidewall gaps on losses and thrust with an improved accuracy when compared to existing empirical models. It is build to allow for estimations of the effects at early stages of the design phase. To reduce the scope of the project to be suitable to a master's project the models and the investigated effects shall be only applied to pumps of the following type:

Table 1.1: Pump type

Component or feature	Type
Impeller	radial & shrouded
Collector	single volute
Leakage direction	inwards
Balancing measures	balance holes
Seal	ring seal

Furthermore the investigated operation will cover a limited range of conditions mostly ranging from 50 % to 150 % of the nominal mass flow. The conclusions and analysis will mostly be based on numerical results only. A very limited amount of experimental data are available for the investigated pumps which cover the global performance parameters. The example designs and the experimental test data are provided by the *ArianeGroup GmbH*.

1.3. Structure of the report

The structure of the project report is presented in this section. After the introductory sections which point out the motivation and the scope of the research the report briefly introduces to fundamental flow mechanisms of radial turbopumps. Conventions that are used in the report are presented 2.1, followed by an introduction into the basic flow mechanics of radial turbopumps 2.2. The section is then followed by an introduction into typical pump characteristics and the main mechanisms that impact the pump behavior 2.3. The following section then deals with losses and loss accounting in turbopumps 2.4. The focus here is on hydraulic losses. The main loss mechanisms, which are friction losses and losses due to flow non-uniformities, are introduced. How the losses can be determined and quantified is presented and a third subsection focuses on loss accounting in the impeller which is generally the component where most of the useful work is created. The next section 2.5 deals with the common averaging methods that are used to determine performance and losses from experimental or numerical test data.

Chapter 3 deals with losses that are directly linked to secondary flow paths. In the first section the common flow field in the side gaps is introduced with the main parameters that impact the flow behavior found in literature.

Chapter 4 deals with modeling approaches in literature of the loss mechanisms mentioned in chapter 2 and 3 focusing on the modeling on the losses associated with secondary flow paths. In chapter 5 the effect of the side cavities on the axial force on the shaft is explained along with the current model to assess the forces analytically.

The main conclusions that can be drawn from the literature review are presented in chapter 6.

Based on the findings from literature study, research questions and the project objectives along with the research plan are presented in section 7.1. The next section 7.2 focuses on the methods applied to follow the research plan. Here the mesh generation and the meshes of the individual models and their components are presented. The setup in the pre-processing tool *ANSYS CFX-Pre* and the analysis methods of the numerical results are also presented.

The following chapters present the results of the investigations. In order to build up understanding for the specific pumps and their behavior the baseline full annulus simulations are presented first and then followed by the secondary flow specific losses and thrust generated in chapter 8. The losses are quantified and their scaling presented in a conclusive section for the baseline investigations.

The next chapter 9 presents the results of the impeller model focusing on the individual loss mechanisms associated with the secondary flow paths.

In order to check whether the new numerical model is improving upon the existing model, analytical models are established based on the most common models in literature mainly presented in [21] . The program structure is presented which is then followed by the results from the analytical models applied on the investigated pumps in chapter 10.

The results of the three different models are compared in the key chapter 11. Here the focus will be on the different loss mechanisms and how well these are captured with the analytical and numerical models referring to the baseline simulations of the full-annulus model. The limitations of the methods applied along with the summary of the effects and their accuracy in a key-chart follows in a section 11.3.

Based on the findings in the first pump's analysis the initial design of the sidewall gaps in a second pump was developed. The results are presented in chapter 12.

The conclusions for the project goal are presented in chapter 13. The chapter also contains a section on the recommendations for setting up pump simulations based on the experiences gained in the course of the project. A last section presents the recommendations for following and further research in the field of secondary flow paths around shrouded impellers and their loss and thrust modeling.

2

Fundamentals of Turbopumps

This chapter deals with the fundamentals of radial turbopumps, presenting the most common flow phenomena in radial impellers and the loss mechanisms in turbopumps that effect the performance behavior of the machine. The characteristic performance parameters are introduced. The methods to quantify losses in turbopumps from test data are presented in chapter 2.4.

2.1. Conventions and subscripts

For a better understanding of the formula and concepts presented the subscripts and conventions need to be defined which are used in the course of the project. Since many principles presented are based on the book of Johann Friedrich Gülich, Centrifugal Pumps (2010) [21], it is reasonable to use his conventions. Figure 2.1 shows a meridional view of a radial impeller with sidewall gaps. The pump type displayed matches the description in section 1.2. Properties at the entrance of the impeller are labeled with the index i_1 and at the exit i_2. Properties referring to the seals of the side cavities are labeled with the index i_{sp}.

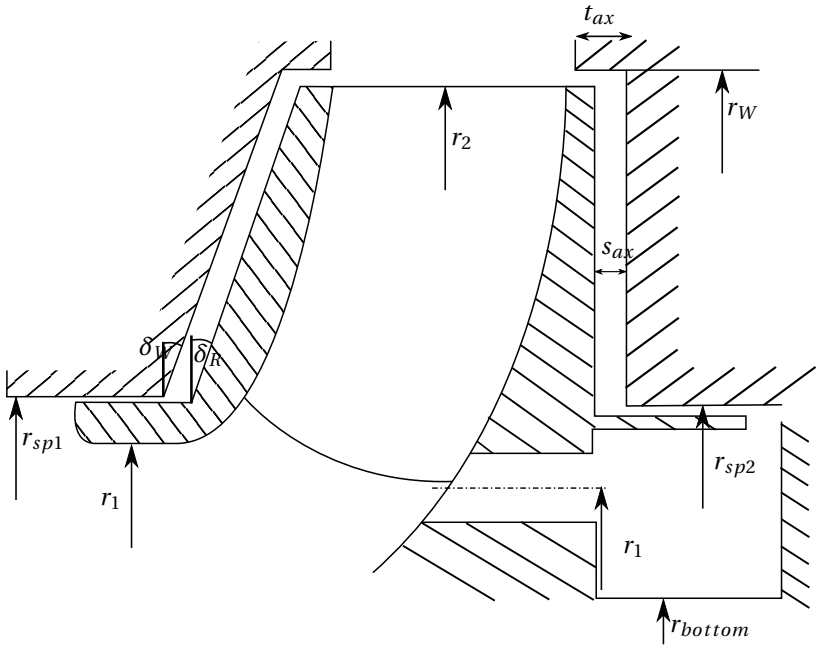

Figure 2.1: Meridional view and geometry definition

Flow velocities in rotating passages are often presented in two different reference frames. The different velocity vectors can best be visualized by developing them on a schematic impeller blade. The velocities have circumferential and meridional components. The following figure shows the velocity triangles and the meridional cross section of an impeller blade according to the definitions used in this research project 2.2.

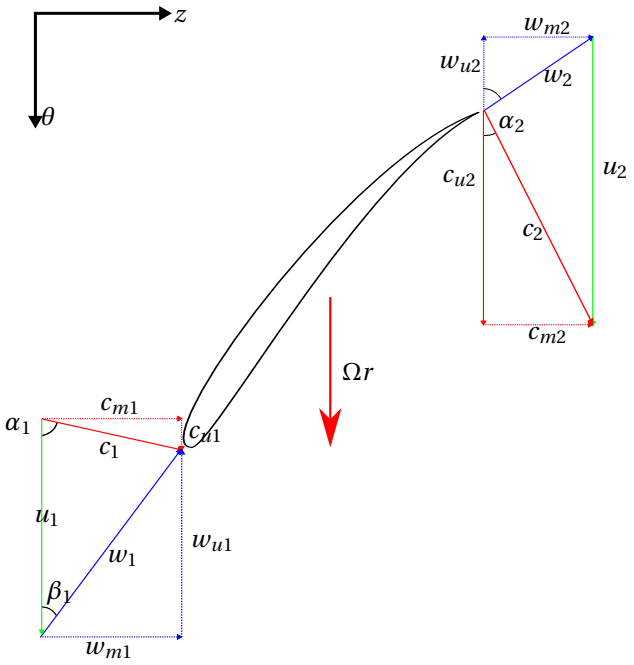

Figure 2.2: Velocity triangles

The following conventions are taken into account:

- The rotational velocities $\vec{u}_1$ and $\vec{u}_2$ point in the positive rotational direction which defines the positive direction for all the vectors.
- The angles α and β are defined as the angle between rotation direction and the velocity in stationary frame and relative respectively.
- The meridional velocity component $\vec{c_m}$ points in the perpendicular direction to the rotation direction and points in positive direction.
- In this schematic figure the blade is aligned to the velocity in rotating frame of reference at inlet and exit of the blade passage, in reality most cases feature a difference in approach angle and blade angle also called slip angle or incidence angle which are defined in the following sections.
- In radial pumps the circumferential speed increases from inlet to outlet leading to an increased circumferential flow in stationary frame of reference.

2.2. Basic flow mechanics of turbopumps

Radial turbopumps are used for the transport and the increase in pressure level of fluids, consisting of a casing, shaft, impeller and in some cases an inducer.

The largest amount of work is done by the impeller, the fluid flows from the suction nozzle through the impeller passages where energy is transferred to accelerate it in a circumferential direction and to increase the static pressure level. The next section will introduce the one dimensional flow theory with which the basic work transfer of the impeller is best described 2.2.1. The preceding sections will address limits of the one dimensional flow theory by presenting the slip factor and introducing incidence angle.

2.2.1. Work transfer in impellers

A one-dimensional flow theory (streamline theory) is often used to describe the basic principles of how pumps achieve a specific pumping task. These fundamental investigations are a major part of the design process for radial turbopumps.

The work transfer in impellers leads to an increasing static pressure as well as kinetic energy [21]. The flow can be described in a stationary frame of reference and a rotating frame of reference [8]. The two frames

are linked with the rotational speed of the machine $\vec{u}$ according to figure 2.2. The velocity in relative frame of reference is noted as $\vec{w}$ and in the stationary frame as $\vec{c}$ and the following equation exists.

$$\vec{c} = \vec{w} + \vec{u} \tag{2.1}$$

Applying a momentum balance on a control volume around the impeller considering the streamline theory on averaged velocity profiles provides "Euler's turbine equation" [21].

$$M_{th} = \rho Q_{La}(u_{2m}c_{2u} - u_{1m}c_{2u}) \tag{2.2}$$

The theoretical specific work can be determined using the velocity components presented in figure 2.2 and the blade angles. The power consumed theoretically by the blades $P_{th} = M_{th}\omega$ is divided by mass flow rate.

$$Y_{th} = u_{2m}c_{2u} - u_{1m}c_{2u} \tag{2.3}$$

Losses are not taken into account which allows the definition of the hydraulic efficiency which divides the useful energy in the discharge nozzle Y by the theoretical energy Y_{th}.

$$Y = \frac{p_{tot,2} - p_{tot,1}}{\rho} \qquad \eta_{th} = \frac{Y}{Y_{th}} \tag{2.4}$$

The useful energy Y represents the transfered energy per unit mass, for a second efficiency definition the useful power P is divided by the shaft power P_{shaft} in case the shaft power is known from numerical or experimental data.

$$\eta = \frac{P}{P_{shaft}} = \frac{\dot{m}Y}{P_{shaft}} \tag{2.5}$$

A common value to describe the performance of pumps is the head H $[m]$ which gives measure to the increase in total pressure of the fluid. The head can be calculated by dividing the specific work with the gravitational constant g according to equation 2.6

$$H = \frac{p_{tot,2} - p_{tot,1}}{\rho g} \tag{2.6}$$

Another way to present the theoretical head in radial turbomachinery allows a more detailed analysis on the effects of the individual velocity components on the generated pressure and useful work.

$$H_{th} = \frac{u_2^2 - u_1^2}{2g} - \frac{w_1^2 - w_2^2}{2g} + \frac{c_2^2 - c_1^2}{2g} \tag{2.7}$$

The head component $\frac{u_2^2-u_1^2}{2g}$ leads to a change in pressure due to centrifugal forces and a change in rotational speed in radial direction, it is not affected by blade angles and depends on inlet and outlet diameter. Another component represents the change in static pressure in the passages due to deceleration of the fluid in the relative frame of reference $\frac{w_1^2-w_2^2}{2g}$. The addition of these two components corresponds to the theoretical increase of static pressure if there were no losses. The last term $\frac{c_2^2-c_1^2}{2g}$ corresponds to the increase in kinetic energy due to acceleration of the flow in stationary frame of reference.

Brennen (1994) [8] gives simple trends in radial turbopumps that allow scaling predictions of the characteristics described above based on rotational speed and geometry with d_2 as the impeller outlet diameter.

$$\dot{m} \propto \rho\omega d_2^3 \tag{2.8}$$

$$H \propto \omega^2 d_2^2 \tag{2.9}$$

$$M \propto \rho\omega^2 d_2^5 \tag{2.10}$$

$$P \propto \rho\omega^3 d_2^5 \tag{2.11}$$

2.2.2. Reduction of "Euler work"

The specific work calculated with Euler's turbine equation increases with an infinite number of blades, however increasing the number of blades leads to increased friction losses in the radial machine. With a finite number of blades the flow in relative frame of reference is not completely aligned with the blade exiting the impeller passage. Secondary flow effects in the passage can increase the effect leading to a difference of theoretical work to real work transferred in the impeller, a factor can be implemented that takes this effect into account μ, a common factor to describe the so called slip effect is the slip factor σ.

$$\mu = \frac{c_{u2}u_2 - c_{u1}u_1}{c_{u2,\infty}u_2 - c_{u1}u_1} \qquad \sigma = 1 - \frac{\Delta c_{u2}}{u_2} \tag{2.12}$$

The velocity difference in the denominator describes the difference of the circumferential velocity component at the impeller exit.

2.2.3. Incidence

When calculating the theoretical work with Euler's turbine equation from the blade angles the assumption is perfectly aligned flow in the passage. As described, that can never be the case in reality, the flow angle at the exit deviates from the blade angles, furthermore the angle of the approach flow can deviate from the blade angle at the passage inlet. The difference of the angle of the velocity in relative frame of reference β_1 and the blade angle β_{1B} in relative frame of reference is called the incidence angle i_1. Along with the definition in "Centrifugal Pumps" the incidence is defined positive when the stagnation point is located on the pressure surface. Figure 2.3 shows the angle definitions used by Gülich and used in this report accordingly with a positive incidence angle.

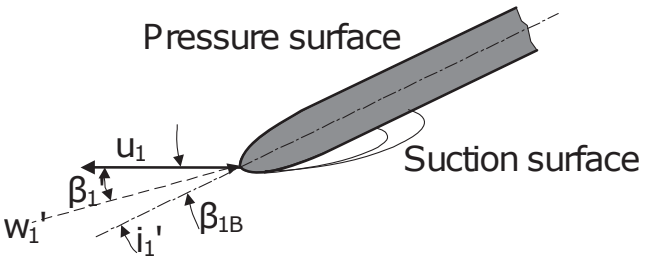

Figure 2.3: Incidence definition at impeller leading edge [21]

2.3. Introduction to pump characteristics

When the mass flow rate changes, the flow conditions vary inside the impeller and performance changes. This leads to a different behavior of the pump in off-design working conditions. The behavior is best described by the characteristic curve of pumps.

There are several different flow mechanisms that impact the work transfer in radial impellers. The following section addresses the flow around the blades as well three dimensional effects that impart efficiency and performance. The characteristics of the flow in the impeller are of three dimensional and viscous nature. A turbulent flow field develops that features friction losses. The adverse pressure gradient causes a retarding effect on the boundary layer flow which can lead to flow separation. The flow separation can lead to a reduction of pressure increase in the passage. A common way to locate separation for example is to investigate the static pressure distribution along the blades. When fluid flows around the blades a pressure difference develops from one side to the other. Due to the pressure difference the two sides of the blades are called pressure -and suction side. The distribution of static pressure over the blade is called blade loading, mostly a pressure coefficient c_p is presented. The loading is directly linked to the work transfer of the blades as well as the non-uniformities in the flow that increase with loading.

$$c_p = \frac{(p - p_{approach})}{0.5\rho w^2_{approach}} \tag{2.13}$$

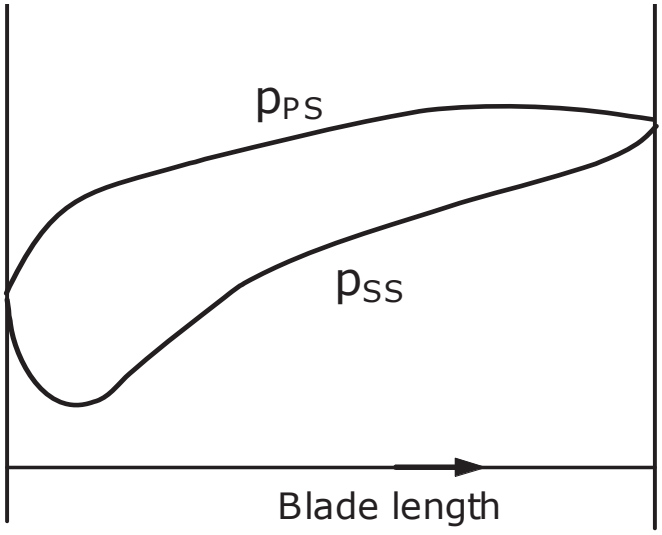

Figure 2.4: Typical pressure distribution around impeller blades [21]

A typical blade loading profile is shown in figure 2.4. On both the suction side SS and the pressure side PS the pressure rises due to centrifugal forces, however the pressure on the pressure side should be higher, if the pressure on the suction side exceeds the pressure on the other side the loaded blade drives the shaft, thereby acting like a turbine.

As described above the centrifugal forces increase the static pressure. To get a better understanding of the pressure distribution due to the retarding of the velocity in relative frame of reference thus the effect of the blade profile the reduced pressure can give better information [9].

$$p_{reduced} = p - 0.5\rho\omega^2 r^2 \tag{2.14}$$

To assess the behavior of pumps thoroughly the performance at different flow rates needs to be considered. The addressed parameters like head, power and efficiency change with varying flow rates. The characteristic curve usually presents dimensionless numbers to allow for a more general comparison and assessment of the behavior. The flow coefficient represents the flow rate through a turbo machine stage, it is calculated with the meridional velocity and the rotational speed, for radial turbomachines the rotational speed varies from inlet to outlet, in this project the flow coefficient ϕ generally refers to the definition with the outlet rotational speed u_2.

$$\phi_2 = \frac{c_{m2}}{u_2} \qquad\qquad \phi_1 = \frac{c_{m1}}{u_1} \tag{2.15}$$

The head coefficient Ψ represents the specific work in a dimensionless form. The common definition is:

$$\Psi = \frac{2Hg}{u_2^2} \tag{2.16}$$

A theoretical characteristic curve of pumps that is defined by the trigonometrical relations which originate from the velocities and blade angles presented in figure 2.2 and can be calculated as follows[8].

$$\Psi_{th} = 1 + \phi_2 \left(\tan\beta_2 - \frac{u_1\phi_1}{u_2\phi_2} \cot\alpha_1 \right) \tag{2.17}$$

Considering constant flow angle α_1 and constant flow angle at the exit in a relative frame of reference β_2 and constant ratios of meridional velocity c_{m1} and c_{m2} for small changes in flow rate the expression simplifies to a linear dependency of the work transferred to the flow rate [6]. However a real characteristic curve features different aspects.

As discussed above, the number of blades is finite which leads to a reduction of the Euler work due to slip at the exit of the impeller. Further loss mechanisms lead to a deviation of the pump characteristic curve from the theoretical one. A more detailed analysis of the different loss mechanisms follows in chapter 2. Figure

2.5 presents the theoretical head coefficient Ψ_{th} over the flow coefficient and three different hydraulic loss mechanisms in the impeller that determine the shape of the real characteristic curve.

- Reduction due to slip: The head coefficient Ψ correlates to the specific work which is reduced due to the occurrence of slip and the reduction can be calculated with 2.18 where N is the number of blades and β_2 the angle at the exit of the impeller in relative frame of reference. The equation indicates an independence of the flow coefficient and a decrease in losses with growing number of blades.

$$\Delta\Psi_\sigma = \frac{-2\pi\cos\beta_2}{N} \tag{2.18}$$

- Losses due to Incidence $\Delta\Psi_{Inc}$ occur due to change in approach flow at the entry of the impeller. A changing flow angle changes the velocity profile over the blade. The flow can for example face strong curvature on one side of the blade due to a change in stagnation region. Super-velocities occur which are followed by a strong adverse pressure gradient leading to boundary layer separation and separated flow, the separation region changes the effective passage and blade geometry that the flow aligns to. The losses due to incidence should be minimal at design point and increase towards off-design load points due to a changing angle of the approach flow.

- Skin friction $\Delta\Psi_{friction}$: Friction losses behave proportionally to the flow velocity in relative frame of reference which scales with the flow coefficient. The geometry and Reynolds number as well as surface properties play a role.

In literature the behavior is differentiated between a stable and an instable curve. A stable behavior is characterized by a decreasing head coefficient with an increase in flow coefficient so that $\frac{\delta\Psi}{\delta\phi} < 0$.

The figure 2.5 shows, that the pump characteristics are directly connected to the amount of hydraulic losses in the pump and already gives hints at how hydraulic losses are quantified. Further details on losses follows in chapter 2.4.

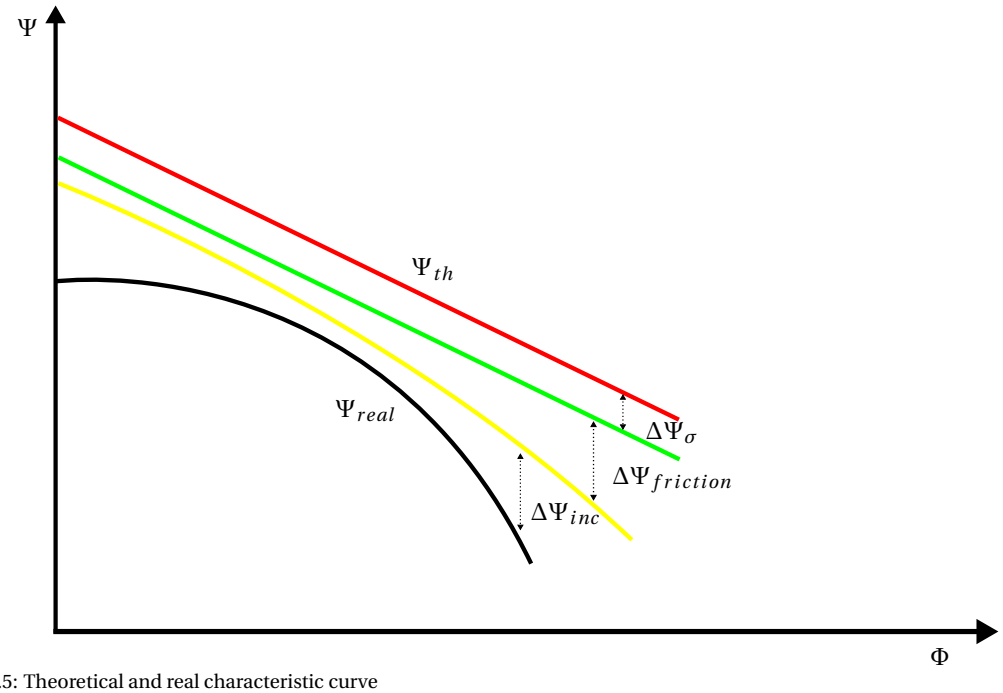

Figure 2.5: Theoretical and real characteristic curve

Rossby number

The pump characteristics are determined by three-dimensional flow effects that impact the velocity distribution in the impeller passage and the collector and the related hydraulic losses. These secondary flows are induced when forces act on the fluid perpendicular to the main flow direction [21]. The generation of the

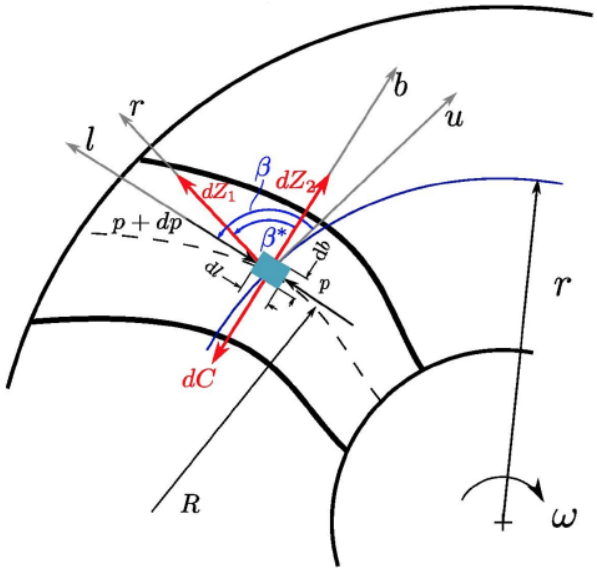

Figure 2.6: Forces acting on a fluid element in an impeller passage[6]

forces can be differentiated into three components on a body in the rotating frame of reference. The centrifugal acceleration due to rotation $b_z = \omega^2 r$, the Coriolis acceleration $b_c = 2\omega w$, and the centrifugal acceleration due to streamline curvature $b_z = w^2/R_{sl}$ (R_{sl} is the radius of the streamline curvature investigated) [21] and presented in figure 2.6. When shear stresses at walls and between streamlines are neglected the equilibrium of forces leads to the following equation presented by Gülich (p.191):

$$\frac{1}{\rho}\frac{\delta p}{\delta n} = 2\omega w + r\omega^2 \frac{\delta r}{\delta n} - \frac{w^2}{R_{sl}} \tag{2.19}$$

The centrifugal forces increase with growing circumferential speeds and with increasing radius of the streamline curvature R_{sl}. The Coriolis force is the inertial force due to movement in the relative frame of reference, so if the relative velocity of a fluid element is low the Coriolis force acting on the element is also low [6]. The figure 2.6 shows an example of the force acting on a fluid element where dZ_1 is the centrifugal force due to streamline curvature and dZ_2 the centrifugal force due to the rotation and dC the Coriolis force. The flow direction is marked with l and the direction perpendicular to the main flow direction with b in figure 2.6.

Gülich points out that the equilibrium of the body forces 2.19 determines the partload characteristic behavior since it is not sensitive to the Reynolds number and the accelerations in the equation are independent of the Reynolds number. The resulting pressure gradients lead to secondary flows and can be determined by the corresponding accelerations presented in equation equation 2.19. The "Rossby number" describes the ratio of the accelerations and determines the direction of the flow deflection.

$$Ro = \frac{b_z}{b_c} \tag{2.20}$$

Furthermore Gülich defines three different Rossby numbers to describe secondary flow patterns between the blades, in axial direction and in curved meridional sections. The different effects are superimposed to describe the secondary flow field that typically forms in radial impellers.

2.4. Losses and loss accounting in turbopumps

Losses in turbopumps have multiple origins. It is useful to differentiate between effects to clarify the key sources of losses for the individual pump. In the diagram in figure 2.7 the different loss mechanisms are presented in a power balance, on the left side the shaft power P is reduced by lost power due to hydraulic losses P_{vh}, lost power due leakage P_L and lost power due to disk friction P_{RR}. P_{Rec} considers the amount of lost power due to recirculation, P_{s3} considers leakage losses through interstage seals for multistage pumps and P_{er} similar to disk friction considers the amount of lost power due to axial thrust balance devises such as balance pistons or disks [21]. P_m considers the mechanical losses which are external to the pump and

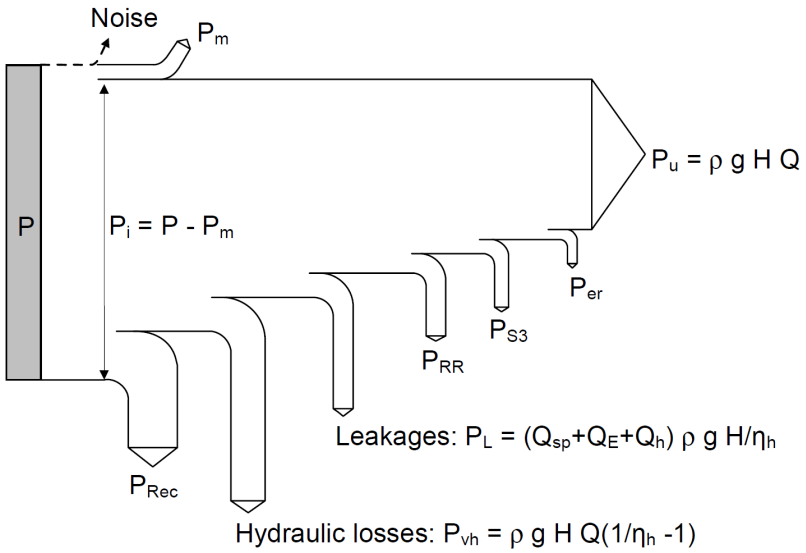

Figure 2.7: Loss mechanisms in power diagram [21]

not considered in the course of the project. The losses due to leakage and disk friction are summarized as secondary losses and dealt with in the next chapter 3.

This chapter deals with the different loss mechanisms in turbopumps focusing on effects that cause hydraulic losses (mechanical losses are not taken into account here). Losses reduce the useful energy delivered by the pump and lower its efficiency. The amounts of losses in the individual components of a pump add up to the useful head to equal the theoretical head calculated with the Euler equation. Gülich presents the losses of the inducer Z_I, the impeller Z_{LA} and the volute Z_{vol} according to equation 2.21.

$$H = H_{th} - Z_I - Z_{LA} - Z_{vol} \tag{2.21}$$

As shown in figure 2.5 hydraulic losses have several causes, briefly introduced in chapter 2.3. As Denton [19] points out, the historical dissection of losses into "profile loss", "endwall loss" and "leakage loss" is still commonly used but the effects are rarely independent. "Profile loss" is usually connected to the friction losses around the blades and the losses that occur after the trailing edge mostly based on a two dimensional flow analysis similar to the losses presented in 2.5. "Endwall losses" sometimes also referred "secondary losses" (not in this report) refer to losses caused by secondary flow phenomena in the passages. These are strongly coupled to the profile losses.

However generally the hydraulic loss effects can be reduced to two mechanisms which form the basis of any loss consideration. Losses are caused by friction and vortex dissipation caused by flow non-uniformities.

2.4.1. Friction losses

The theoretical work by Euler 2.3 applied on blade angles introduced above assumes an infinite number of blades. As mentioned already, increasing the number of blades too much leads to large friction losses. Friction due to viscous effects needs to be regarded when assessing losses in turbomachinery. When boundary layers form on the surfaces losses due to viscous shear stresses are generated. The growth of the boundary layer over the blades and the wakes that are formed downstream are subject to complex phenomena. The entropy generation can be considered when assessing the losses in boundary layers. The entropy generated is linked to the shear stresses in the boundary layer. The generated entropy solves with the integral below:

$$T\dot{S}_{irrev} = \int_0^{w_E} \tau_{xy} dw_x \tag{2.22}$$

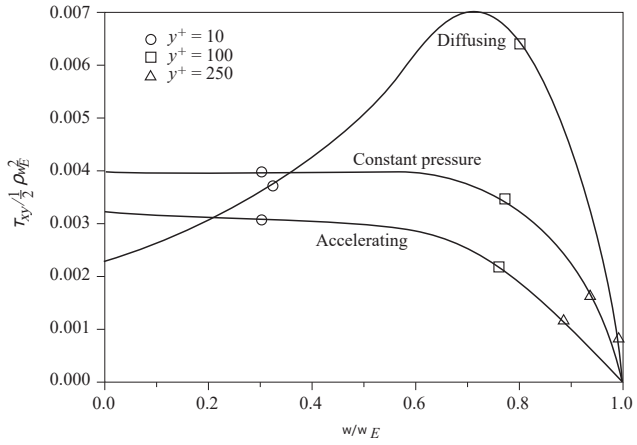

Figure 2.8: Shear stresses over velocity distribution in boundary layers [19] [9]

Figure 2.8 shows the development of shear stresses over velocity in three boundary layers which are subject to different pressure gradients. When looking at the integral area of shear over velocity it becomes obvious that losses are highest in boundary layers in adverse pressure gradients.

The mass-averaged total pressure loss can then be calculated as:

$$\overline{\Delta p_t}^M = \rho \frac{T\dot{S}_{total}}{\dot{m}} \tag{2.23}$$

The energy losses caused in boundary layers are created due to velocity gradients in the flow. Shear stresses can be expressed as a friction force per area between flow and and wall elements.The force due to shear stresses τ becomes:

$$dF_\tau = \tau_0 dA \tag{2.24}$$

The power which is dissipated due to shear stresses is then:

$$P_d = w_E F_\tau \tag{2.25}$$

Dissipated power and pressure loss is connected by $P_d = \Delta p_v \dot{m}$ [21]. The friction coefficient decreases with Reynolds number so for high Reynolds number flow viscous losses make up for a smaller portion of the overall losses. Viscous losses occur on additional surfaces in the passages. The viscous layers on the hub and on the shroud which increase complex and three-dimensional flows leading to additional losses [8], previously referred to as endwall losses. The skin friction losses on the rotating walls in the impeller sidewall gaps are called disk friction losses. These need to be added to the power balance and will be addressed in further detail in section 3.3.2.

2.4.2. Losses due to flow non-uniformities

The losses due to mixing of non-uniformities form the main source of energy losses in pumps according to Gülich. Especially in curved channels, pipes, impellers and diffusers the flow field becomes non-uniform which creates losses by turbulent dissipation through exchange of momentum [21]. These losses are sometimes referred to as mixing losses. This term includes mixing of a non-uniform velocity profile but also losses due to mixing of two physically separate flows with different properties. There are several causes of flow non-uniformities which are indicated by Gülich [21] (p.107) of which some are presented in more detail in this chapter:

- The work transfer of the blades creates a non-uniform velocity profile which increases with blade loading.

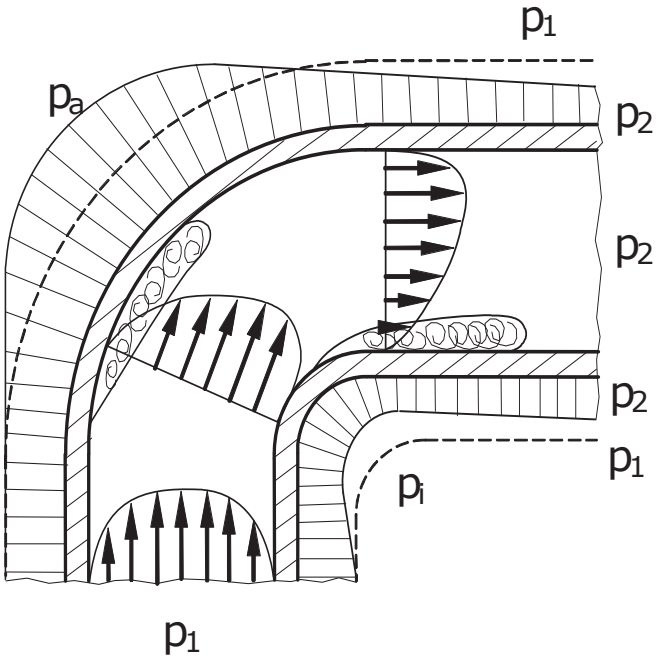

Figure 2.9: Pressure and velocity distribution in a curved channel [21]

- Local zones of low momentum flow or even separation on the blades causes non-uniformities.
- Curvature of the meridional section creates non-uniformities.
- Secondary flows generated by streamline curvature and the Coriolis force.
- **Injection of leakage flow through seals to the main passage:** This effect gives significance to the analysis of the impeller hydraulic losses in the course of this project because it represents a gap in knowledge in literature of how large the effect is and how the impact on the pump characteristics develops.
- Wake flow.

A cause of a non-uniform flow field in radial turbopumps is the curvature of the passage. In curved channels pressure increases from inner to outer radius [21]. Flow velocities are lower at the outer radius. Therefore the fluid on outer streamlines is more likely to separate due to the positive pressure gradient and low kinetic energy. Behind the curved part of the passage flow on the outer streamline accelerates and at the inner radius decelerates, which can lead to separation after the curved part on the inner streamline. Based on this basic principle some flow aspects in impeller passages can be explained.

Flow separation is one major aspect that leads to highly non-uniform flow fields in pumps. To gain better understanding of the cause of flow separation in passages the consideration of boundary layer flow is crucial. Boundary layer flow is governed by viscous effects. Due to friction, kinetic energy is converted into heat and flow is slower than the surrounding flow. Boundary layers are endangered to separate wherever a positive pressure gradient is present respectively where flow velocity is retarded. Avoiding large positive pressure gradients due to strong surface curvature or rapid deceleration is therefore recommendable. Flow separation is common in centrifugal pumps and occurs mostly on the suction surface near the leading edge. A wake is produced over the suction surface mostly ranging to the discharge of the impeller on all the blades. The flow exiting the impeller features mostly two regions one low velocity zone next to the suction surface and a zone with increased velocity next to the pressure surface. The velocity profile is commonly described with the "Jet-Wake-Model". The figure 2.10 shows a typical outlet velocity profile at the outlet of the impeller. Further downstream the velocities will have a uniform profile, during the process in between, entropy is generated and losses are created.

As Brennen states [8]:"*Relatively high rates of shearing occur in wakes, at the edges of separated regions, in vortices, and in leakage jets*", which makes the investigation of mixing losses very relevant for the project

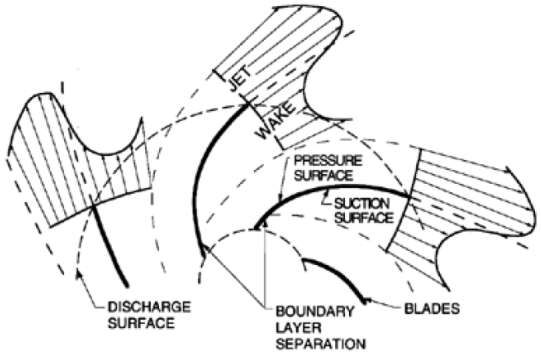

Figure 2.10: Typical impeller outlet velocity profile according to the "Jet-Wake-Model" [8]

and application. Mixing losses occur also when leakage flow is injected into the main flow. How losses due to mixing can be determined is presented in the following chapter on the example of a non-uniform impeller outflow.

2.4.3. Accounting for losses of the impeller

As seen above, the non-uniformities exiting the impeller inhibit mixing losses. These have to be accounted to the impeller and not to the downstream component. The correct determination of the hydraulic losses in the impeller is essential for the project because here the effect of leakage injection needs to be analyzed. The hydraulic losses in the impeller passage are determined by subtracting the head coefficient due to increase in total pressure from the theoretical head coefficient Ψ_{th} from blade angles. The hydraulic loss coefficient in the impeller ζ_{La} is then defined as follows.

$$\Psi_{th} = 2\left(\frac{(uc_u)_2}{u_2^2} - \frac{(uc_u)_1}{u_2^2}\right) \qquad \Psi = \frac{2(\overline{p_{2,tot}} - \overline{p_{1,tot}})}{\rho u_2^2} \qquad \zeta_{La} = \Psi_{th} - \Psi \tag{2.26}$$

However the losses that occur due to downstream mixing need to be associated to the impeller, so the definition above is only meaningful when the velocity profile is nearly uniform. To account for the downstream mixing losses Gülich presents different approaches. The kinetic energy of a non-uniform flow can be higher than the energy of a uniform flow at the same mass flow rate. According to Gülich observations show that the total pressure rise of impellers grows with increasing non-uniformities [21]. The method above therefore represents a lower limit of impeller losses. The analysis of a mixed out condition becomes useful. However analyzing losses in a mixed out condition over predicts the losses which makes this approach represent a maximum of the losses accounted to the impeller. The mixed out impeller losses can be calculated according to the equation below. The mixed-out averaging method is a common approach to account for losses that happen downstream of a component, it is further presented in the next section which deals with the different averaging methods used in literature 2.5.

$$\zeta = \Psi_{th} - \Psi_{static} - \left(\frac{\Psi th}{2} + \frac{d_{1m}^* c_{1u}}{u_2}\right)^2 - \Phi_2^2 + \left(\frac{\overline{c_1}}{u_2}\right)^2 \tag{2.27}$$

The average velocities are calculated from angular momentum and continuity equation, d_{1m}^* is the mean inlet diameter by the outlet diameter d_2.

$$\frac{C_{2u}}{u2} = 0.5\Psi_{th} + d_{1m}^* \frac{c_{1u}}{u_2} \tag{2.28}$$

The estimation that half of the excess kinetic energy is recovered is a plausible estimate [21]. The second approach is presented in the following section 2.5.

2.5. Averaging methods

As described in the previous section, non-uniform flow is common in centrifugal pumps. These flow non-uniformities will mix-out to become uniform during which process mixing losses occur. In order to account

for these losses from numerical simulation results or experiments one needs to address how to account for losses in non-uniform flow fields and how to find possible averages of properties that represent the losses and characteristics of the flow. As Pianko and Wazelt (1983) underline:*"No uniform flow exists which simultaneously matches all the significant stream fluxes, aerothermodynamic and geometric parameters of a non-uniform flow"* [9]. The choice of the averaging procedure is therefore important in order to obtain meaningful results for different purposes. Literature introduces guidelines of when to apply which averaging method. The following section introduces to the three common averaging methods: Mass average, area average and mixed-out average.

2.5.1. Mass average

For extensive properties such as enthalpy and entropy the mass average is a commonly recommended method. On the example of enthalpy the mass average is found with:

$$\dot{m}\overline{H}^{M} = \int H d\dot{m} \tag{2.29}$$

For intensive properties such as pressure and temperature the averaging methods are discussed to a larger extend, the paper by Cumpsty and Horlock (2006) [23] concerns with the way pressure should be averaged. A common method however is the mass average on stagnation pressure.

$$\dot{m}\overline{p_{tot}}^{M} = \int p_{tot} d\dot{m} \tag{2.30}$$

2.5.2. Area average

The area average is the appropriate averaging method to average static pressure [23]. The derivation follows from the force due to pressure acting on a surface area.

$$F = A\overline{p}^{A} = \int p dA \tag{2.31}$$

Applying the area averaged method to the stagnation pressure however cannot be associated to any conservation law which makes the use not reasonable for that property [9].

2.5.3. Mixed out average

An approach to averaging flow non-uniformities is to imagine that the flow undergoes a process downstream of the considered plane which leads to a uniform profile [23]. Assumptions need to be taken under which the process takes place. The common assumption which is the one also presented by Greitzer (2004) [9] is that the flow area remains constant downstream. The mixed out average total pressure is the pressure that would exist after complete mixing at constant area [9]. Furthermore wall friction is neglected in the imagined process of mixing. If the flow is uniform at the exit of a two dimensional channel with the width A where x indicates the direction of the main flow and y points in the direction perpendicular to the flow [9] and according to figure 2.11 the averaged velocity can be calculated with the integral:

$$\int_{\frac{-A}{2}}^{\frac{A}{2}} c_x dy = \overline{c} A \tag{2.32}$$

Gülich presents the mixed-out average with the area integral of the velocity over the average velocity which is determined from the continuity equation. This leads to a mixing loss coefficient ζ_{mix}:

$$\zeta_{mix} = \int \left(\frac{c}{Q/A} \right)^3 \frac{dA}{A} - c_p - 1 \tag{2.33}$$

The coefficient c_p in this case represents the pressure recovery coefficient which is defined as shown in equation 2.34 with $c_a v = Q/A$.

$$c_p = \frac{p_2 - p_1}{\rho/2 c_{av}^2} \tag{2.34}$$

Figure 2.11: Equalization of a non-uniform velocity profile [21]

The presented method can be applied to non-uniform velocity profiles and to two or more separate flows that mix with constant velocities by replacing the integrals with summations of the investigated flows.

Applied to the impeller outlet flow the hydraulic losses of the impeller can then be determined with equation 2.35

$$\zeta_{La} = \Psi_{th} - \Psi_{La} + \zeta_{mix} \tag{2.35}$$

2.6. Conclusions for research question

The previous section addresses the main sources of losses in turbopumps, even though the project deals with the losses due to secondary flow paths an interaction exists due to the leakage injection to the main passage. Therefore the analysis of the hydraulic losses in the impeller is justified and important for the project. Losses investigated in the course of the project are the hydraulic losses and the secondary losses, hydraulic losses are determined with the difference between the theoretical head and the real head of the impeller or pump respectively when applying the correct averaging methods to the outflow velocity profile. The effects of leakage injection on the pump performance represent a large unknown in the field which will also be shown in the modeling section of this report 4.

Hydraulic loss calculations from numerical results are subjected to high uncertainties 10 % [21].

3

Losses Associated with Secondary Flow Paths

The losses in side cavities of shrouded radial impellers have been subject to research for a long time. The chapter addresses the different loss mechanisms that are associated with secondary flow. Furthermore the common methods of how to determine these losses are presented. It will be divided into sections that deal with the loss mechanisms individually and one introductory section to describe the flow in side cavities in general. As mentioned before the losses that are associated with secondary flow paths can be divided into secondary losses and hydraulic losses due to leakage injection to the main passage according to figure 3.1.

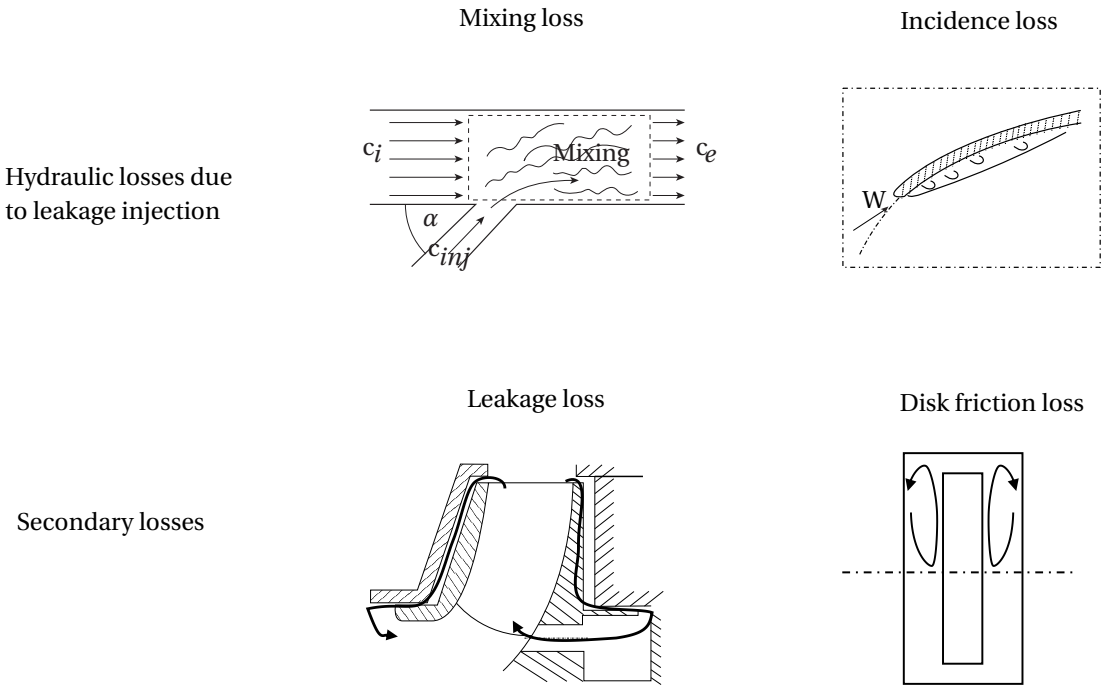

Figure 3.1: Losses associated with secondary flow paths

The injection of flow causes larger non-uniformities in the flow field which leads to mixing losses. When injecting leakage to the main passage upstream of the impeller blade the approaching flow angle can be changed which can lead to a change in hydraulic performance of the component due to incidence losses. Secondary losses mostly refer to leakage losses and disk friction, the term sometimes also includes mechanical losses which are not considered in this project [21]. Disk friction describes the power losses due to skin friction on the rotating walls in the cavities and leakage losses refer to the direct reduction of useful work by extracting pressurized fluid from the impeller outlet thereby reducing the useful effective mass flow at the

outlet of the pump.

3.1. Flow in side cavities of shrouded radial impellers

Flow inside the side cavities is subject to a number of different driving mechanisms that impact the behavior and the specific characteristics of it. The side cavity between the rotating hub and shroud of the impeller and its casing is filled with the pumped fluid. A pressure difference induces a resulting flow from the high pressure outlet back to the inlet of the impeller, which makes the implementation of a seal in these side gaps crucial in order to reduce the amount of leakage flow and reduce the associated leakage losses. Without taking the leakage flow into account, the rotating shrouds already introduce a circulating flow in the cavities. Figure 3.2 shows a typical flow field in the side cavities on the low pressure side and on the high pressure side of a shrouded impeller. Due to the no-slip condition on both sides of one cavity, boundary layers form. The circumferential velocities are higher close to the rotating wall where centrifugal forces drive fluid radially outwards and as a result a radial inward flow close to the stationary walls. There are several different flow regimes possible in the side cavities. Depending on Reynolds number and gap width of the cavity the boundary layers on both sides can be merged or separate. In case of separate boundary layers a core flow is formed where radial velocities are nearly constant as shown in figure 3.2. Furthermore the boundary layers can be laminar or turbulent. In most of the relevant literature the condition of turbulent boundary layers and core flow is assumed [25]. According to Güllich [21] most of the pumping applications feature that condition and especially in turbopumps for rocket engines where very high rotational speeds are common [5]. Analytical loss models commonly feature the assumption of turbulent boundary layers and a core flow.

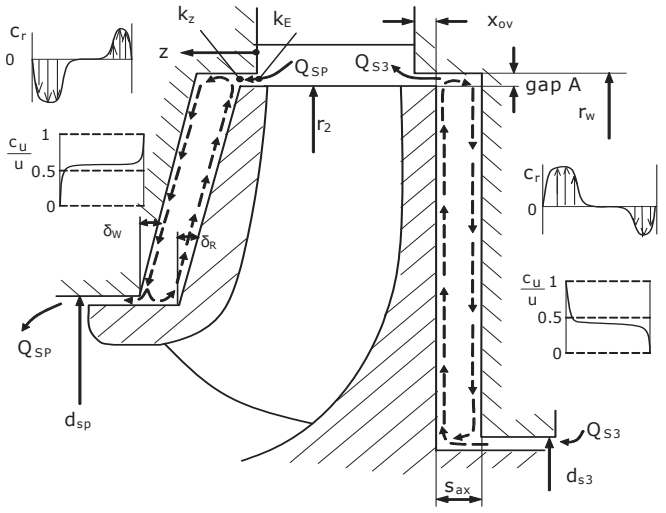

Figure 3.2: Typical flow field around shrouded impellers [21]

The seal leakage on the front shroud creates a net flow through the side cavity. This flow is directed inwards and carries momentum from the impeller exit. Figure 3.2 shows the velocity profile on the left side and the enhancing effect of the through flow on the rotation in the cavity. The high pressure side features different flow characteristics, the net flow is directed radially outwards and emerges from a seal. The example case shown in figure 3.2 features an interstage seal where seal leakage flows to the impeller outlet. If leakage is directed outwards the effect on the flow field is different, the flow is retarded due to the low momentum in the leakage which is mixed to the circulation in the cavity. The flow features in the side gaps depend on the gap geometry the pump layout and also the thrust balancing method applied in the side gaps. According to Gülich three cases can typically be found in turbopumps:

- **The pump features balance holes for thrust balancing, in this case leakage is flowing radially inwards and conditions are similar to the conditions in the front side gap.**
- Pumps that do not feature balance holes in the impeller hub a shaft seal prevents leakage, so the flow just describes a circulation
- In multistage-pumps an interstage seal leads to net flow directed radially outwards as described above.

In order to reduce the scope of the research suitable to a master project, only the first case will be investigated further. The choice is due to the fact that the application and example pumps are of type: single-stage with balance holes.

The flow field, the amount of leakage mass flow and the associated losses in the sidewall gaps depend on a number of parameters and characteristics of the overall pump.

1. The **circumferential velocity** that enters the side cavities and mixes to the circulating fluid in the cavities and impacts the circumferential velocity of the entire flow field. If high momentum flow enters the cavity it increases the rotational velocity and reduces velocity gradients and shear stresses on the rotating disks, furthermore the flow experiences a larger pressure drop due to higher rotation [15]. The entering fluid flow in the side cavities is largely coupled to the flow exiting the impeller. Depending on the outlet design more or less interaction can be expected. Especially when the sidewall gaps are wide open to the main flow like in pump designs with volutes and open side gaps large interaction between the components is likely. The interaction leads to many uncertainties when predicting losses and modeling thrust [21] making volute pumps interesting for further research. The effect of pre-rotation on the flow in the side cavities was investigated by Poncet, Chauve and Le Gal (2004) [25] experimentally showing that when high circumferential velocity flow enters the cavity, rotation is enhanced in the whole cavity and pressure drop increases.

2. Connected to the circumferential velocity impact described above, **recirculation** which usually occurs at the impeller outlet at partload slows down the fluid entering the side cavities and therefore changes the flow behavior.

3. The **roughness of rotating and casing wall** impacts the fluid rotation when different roughness on casing and rotating disk is chosen, the rotational velocity is increased if the roughness on the rotating wall is higher and the same effects as described above can be expected. However increasing roughness on the rotating disk increases shear stresses and torque on that surface hence higher disk friction losses.

4. The **width of the sidewall gap** s_{ax} impacts the flow especially when chosen small so that $s_{ax} < \delta$ (boundary layer thickness)[21]. In this case a linear velocity distribution can be expected. The impact of the axial clearance is minimal in turbulent flow [21], [25], which is the flow regime in the side cavities that is expected and modeled in the course of this thesis project.

5. The **leakage flow** changes the flow field in the side cavities as described above, rotation is added when leakage is directed inwards and $c_u / u_2 > 0.5$. Numerical and experimental results performed by Hu et. al [4] (2017) confirm the effect described by Gülich and Poncet. Increased inward through flow increases the pressure drop in the gap.

The analytical modeling of the flow in a common concept faced many challenges until today. The largest uncertainties are due to close interactions of disk friction, pre-rotation and roughness effects [21].

Further research was mostly done on rotating disks in cylindrical casings where disk friction factors as empirical correlation of Reynolds number and roughness were derived [20]. Following research on the matter lead to the understanding that the flow can be described by splitting it into three separate regions, two boundary layers and a core flow where the rotation factor is constant, the main research on that was done by Batchelor (1951) (Flow that behaves similarly is called Batchelor-type flow) . Le Gal and Chauve (2001) were able to confirm the investigations with their experimental data and found out that core flow develops if the gap width is larger than the boundary layer thicknesses. In the core flow, radial velocities are nearly zero and circumferential speeds are $k\omega r$ and close to the rotating walls velocities range from $k\omega r$ to ωr. Daily and Nece (1960) [17] investigated the effect of gap width on the flow. The effect of leakage on the velocity distribution and pressure losses was investigated in the following years. Daily, Ernst and Asbedian (1964) [18] determined that flow with weak through-flow shows a similar behavior as the one without through-flow but the main part of the net flow accelerates the layer which is directed radial inwards.

3.2. Hydraulic losses due to leakage injection

When the leakage flow is injected to the main flow, mixing losses occur, these have been mentioned in section 2.4. The injection causes non-uniformities in the flow which cause a reduction in total pressure during the

mixing process. Because a mixed-out and undisturbed condition is unlikely to occur in the passage downstream of the injection these losses need to be accounted for in a similar manner as the impeller downstream mixing losses 2.4.3. The mixed-out average gives an estimation of the mixed-out condition and the losses due mixing of leakage flow to the main flow can be quantified.

Apart from the losses due to viscous effects in a non-uniform flow field, the change of velocity profile due to injection of leakage flow can change the hydraulic pump performance and its stability. Injection mostly takes place in front of the impeller inlet at the shroud and at the entrance of the impeller blade passage at the hub. Changing the flow field at the outer and inner streamline changes the incidence of the approach flow. With regard to leakage injection Gülich states [21]:*"Impeller flow and Q-H-curve can react with great sensitivity to changes in the approach flow"*. This statement underlines the uncertainties in literature due to this effect since it is so dependent on the pump type and design.

Compared to the other loss mechanisms less literature can be found that investigate the effects of leakage injection on the pump performance. A recent study at the Technical University Munich has been performed to analyze the change of flow field with increasing leakage mass flow [26], the pump in that project showed changes in performance that could be explained mainly due to a higher mass flow rate the impeller. However as Gülich points out [21]: *"The effect of the leakage injection on the flow in the impeller can be important in particular cases (e.g. with respect to the Q-H-curve stability or cavitation). However it is difficult to predict in which cases this applies. The study of a specific case cannot be generalized"*. Referring to the following chapter, loss modeling 4, the literature review does not reveal existing analytical loss models of this effect. The change of hydraulic impeller performance due to leakage injection needs to be determined by comparing hydraulic losses determined from results with and without leakage injection. The method to correctly quantify hydraulic losses in the impeller has been presented in chapter 2.4.3.

3.3. Secondary losses

3.3.1. Leakage losses

Design aspects between rotating shrouded impellers and the non-rotating casing make the occurrence of leakage inevitable. In the investigated pump layout leakage flows from the impeller exit through side cavities and seals and is then re-injected to the main flow at the impeller inlet on the front side. On the back side the injection takes place through holes in the impeller hub. Leakage mass flow needs to be taken into account not only to correctly assess the efficiency but also during the design phase since the effective flow coefficient increases due to a higher mass flow rate in the impeller. The mechanical energy transfered by the impeller to the leakage flow is throttled and converted into heat in the seal [21], this leads to a direct reduction of the efficiency since the amount of lost work has to be compensated by the impeller whereas the effective mass flow remains constant. The amount of power needed to increase the pressure of the leakage flow again can be calculated by using the formula 3.1 below.

$$P_L = \rho g H_{th} Q_{sp} \tag{3.1}$$

In the formula above it becomes evident that the leakage mass flow determines the amount of power loss. The most common seals in turbopumps for rocket engines are floating ring seals and labyrinth seals [28]. Floating ring seals feature an annular gap whereas labyrinth seals present a more complex flow path. This project will focus on ring seals with annular gaps. In the slim channel ($s << r_{sp}$) flow is accelerated in axial direction due to a static pressure difference $p_{ax,sp}$ over the sealing path. The axial flow is again overlapped by a rotational flow around the rotating inner cylinder. Mass flow through the gap is directly related to the pressure difference across the seal according to equation 3.2.

$$\dot{m}_{sp} = \zeta A_{sp} \sqrt{\frac{2\Delta p}{\rho}} \tag{3.2}$$

3.3.2. Disk friction

The rotating walls of shrouded impellers generate drag losses due to shear stresses on the surfaces [20]. The fluid in the side gaps is set in motion by the rotating walls and centrifugal forces carry fluid close to the walls radially outwards. The pressure distribution is determined by that motion and thus axial thrust and disk friction as well as leakage losses influence one another. The shear stresses, resulting torque and resulting friction power can be calculated as follows. The friction coefficient depends on roughness of the surface and on Reynolds number.

$$\tau = \frac{1}{2}\rho c_f w^2 \tag{3.3}$$

$$dF = 2\pi\tau r dr \tag{3.4}$$

$$PRR = \frac{\pi}{5}\rho c_f \omega^3 r^2 \tag{3.5}$$

The disk friction can be determined from numerical results by directly integrating the torque M due to shear stresses on all the rotating walls in the side cavities.

$$P_{RR} = \omega \int dM \tag{3.6}$$

According to Poncet et. al. [25] and Gülich the amount of disk friction in the sidewall gap is largely dependent on the inlet swirl of the gap , the general trends are presented in his paper on disk friction on closed turbomachine impellers. If fluid with a high circumferential velocity enters the sidewall gaps and leakage is directed radially inwards the disk friction losses decrease due to growing fluid rotation. If the pump features large clearances the disk friction can drop to a fraction of the of the value without leakage through flow according to Gülich [20]. If the fluid enters with low speeds on the other hand the disk friction losses increase with growing leakage because the flow in the side cavity is slowed down. Radially outward leakage will increase disk friction irrespective of the preswirl. The impact of leakage flow on the disk friction decreases with increasing ratio of inner to outer radius.

3.4. Conclusions for research question

The section introduced the main flow mechanisms of secondary flow paths in shrouded impellers. The goal was to identify the loss mechanisms that are associated to secondary flow paths and explain their behavior. The losses can be differentiated between secondary losses which include leakage losses and disk friction losses and hydraulic losses due to the leakage injection (mixing and incidence loss). The secondary losses can be determined from numerical results by integrating shear stresses and determining the leakage mass flow. For the impact of leakage injection on the hydraulic performance the impeller losses need to be evaluated according to 2.4.3 and compared with and without leakage injection. The detrimental effects of the leakage injection on the hydraulic performance are quite unknown in literature. For the effect of leakage injection through balance holes for example, no previous research could be found.

4

Loss Modeling

In this chapter, loss models from literature are introduced that are commonly used to estimate the individual effects. The focus hereby lies on the modeling of the losses that are associated with secondary flow paths. Models for wake mixing and friction are only briefly introduced.

4.1. Mixing losses

Denton [19] presents an approach to assess mixing losses of wakes behind trailing edges. It is based on a control volume analysis at the passage exit and downstream. The trailing edge loss coefficient is computed according to the equation 4.1.

$$\zeta = -\frac{C_{pb}t}{w} + \frac{2\theta^*}{w} + \left(\frac{\delta^* + t}{w}\right)^2 \tag{4.1}$$

where t is the trailing edge thickness θ^* and δ^* boundary layer momentum thickness of the individual sides and w the throat width. C_{pb} represents the difference of base pressure upstream of the trailing edge compared to base pressure acting at the trailing edge.

$$C_{pb} = \frac{P_b - P_{ref}}{0.5\rho c_{ref}^2} \tag{4.2}$$

As mentioned earlier a second flow feature in radial turbopumps is prone to create mixing losses that needs to be mentioned here. Mixing losses occur where the leakage flow is injected into the main passage. The velocity profile downstream will be altered due to the flow injection.

Denton [19] presents a simplified version of the mixing process where one flow rate is small compared to the other one. This case can be applied to the leakage injection and the assessment of the mixing losses and is visualized in figure 4.1.

The simplified model was developed by Shapiro (1953) [2], it solely regards the entropy change of the main flow and disregards the entropy change of the injected flow. The angle and the difference in velocities are the

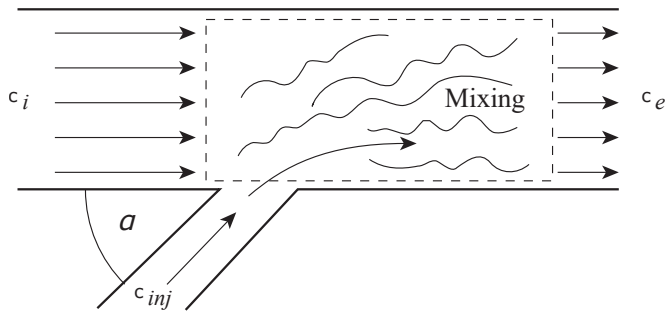

Figure 4.1: Mixing of injected flow with a mainstream flow (adapted from [9])

driving parameters that determine the losses of the leakage injection. The entropy generation can then be linked to the change of total pressure due to injection [19].

$$T\dot{S} = -(\dot{m}_i + \dot{m}_{inj})\frac{\Delta p_{tot}}{\rho} = \dot{m}_i(c_i^2 - c_{inj}\ c_e \cos\alpha) \tag{4.3}$$

In case of $c_i > c_{inj}$ and small injection angles the total pressure can rise in the main flow, yet losses occur. These can be evaluated by comparing the useful energy before and after the mixing process if known.

$$\dot{m}_i p_{tot,i} + \dot{m}_{inj} p_{tot,inj} = (\dot{m}_i + \dot{m}_{inj}) p_{tot,e} + \rho T\dot{S}_{overall} \tag{4.4}$$

4.2. Friction losses

As already mentioned in section 2.4.1 the losses due to viscous shear stresses in the fluid are subject to complex phenomena, yet some qualitative guidelines for the resulting viscous effects are presented by Brennen [8]. The boundary layer on the suction surface is likely to be thicker than on the pressure surface, furthermore the boundary layer grows fastest over the area where adverse pressure gradients occur. Most of the shear stresses and losses occur in boundary layers in adverse pressure gradients as presented by Denton (1993) [19].

Brennen [8] relates the pressure loss in boundary layers to the momentum thickness of the wake they form downstream of the blade θ^*. The total pressure loss is mostly determined by the suction surface where the highest adverse velocity gradients occur [8]. This connection was done by Lieblein (1965) who introduced a diffusion factor $\frac{w_{max}-w_2}{w_{max}}$ to show the deceleration from w_{max} to w_2 and showed that it is the primary factor that determines the wake thickness [8]. This approach allows estimations of the losses caused by viscous effects $\Delta p_{tot,L}$ where the loss coefficient f is defined as:

$$f = \frac{\Delta p_{tot,L}}{0.5\rho w_M^2} \tag{4.5}$$

And becomes:

$$f = \frac{s\sin(\beta_M)}{\sin^2(\beta_2)}\frac{\theta^*}{c} \tag{4.6}$$

Where s is the solidity c the chord length and β_M the mean angle of the flow in relative frame of reference and β_2 the flow direction at the exit of the blade.

The losses in the boundary layer can be assessed from the shear stresses and the velocity distribution as presented in chapter 2.4.1. However these properties are rarely a known quantity in design processes so Denton gives a useful estimation of the dissipation coefficient $C_d = \frac{T\dot{S}_irrev}{\rho w_e^3}$ for turbomachinery blading of $C_d = 0.002$ so that for flow through a two-dimensional passage the rate of boundary layer entropy generation over the surfaces becomes [9] (U is the reference velocity):

$$T\dot{S}_{total} = C_d \sum_{allsurfaces} \rho L U^3 \int_0^{x_{final}} \frac{w_E}{U}^3 d(\frac{x}{L}) \tag{4.7}$$

4.3. Leakage mass flow

In literature there are several approaches to determine the leakage flow rate through an annular gap. The approach presented in the Roloff/Matek [14] can be seen below. The gap width s is the most influencing parameter and enters the equation to the power of three.

$$Q_{sp} = \frac{\Delta p_{stat} s^3 \pi d}{12\mu\rho l} \tag{4.8}$$

Gülich [21] presents a different approach which is similar to the research of Schneckenberg [10] which can be seen in 4.9.

$$c_{gap} = \sqrt{\frac{2\Delta p_{stat}}{\lambda\frac{l}{2s} + \zeta}} \tag{4.9}$$

The loss coefficient ζ combines different effects that occur in the seal gap.

- The immediate decrease in cross sectional area creates losses at the inlet of the gap. $\Delta p_i = \frac{\rho}{2}\zeta_i \overline{c}_{ax}^2$.
- Losses occurring downstream of the gap inlet until the flow field develops $\Delta p_d = \frac{\rho}{2}\zeta_d \overline{c}_{ax}^2$.
- At the exit of the gap the cross sectional area increases instantly which leads to deceleration, separation and recirculation creating further losses $\Delta p_o = \frac{\rho}{2}\zeta_o \overline{c}_{ax}^2$
- Viscous losses due to friction on the walls $\Delta p_\lambda = \lambda_{axsp} \frac{\rho}{2} \frac{l}{2 s_{ax} \overline{c}_{ax}^2}$, λ depends on whether the flow in the gap is laminar or turbulent.

The friction coefficient λ is dependent on Reynolds number and needs to be determined iteratively since the Reynolds number defined for the seal gaps ($Re = \frac{2 s c_{ax}}{\nu}$) depends on the axial velocity .

For both methods the pressure difference over the seal needs to be known. In the side cavity upstream of the seal the pressure reduces an unknown amount. Knowledge of pressure distribution in the side cavities is important to estimate not only the leakage losses but also the axial thrust as well as disk friction losses. The analytical approach to the flow in side cavities has been built up over many years of research. The main changes and different models are part of the next section.

The leakage mass flow prediction capability is strongly coupled to the accuracy on the rotation factor modeling. Furthermore the loss coefficient in the sealing gap needs to be assumed which can lead to further errors. The clearance of the seal gap width can vary from the design value due to manufacturing tolerances. These factors lead to uncertainties of 30 % for leakage mass flow predictions as pointed out by Gülich [21].

4.4. Rotation factor

Rotation factor without through-flow

Disk friction, leakage mass flow and axial thrust depend on the flow behavior in the side cavities which are complex and three dimensional as described in chapter 3. Finding a representative coefficient or factor to describe the flow in the side gaps so that losses and thrust can be estimated has been subject to a lot of research [25], [4], [29], [15].

Most of the projects consider the so called rotation factor k to describe the flow effectively. It was first established by Stépanoff (1932) [3] who set the typical value of the rotation factor to be $k = 0.5$ independent of the radius. It describes the ratio of fluid velocity to impeller circumferential velocity with β the fluid rotational speed.

$$k = \frac{c_u}{u} \tag{4.10}$$

Zilling [15] derives the model for the rotation factor of a sidewall gap without through-flow from the balance of moments equation for the medium in the sidewall gap on a fluid element. The fluid in the side wall is treated as a solid body, which rotates with the angular speed β_0. The body is in equilibrium when the summation of the different torque components that act on the fluid equals zero. The equation contains the torque on the rotor wall M_R, shaft M_S, casing wall M_W and the outer cylindrical face of the casing M_F. The labels used in this approach are presented in figure 4.2.

$$dM_R + dM_S - dM_W - dM_F = 0 \tag{4.11}$$

On a fluid element the moments on the casing and rotor wall perpendicular to the rotational axis are:

$$dM_R = 2\pi r^2 \tau_R dr \qquad dM_W = -2\pi r^2 \tau_W dr \tag{4.12}$$

The shear stresses are taken from the equation of turbulent flow in pipes ($\overline{w}$ the average velocity in relative frame of reference).

$$\tau = \frac{\rho}{8} \lambda \overline{w^2} \tag{4.13}$$

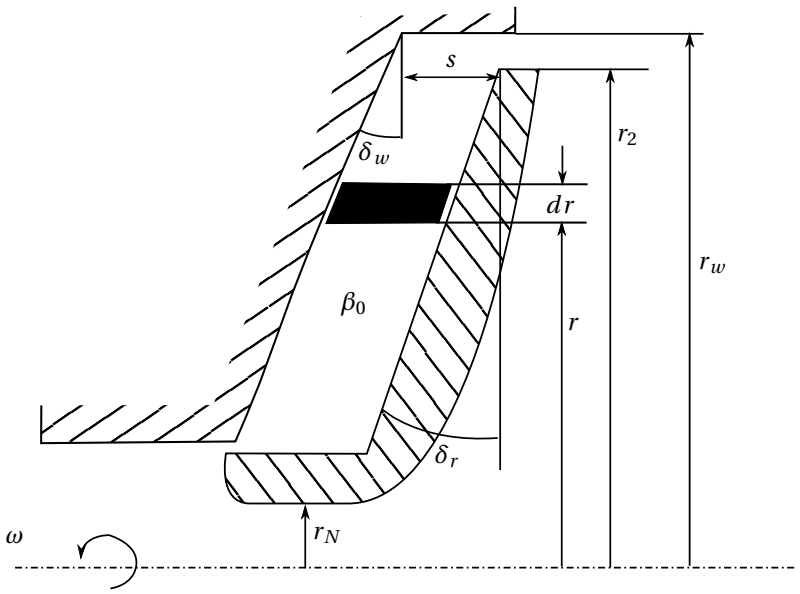

Figure 4.2: Side cavity labels for model without through-flow (adapted from [15])

Neglecting the dependency of λ on the radius and integrating the equations in 4.12 from inner to outer radius with the velocity in relative frame of reference as $\overline{w_R} = \omega - \beta_0$ and $\overline{w_W} = \beta_0$ the torque becomes:

$$M_R = \frac{\pi\rho\lambda_R}{20cos\delta_R}(r_2^5 - r1^5)(\omega-\beta_0)^2 \qquad M_W = \frac{\pi\rho\lambda_W}{20cos\delta_W}(r_2^5 - r1^5)\beta_0^2 \tag{4.14}$$

The torque on the cylindrical faces (shaft and casing) is calculated by:

$$M = 2\pi t_{ax}\tau r^2 \tag{4.15}$$

So for the individual faces the equations are:

$$M_F = \frac{\pi\rho\lambda_W}{4} r_W^4 \beta_0^2 \qquad M_S = \frac{\pi\rho\lambda_R}{4} r_1^4 [t_{ax} + (r_W - r_1)\tan\delta_W - (r_2 - r_W)\tan\delta_R](\omega-\beta_0)^2 \tag{4.16}$$

Applying these to the momentum equation in 4.12 leads to the rotation factor without through-flow.

$$k_0 = \frac{1}{1 + \sqrt{\frac{\frac{1}{\cos\delta_W}\left\{\left(\frac{r_W}{r_2}\right)^5 - \left(\frac{r_i}{r_2}\right)^5\right\} + 5\frac{t_{ax}}{r_2}\left(\frac{r_w}{r_2}\right)^4}{\frac{1}{\cos\delta_R}\left\{1 - \left(\frac{r_i}{r_2}\right)^5\right\} + 5\frac{t_{ax}}{r_2}\left(\frac{r_i}{r_2}\right)^4\left\{1 + \frac{r_w - r_i}{t_{ax}\tan\delta_W - \frac{r_2 - r_i}{t_{ax}}\tan\delta_R}\right\}}\left(\frac{c_{f,W}}{c_{f,R}}\right)}} \tag{4.17}$$

When assuming the ratio of the radii small $r_1/r_2 = 0$ and $r_W/r/2 = 1$ and the ratio of the friction coefficients $C_{f,W/R} = \frac{c_{f,W}}{c_{f,R}}$, the equation above 4.17 simplifies to:

$$k_0 = \frac{\beta_0}{\omega} = 1 + \left(\frac{r_w}{r_2}\right)^2 \sqrt{\left(\frac{r_w}{r_2} + 5\frac{t_a x}{r_2}\right) C_{f,W/R}} \tag{4.18}$$

Rotation factor with radial through flow

The most prominent approach to determine the behavior of the rotation factor with superimposed through-flow was developed in 1976 by Möhring [29]. Based on Zilling's investigations he developed a differential equation that allows a stepwise calculation of the local rotation factor in side cavities with leakage flow. The

approach is based on the balance of moments similar to the derivation of the fluid rotation without through-flow which is presented above. However there are more terms entering the balance of moments equation. Moments due to friction on the rotating and stationary wall dM_R and dM_W and the moment due to flow entering the fluid element dM_{Imp} and the moment due to secondary flows exiting and entering the fluid element close to the walls due the developed secondary flows radially inwards and outwards $dM_{Imp,R}$ and $dM_{Imp,W}$.

$$dM_R + dM_W + dM_{Imp} + dM_{Imp,R} + dM_{Imp,W} = 0 \tag{4.19}$$

The moment due to mass flow entering the fluid element is calculated as follows with $x = r/r2$ the ratio of radius to inlet radius:

$$dM_{Imp} = \rho Q_{sp} \omega r_2^2 x(2kdx + xdx) \tag{4.20}$$

For the frictional torque assumptions for the friction coefficients λ_R and λ_W have to be taken. Möhring uses the proportionality for the boundary layer thickness to radius and rotational speed established by Schlichting [13] $\delta \sim r^{0.6}((\frac{\nu}{\omega})^{0.2}$ so that the boundary layer thickness becomes:

$$\delta_R = \gamma_R r^{0.6} \left(\frac{\nu}{\omega}\right)^{0.2} \qquad \delta_W = \gamma_W r^{0.6} \left(\frac{\nu}{\omega}\right)^{0.2} \tag{4.21}$$

And Zilling [15] establishes the formula for the friction coefficients.

$$\lambda_R = 0.18 \left(\frac{\nu}{\delta_R r(\omega - \beta)}\right)^{0.25} \qquad \lambda_W = 0.18 \left(\frac{\nu}{\delta_W r \beta}\right)^{0.25} \tag{4.22}$$

The frictional torque can then be written as:

$$dM_R = \frac{\pi}{4} \lambda_R \rho r_2^5 \omega^2 (1-k)^2 x^4 dx \qquad dM_W = -\frac{\pi}{4} \lambda_W \rho r_2^5 \omega^2 (k)^2 x^4 dx \tag{4.23}$$

Inserting the terms for the individual moments to equation 4.19 while neglecting the moments due to secondary flow the differential equation for the rotation factor over the dimensionless radius becomes:

$$\frac{dk}{dx} = \frac{\pi}{4} \frac{x^2}{\frac{Q_{sp}}{\omega r_2^3}} [\lambda_W k^2 - \lambda_R (1-k)^2] - 2\frac{k}{x} \tag{4.24}$$

Möhring then combines the proportionality factors of boundary layer thickness to $C_R = \frac{0.18}{\gamma_R}$ and $C_W = \frac{0.18}{\gamma_W}$ and establishes a correlation of the two factors taking into account the secondary flows along both walls. Implementing the balance of moments for the case without through-flow C'_W becomes $C'_W = C_R \left(\frac{1-k_0}{k_0}\right)^{1.75}$ with $C_R = 0.315$ which was determined by Möhring from several experimental results.

The final form of the differential equation for side gaps with superimposed through-flow can then be written as, with $\phi_{sp} = \frac{Q_{sp}}{\pi r_2^2 u^2}$:

$$\frac{dk}{dx} = 0.079 \frac{x^{1.6}}{\phi_{sp} Re_u^{0.2}} \left[(\frac{1-k_0}{k_0} k)^{\frac{7}{4}} - (1-k)^{\frac{7}{4}} \right] - 2\frac{k}{x} \tag{4.25}$$

Gülich [21] suggests a Reynolds number range for the 4.25 equation in which solutions are stable of $\phi Re_u^{0.2} > 0.002$.

Another model is presented by S. Poncet, M. P. Chauve and P. Le Gal (2004) [25]. On the basis of experiments with rotating disks in enclosed casings they established a simple correlation that links the local rotation factor to the flow coefficient of the through flow. The derivation follows a similar approach. The expression for the boundary layer thickness for the boundary on the rotating disk (Ekman layer) is found:

$$\delta_R \sim r \left(\frac{k+1}{2}\right)^{1.4} \left(\frac{\Omega r_2^2}{\nu}\right)^{-0.2} \tag{4.26}$$

And the final expression for the rotation factor which is also referred to as the "*5/7 Power law*" with the constants a and b which were experimentally determined:

$$k = 2(a\phi_{sp}Re_u^{0.2} + b)^{\frac{5}{7}} - 1 \tag{4.27}$$

A third model of the rotation factor is presented by Gülich [21]. An averaged rotation factor $\overline{k}$ is calculated from the rotation factor k_0 presented in chapter 4.4 and the flow coefficient of the leakage flow ϕ_{sp}.

$$\frac{\overline{k}}{k_0} = exp\left\{300\phi_{sp}\left(\frac{r_2}{r_{sp}} - 1\right)\right\} \tag{4.28}$$

4.5. Disk friction modeling

In his abstract on disk friction [20] Gülich presents a simplified empirical approach to assess the disk friction factor of side cavities with through-flow. The modeling of the disk friction is strongly linked to the model of the rotation factor presented in the previous section. Since the rotation factor describes the velocity ratio of the core flow in the cavity to the rotating wall, shear stresses can be linked to that characteristic quantity. Again there are two approaches presented by Gülich, one dealing with the effect of leakage with an averaged factor in this case f_L and a second one calculating the torque due to shear stresses on the rotating disks on radial ring elements with the local rotation factor determined by the iterative process previously described.

The averaged process takes into account the leakage direction, the roughness on both walls, the amount of leakage flow and the side gap geometry in the rotation factor k_0.

$$P_{RR} = \frac{k_{RR}}{\cos\delta}\,\rho\omega^3 r_2^5\left\{1 - \left(\frac{r_i}{r_2}^5\right)\right\} \tag{4.29}$$

With:

$$k_{RR} = \frac{\pi}{2Res_{ax}} + \frac{0.0625}{Re^{0.2}}(1 - k_o)^{\frac{7}{4}} f_{R,imp} f_L \tag{4.30}$$

The coefficient f_L includes a factor for the direction of leakage. The simplification can be applied in cases where $\frac{r_{sp}}{r_2} > 0.3$ and the rotation factor at the inlet is $k_E \approx 0.5$.

$$f_L = exp\left\{-350\phi_{sp}\left(\left(\frac{r_2}{r_{sp}}\right)^a - 1\right)\right\} \tag{4.31}$$

If conditions vary from the addressed range in which the simplified model can be applied, the iteratively determined rotation factor needs to be implemented. Therefore the second approach is introduced where the disk is divided into several radial segments with the dimensionless width dx. The torque is calculated with the local rotation factor at that location and $x = \frac{r}{r2}$ the dimensionless radius.

$$dM = \frac{0.287x^{3.6}\|1 - k\|^{1.75}dx}{Re_u^{0.2}}\,\frac{c_{f,Rough}}{c_{f,Smooth}}\,sign(1 - k)\rho\omega^2 r_2^5 \tag{4.32}$$

Uncertainties remain in the definition of the boundary condition with inlet swirl k_E which is dependent on the outlet geometry flow conditions and the effect of the side gap paths on the main passage. Especially in volute casings (like the example pumps) where the leakage flow is fed from low momentum boundary layer flow of the volute the interaction of outlet main flow and side gap flow can lead to deviations from the expected losses. Further uncertainties can come up in off-design load points of the pumps when large recirculation occurs. As Gülich sums up:"The last three parameters can severely influence the disk friction loss and render its calculation quite uncertain, especially with large leakage flows and at partload. Even at the best efficiency point, the tolerance of the calculated disk friction loss is estimated to be about 25%".

4.6. Conclusions for research question

The section deals with different loss models for the losses associated with secondary flows. The secondary losses (leakage loss and disk friction) models are based on the modeling of the rotation factor in the side cavity. As presented, the rotation factor models are based on semi-empirical correlations which have been compared and improved over the years with experimental test data mostly from tests on rotating disks. Geometric simplifications according to figure 4.2 of the side cavities and assumptions on wall roughness effects

as well as assumptions on inlet conditions pose limits to the models' prediction capabilities. Especially the application of the models to off-design operation in turbopumps is problematic since the circumferential velocity that enters the side gaps needs to be assumed. The flow field at low operating conditions is known to be very asymmetric and three dimensional. Effects like impeller outlet recirculation and sudden changes of locations of separated flow can be common in these conditions. The uncertainties for disk friction and leakage losses around highest efficiency operation is said to range from 25 % to 30 %. The uncertainties at off-design are not stated but can definitely be assumed higher than at nominal operation.

As mentioned before, the impact of leakage injection on the hydraulic performance is not well known in literature. Information is vague and the effects are described as to be very design dependent. Empirical or analytical models could not be found in terms of incidence losses due to leakage injection.

5

Thrust Balancing

Forces in direction of the rotational axis occur in all flow machines. The axial thrust originates from many different mechanisms. Weight acts on the rotor of the machine if not integrated in a horizontal manner. Impulse forces due to a change of direction of the axial velocity component occurs and has to be considered in radial machines. According to Bahm [11] the axial force can be determined from the conservation of momentum where $c_{ax,e}$ is the axial velocity of the exit and $c_{ax,i}$ at the inlet of the component.

$$F_{ax,Impulse} = \rho Q(c_{ax,e} - c_{ax,i}) \tag{5.1}$$

Differences in static pressure acting on rotating surfaces cause forces in axial direction as well. The sum of all the components leads to a resultant force. However, since the pressure differences over the impeller are largest and surface areas in axial direction on radial impellers are comparatively large as well the major part of axial pressure force is generated around the impeller. Since fluid in the side gaps is fed from the high pressure region at the outlet of the impeller, static pressures are high in the cavities and thus the resultant forces generated in the side gaps make up the largest part of the resulting axial thrust. Therefore literature on axial thrust and its balancing focuses on the pressure distribution in the secondary flow paths. As shown in figure 5.1 the pressure distribution on the two opposing sides differ as well as the surface areas in axial direction in the side gaps, therefore the resulting force is directed to the low pressure side if no measures to balance thrust are taken [15].

The axial force of a single side is calculated by integrating the static pressure over the axial surface area.

$$F = 2\pi \int p\, r \, \mathrm{d}r \tag{5.2}$$

The pressure distribution in the side cavities can be determined from the rotation factor which was introduced in the previous chapter. Different approaches can be found in literature to gain knowledge of the force on the individual sides. Gülich [21] proposes the use of an average value of the rotation factor if leakage is small or zero so that the force can be determined as follows.

$$F = \pi r_2^2 \left\{ (1 - x^2)\Delta p_{La} - \frac{\rho}{4} u_2^2 \bar{k}^2 (1 - x^2)^2 \right\} \tag{5.3}$$

As seen before the modeling of the rotation factor is coupled to the amount of leakage flow. If considerable leakage is present the change of rotational factor needs to be taken into account. The radial pressure distribution can be determined by solving the integral below.

$$p(r) = \omega^2 \rho \int_r^{r_2} k(r)^2 r \, \mathrm{d}r \tag{5.4}$$

For rough estimations a third approach is presented [21].

$$F_{ax} = (0.7 \; to \; 0.9)\rho g H_{tot} \frac{\pi}{4}(d_{sp}^2 - d_D^2) \tag{5.5}$$

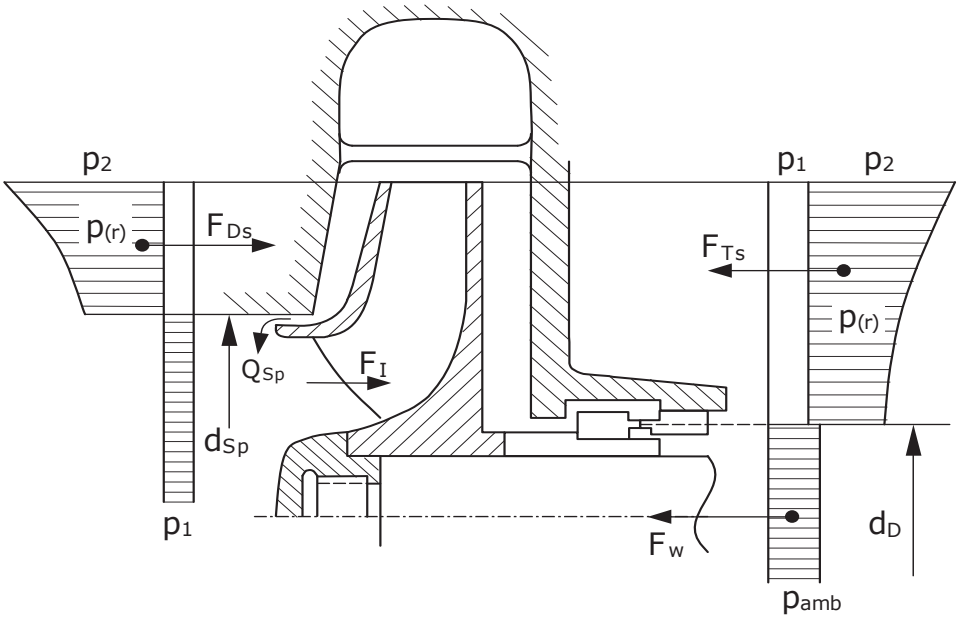

Figure 5.1: Pressure distribution around shrouded impellers [21]

The current investigations in literature deal with different types of thrust balancing. Shimura et. al. (2012) [27] focus on the dynamic behavior when balancing devices and grooves are applied on the side walls. Further balancing options are balance holes in the hub of the pressure side or balance pistons in case of multiple stage pumps, bladed side walls can reduce axial thrust and leakage as well. In this project the implementation of balance holes will be the only option considered. A model for estimating thrust with balance holes is also presented by Gülich, again a rough estimation which needs to be investigated for its applicability and its uncertainties. The most prominent uncertainties addressed in literature are still: Inlet swirl and partload recirculation.

$$F_a x = (0.1\ to\ 0.2) F_{Hy1} + F_{Hy2} \tag{5.6}$$

The modeling of forces and losses associated with secondary flows are connected to the development of the rotation factor inside the side cavities. Therefore the modeling of axial thrust generated in the side cavities is subjected to the same uncertainties as the disk friction and leakage losses. For nominal operation the uncertainties for axial thrust are said to be about 20 % and with an increasing trend towards off-design conditions. When balanced well, small uncertainties on the development of the forces of one side can lead to large errors in the resultant force. These errors can for example occur when flow conditions at the impeller outlet drastically change and the separation switches from hub to shroud. A behavior like this could lead to a shift in the direction of resulting force.

6

Conclusions for Research Project

The research question: "How can existing models capture the losses and axial thrust due to secondary flow paths?", can be answered as follows. The effect of leakage injection on the hydraulic performance is not modeled in literature and little information can be found on it. The existing models cover the secondary losses (disk friction and leakage losses) and thrust. The focus lies on the empirical characterization of the rotational flow velocity in the side gaps individually. From the rotational factor k leakage mass flow, disk friction and pressure distribution can be calculated even with leakage through-flow in the cavities. However, literature agrees that a number of uncertainties remain when calculating the effects. The main effects which cause the uncertainties are summarized below.

Axial thrust

- Boundary conditions for the analytical model, especially the inlet swirl, which is unknown, but also the static pressure at the outlet of the impeller can be different for the front and the rear side.
- The partload recirculation which occurs at the impeller exit impacts the velocity and pressure distribution, the behavior is difficult to predict and leads to larger uncertainties at low flow coefficients (Gülich: *"especially in the case of radial impellers with high specific speeds"*).
- Geometric tolerances especially with seal clearance which has a large effect on the leakage mass flow and therefore also on the pressure distribution.

These effects create uncertainties for a single side cavity the resulting thrust from the side gaps is determined by the difference of the two leakage paths. Normally these two forces should be nearly balanced so that errors in the calculation of one side leads to large uncertainties when comparing both sides. As Gülich points out, safety margins have to be applied to the bearing sizing and that simple formula should only be used if the bearings are bound to be oversized. The work at TU Munich [24] with the models for axial thrust from Gülich showed agreement of the analytical models to CFD of 16 % to 20 % for nominal load points.

Leakage mass

- Turbulence and roughness structure (and their interaction) [21] .
- The pressure difference over seal is determined by the pressure drop in the sidewall gap, which is linked to uncertainties discussed above.
- Effective clearance of the seal creates uncertainties due to manufacturing tolerances.
- Correct loss modeling of the seal geometry for loss coefficient ζ_{EA}.

The aforementioned factors make the leakage prediction uncertain. Gülich states that leakage calculations are subject to uncertainties of approximately ±30%.

Disk friction

- Partload recirculation can reduce the circumferential velocity of the fluid entering the sidewalls and increase friction in the cavities, similar to the axial thrust the onset and behavior of the partload recirculation is hard to predict and creates uncertainties especially at low flow coefficients.
- Uncertainties in leakage prediction impact the disk friction prediction.
- Roughness and turbulence modeling impacts the disk friction.

Gülich estimates the effects that create uncertainties in the disk friction calculations even at nominal load point to be around ±25%.

Numerical investigation become necessary for an estimation of the effect of leakage injection. However loss calculations from CFD are subject to uncertainties themselves.

CFD

- Largely non-uniform impeller outflow creates uncertainties in loss calculations.
- *"The influence of roughness is difficult to evaluate because of the interactions between turbulence and velocity profiles"* [21]

Loss calculations from CFD are considered uncertain to about 10 % [21].

The presented models fail to capture all loss effects due to secondary flow paths and are subject to high uncertainties especially at partload operation. A numerical model with improved prediction capabilities is needed to help estimating losses and thrust in early stages of the design process.

7

Methodology

7.1. Research plan

In the course of the literature review it becomes evident that the current loss and thrust models are subject to high uncertainties and fail to capture all effects that are connected to secondary flow paths. Therefore a research goal can be formulated that aims to improve upon the existing models.

The goal of the project is the development of a reduced order model to capture losses and thrust due to secondary flow paths in rocket engine turbopumps with improved prediction capabilities upon the existing models while maintaining lower computational costs and effort as compared to high fidelity full annulus numerical simulations.

Several questions come up that shall be answered in the course of the project in order to reach the project goal. The main questions are listed below.

- What are the differences between numerical results and experimental data and how can those be explained?
- How is the characteristic behavior impacted when leakage is injected to the main passage
- Does leakage injection have destabilizing effects on the characteristics of the pump?
- What causes the changes if present?
- How do losses scale over the range of flow coefficients?
- What are causes for possible changes in leakage mass flow, disk friction and axial thrust?
- How well are the effects predicted applying analytical models to the example case?
- Can the new reduced numerical model capture the effects with a higher accuracy?
- What are possible differences between the full annulus and the reduced numerical model?

A plan is established in order to successfully reach the project goals and to answer the subquestions.

- **Literature review:** A thorough investigation of the literature on analytical models that describe the flow and losses in sidewall gaps is done to point out remaining uncertainties and gaps in knowledge which indicate where further investigation is necessary.
- **CFD on full annulus model:** On the basis of an example liquid oxygen pump for which test data on the performance are available, numerical flow simulations are performed. These simulations feature a full scale pump unit with inducer, impeller and volute. The simulations will be run for varying flow coefficients to capture the off-design performance of the pump. Results will be compared to experimental data of the pump on the same flow coefficients.

- **CFD on full scale model with leakage paths:** Simulations will be run for the same pump with leakage paths and seals. The model shall show the effects on the global performance data as well as the individual loss mechanisms. The results will be compared to the full model and the experimental data, to evaluate the impact of leakage on the performance and whether results are closer to the experimental data. The losses are quantified to identify the largest effects due to leakage. The thrust generated in the side cavities will be analyzed in the investigated operating range.
- **Development of numerically reduced model**: In the early stages of the design process a simplified model of the side cavities and its interaction with the pump passage is useful to estimate the performance and axial thrust. The model shall cover the relevant effects but be easier to set-up and quicker to simulate than the full annulus calculations.
- **Development of analytical model from literature**: Based on the models presented in literature an analytical tool can be implemented that calculates the amount of leakage mass flow, disk friction losses as well as axial thrust in the cavities.

7.2. Model setup

7.2.1. Full-annulus model

In this section the build up and working principle in *ANSYS CFX* for the numerical full scale model is presented. The mesh generation and the mesh quality is shown as well as the choice of boundary conditions for the different domains. The usual work flow for a numerical model can be seen in flow chart 7.2.1.

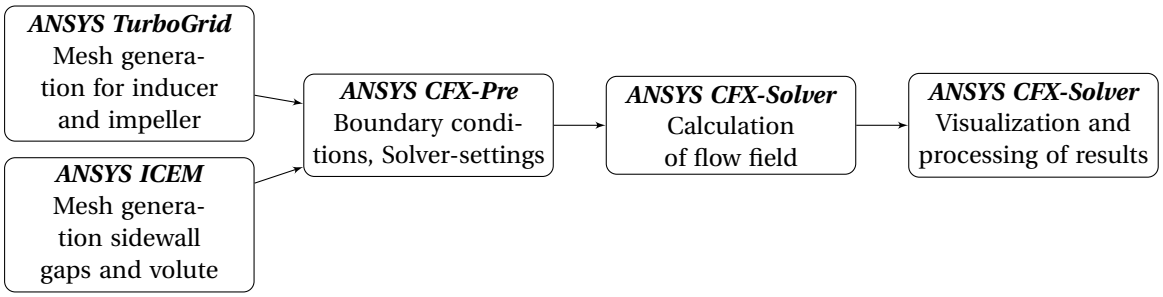

The geometry for mesh generation is taken from the CAD-model of the pump. The full scale model features the geometry in 360° including inducer, impeller, volute and side cavities to capture possible asymmetric effects stemming from the volute tongue or the inducer outlet flow. The geometries of impeller and inducer are imported by the meshing tool *ANSYS TurboGrid*, where the calculation domain gets discretized by a division into finite volume elements. Mesh generation for sidewall gaps and volute is performed in the tool *ANSYS ICEM*. Boundary conditions and settings for the numerical simulation are defined in the preprocessor *CFX-Pre*. The stationary calculation of the three dimensional flow field in the geometry follows in the *CFX-Solver* and results are evaluated in the *CFX-Post*.

Mesh generation

In case of *ANSYS TurboGrid* the domains are meshed in a structured blocking manner. >Elements consist of hexahedrons and have to be aligned with the geometry. In *ANSYS TurboGrid* the structured mesh is created following algorithms that automatically generate the topology and the elements from given geometries. This way meshing processes can be sped up. When generating meshes the resolution of the boundary layer flow is important so that effects of the flow around the blades and other walls can be investigated properly. Because of this, regions close to no-slip walls feature small cells. A common measure for the quality of the mesh resolution is the dimensionless wall distance $y^+ = \frac{u_\tau y}{\nu}$. The $u_\tau = \sqrt{\frac{\tau_w}{\rho}}$ represents the friction velocity, y the actual wall distance and ν the kinematic velocity. The first cell at the wall should have a value close to one. In cases of very large shear stresses due to strong velocity gradients the value of one is hard to maintain at every location on the wall. For this case the solver features wall functions which reduce the error made when resolution is not good enough. A quality mesh features grid lines that follow the streamlines and preferably orthogonal edges, minimal and maximal angles of 15° and 165° are common mesh criteria for radial machines. Furthermore the difference in element size should not change drastically from one cell to the next.

Gülich gives the reference factor of 2 for the dimensions of the cell. The *ANSYS ICEM* tool is used for the sidewall gaps and the volute. The sidewall gaps feature a structured mesh and the blocking topology is manually created. The volute is discretized in an unstructured fashion. The mesh does not feature a defined topology and the cell geometry is not even. The meshes get created automatically and can be adapted to complex and asymmetric geometries suitable to a volute. The use of prism layers helps creating higher resolution close to the walls and perpendicular to the walls while still keeping number of elements within limits.

Inducer

A single inducer passage is meshed with *ANSYS TurboGrid*. The inducer features very sharp leading -and trailing edges and a gap between casing and blades. The geometry of the blades is imported as curve-files which feature infinitely sharp edges. The meshing tool fails to generate cells close to the edges without creating overlapping elements. Therefore the curve files have been manipulated to feature a rounded edge with a minimal radius as can be seen in figure 7.2. To model the injection of the leakage flow paths, an interface surface needs to be defined. The injection of leakage in the investigated pump takes place over the tip of the inducer blades close to the trailing edge. Figure 7.1 shows a simplified meridional scheme of the injection location. Including this feature to the model could have led to a major increase of workload and time due to the complex meshing around the trailing edge of the inducer and the tip gap. Therefore the inducer blade geometry has been shifted upstream to allow for a small inducer outlet domain on which the interface can be defined. The dimensionless values that determine the change in geometry can be taken from table 7.1. The y^+-distribution for all the components is shown in figures in the appendix A.5.

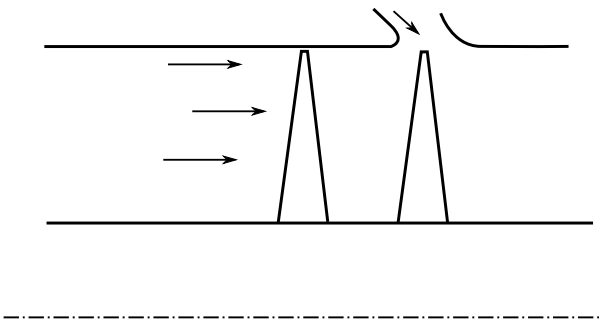

Figure 7.1: Schematic meridional view of inducer blades and leakage injection

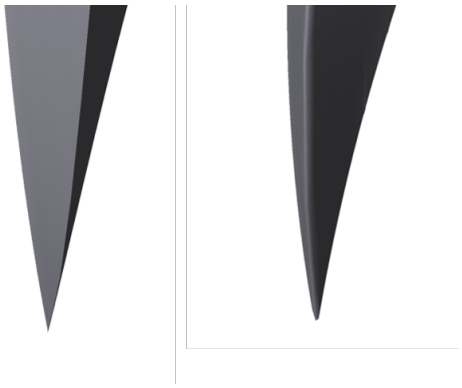

Figure 7.2: Trailing edge of inducer blade; left: Sharp; right: Rounded

Including the aforementioned changes the full mesh and cuts can be seen in figure 7.3. The element quality at the trailing and leading edge is still lower than the limits presented in the section above.

The parameters for the mesh quality can be taken from table 7.1.

Table 7.1: Mesh statistics inducer

Parameter	Value
Minimum face angle	2.2°
Maximum face angle	178.3°
Maximum element volume ratio	95
Minimum volume	$2.4965e-18$ $[m^3]$
Maximum edge length ratio	1672
Minimum y^+	0.12
Maximum y^+	54
number of cells	1638296
Shroud tip gap width by span	1 %
Number of elements in tip gap	24
Trailing edge radius by span	0.125 %
Upstream shift by span	15.6 %

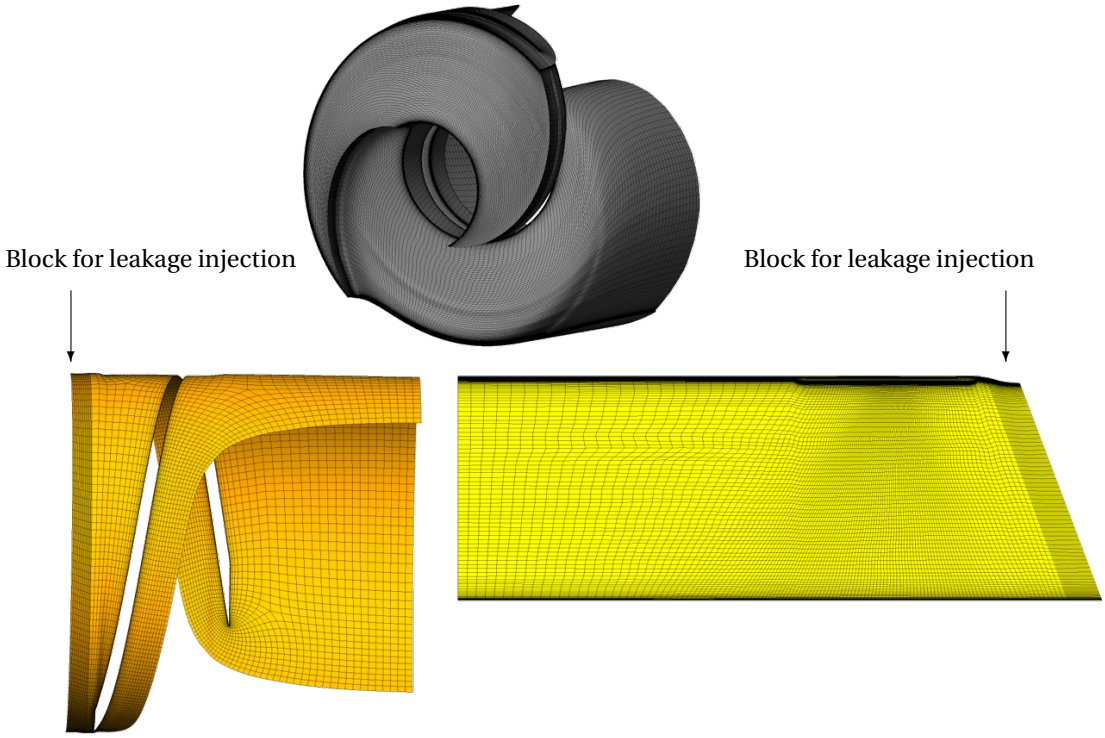

Figure 7.3: Top: Inducer mesh; Left: Topology layer close to shroud; Right: Meridional view

Impeller

The impeller mesh is created with *ANSYS TurboGrid* as well. Similar to the inducer mesh the impeller geometry is imported using curve-files. The impeller is shrouded so there is no tip gap. Some geometry modifications have to be made in order to be able to successfully create the mesh. When the trailing edge of the blade aligns with the hub and shroud curve the meshing tool fails to generate a mesh for the exact geometry. Therefore the hub and shroud curve are extended enough so that the creation of the mesh succeeds as shown in figure 7.4. The analysis of the effect of this extension has not been performed in the course of this project.

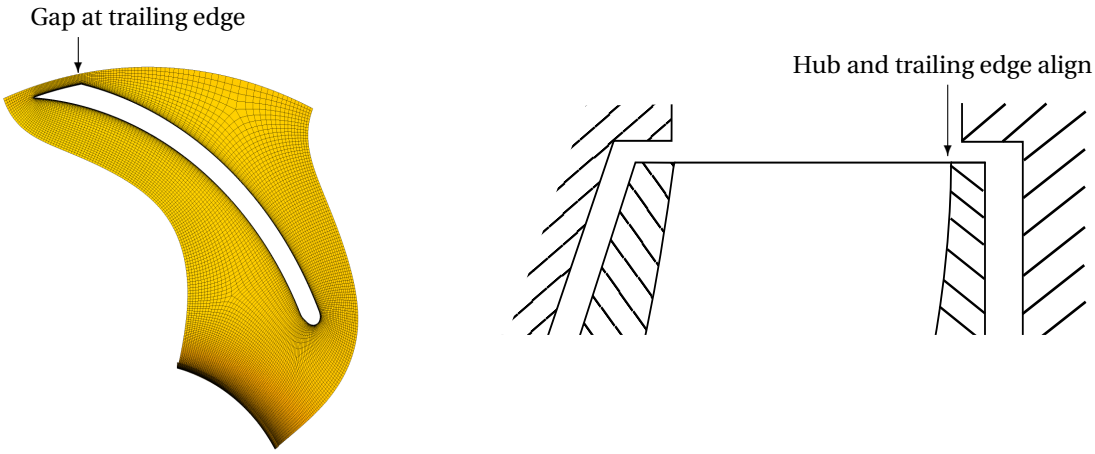

Figure 7.4: Left: Mesh at midspan; right: Geometry of impeller rotor

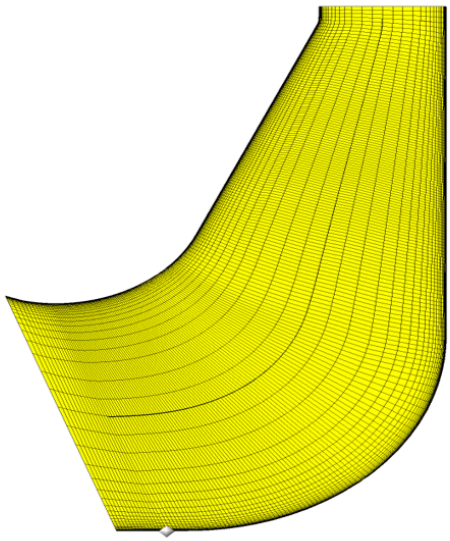

Figure 7.5: Meridional cut of the impeller mesh

Similar projects at TU Munich are evaluating the impact on the performance when a slim gap is included using unstructured meshes for the impeller geometry. In order to allow the leakage through the balance holes to be reinjected to the impeller passage an interface needs to be created. For that an interface surface needs to be defined that attaches to the balance hole domain. For that the mesh is exported from *TurboGrid* and imported with the meshing tool *ANSYS ICEM*. The mesh faces are selected manually at the hub of the domain to allow for the interface definition in *CFX-Pre*. Table 7.2 shows parameters for the mesh quality.

In figure 7.5 a meridional view of the impeller mesh is shown.

Table 7.2: Mesh statistics impeller

Parameter	Value
Minimum face angle	9.23°
Maximum face angle	172.6°
Maximum element volume ratio	10.2
Minimum volume	$9.184e-18$ $[m^3]$
Maximum edge length ratio	945
Minimum y^+	0.02
Maximum y^+	8
Number of cells	1057700
Trailing edge gap by outlet radius	2.2 %

Volute

The mesh for the volute is created with *ANSYS ICEM*. The volute attaches to the impeller outlet flow and to the side gaps, in both cases the flow field at the intersection is expected to be highly non-uniform and interfaces can create convergence problems and lead to physically incorrect results. In the course of the project the interfaces with the volute have been a major factor which impacts results and convergence. A stable simulation was only achieved when creating a coarse and unstructured mesh in the volute domain. The unstructured mesh consists of tetrahedra and prism layers along the no-slip walls.

The mesh statistics are presented in table 7.3, in figure 7.6 a three dimensional mesh of the volute is shown.

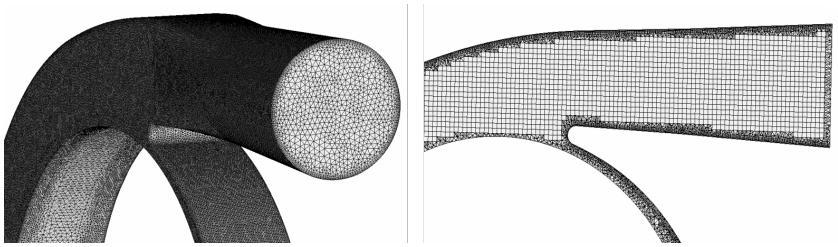

Figure 7.6: Volute mesh

Table 7.3: Mesh statistics volute

Parameter	Value
Maximum edge length ratio	4.10
Minimum y^+	5
Maximum y^+	381
Number of prism layers	8
Number of cells	1363760

Leakage Front& Leakage Back & Balance Holes

The meshes for the side gap geometries including the balance orifices are done with *ANSYS ICEM*. The sealing paths that are included in the geometry have to be modeled and meshed as well. The investigated pump features floating ring seals which are modeled with a slim annular gap in the leakage paths. First approaches with unstructured meshing methods failed because of these slim gaps in the seals. In order to resolve the boundary layers in the sealing paths a minimum of 12 to 16 cells shall be implemented.

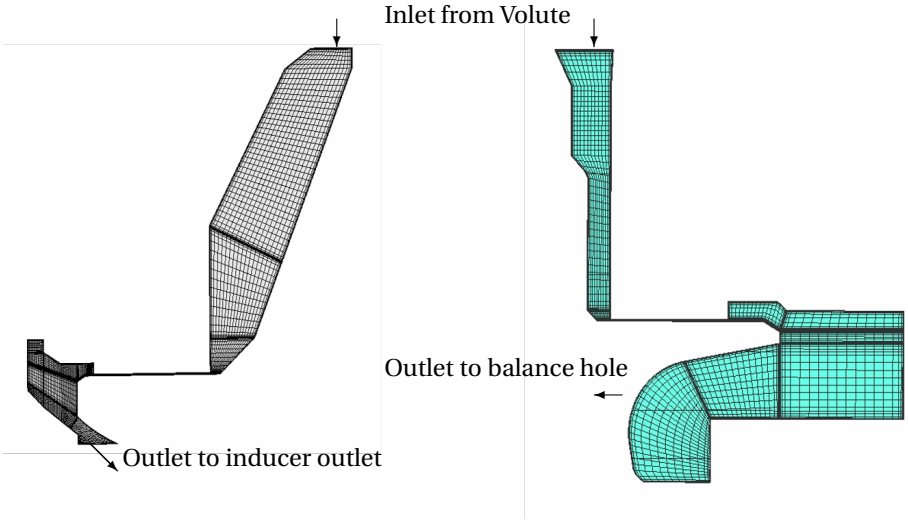

Figure 7.7: Two dimensional side gap meshes

The geometry of the side gaps could easily be simplified to a rotational symmetric path if holes in the real geometry for measurement instruments are not taken into account. The blocking and the topology can then be established in two dimensions. Fillets in the paths are not modeled. It is a common simplification in meshes for turbomachine passages, since the modeling of fillets in tools like *TurboGrid* is connected to an enormous amount of effort. The side gap in the back features complex geometry downstream of the sealing path around the rotor. The geometry is reduced and the slim passages around the rotor leading to a second seal are not modeled. The meshes for the side gaps in two dimensions can be seen in figure 7.7. The meshes are then extruded to 360° and three dimensions.

The balance holes are also done with *ANSYS ICEM*. There are modeled as simple round ducts and meshed with a three-dimensional blocking topology which features o-grids. The mesh of the hole can be seen in figure 7.8.

Table 7.4: Mesh statistics sidegaps

Parameter	Value front	Value back
Minimum Face Angle	22.16°	9°
Maximum Face Angle	157.8°	153.33°
Maximum Element Volume Ratio	45.8	8.77
Minimum Volume	$9.9e-17$ $[m^3]$	$3.52e-16$ $[m^3]$
Maximum Edge Length Ratio	870	1200
Minimum y^+	0.002	0.012
Maximum y^+	14	47
number of cells	3824280	2439000

Figure 7.8: Balance hole mesh

Pre-Processing

The stability of numerical simulations is not only dependent on the mesh quality but also on the choice of boundary conditions and turbulence model. The simulations will be performed with the SST model (Menter's Shear Stress Transport) turbulence model. It is a common two-equation model. It combines the advantages of the k-omega model and the k-epsilon and uses k-omega for boundary layer flow and k-epsilon for free shear flow. For numerically solving the RANS-equations, boundary conditions on inlet and outlet as well as at the walls are needed to create a system of equations which is then solved by the solving tool. The different boundary conditions are presented in the following:

- **Inlet:** The inlet boundary condition is set with a constant value of total pressure for all operating points. The inlet direction of the flow is defined purely axial. The inlet surface is located 55 % of the inducer span upstream of the inducer blades.
- **Outlet:** At the exit of the volute the total mass flow through the geometry is defined. The behavior of the system shall be investigated at nominal mass flow but also at higher and lower operating conditions. Therefore the value of the mass flow at the outlet is changed so that the flow coefficients range from $\Phi/\Phi_{nom} = 0.45$ to $\Phi/\Phi_{nom} = 1.3$.
- **Periodic boundaries:** Periodic boundaries are not required since the full 360° geometry is calculated.
- **Walls:** All domains are modeled in the rotating frame of reference except for the volute. The rotating walls are assigned with a no-slip and smooth wall condition. Since the casing walls in the leakage paths and the inducer are non-rotating these are assigned with the counter rotating condition in the rotating domains. The walls in the volute feature the no-slip condition. When leakage paths are not included in the model it is assumed that the secondary flow paths are closed and also the tip faces of hub and shroud of the impeller are non rotating so that these boundaries in the volute are defined as no-slip walls. When the secondary paths are included to the model, the tip faces of hub and shroud feature the free-slip condition.
- **Interfaces between domains:** Between calculating domains interfaces have to be defined which allow the exchange of information. Between rotating and non-rotating domains the pre-processor *ANSYS CFX-Pre* gives two options. The mixing plane approach transfers the information of the flow properties

after performing a circumferential average. When the frozen rotor approach is used the flow information are not averaged but the change of relative position between two domains is not taken into account. The interface choice between impeller and volute proves to be a crucial parameter in the setup. When frozen rotor is chosen the flow field that gets calculated becomes extremely asymmetric due to the upstream effect of the volute tongue. The flow coefficient for each passage changes because of a difference in downstream local pressure in the volute passage [21]. However the frozen rotor method considers only a single position of the impeller passages relative to the asymmetric volute. Multiple frozen rotor positions are not investigated due to high computational effort and time constraints. Therefore the interface method of mixing plane was picked between volute and impeller. Since the inducer and impeller are driven by the same shaft the relative position inducer blades and impeller blades is maintained. The frozen rotor interface choice is therefore justified. To avoid asymmetric injection through the balance holes the interfaces between the back leakage and the balance hole domains as well as the holes to the impeller passage are calculated with the stage mixing approach. Between volute and both leakage paths the frozen rotor method is chosen.

The simulation is performed with the high resolution scheme on a physical time scale of $3.5e^{-5}$ which is according to the recommendations from the *CFX*-manual [16]. The simulated fluid is water at 20° which agrees to how the pumps are usually tested. Simulations are stopped once the global characteristics reach constant values with remaining fluctuations and the averaged residuals are lower than $RMS = 1e^{-3.5}$.

Post-Processing

In order to investigate the individual components closer, it is reasonable to define planes on which the averaging methods are applied. The planes are positioned at the beginning and end of the component, however, in order to avoid inaccurate results created by interface or outlet methods, the analysis planes are positioned upstream of the interface to the downstream component. In figure 7.9 the analysis planes are presented and numbered.

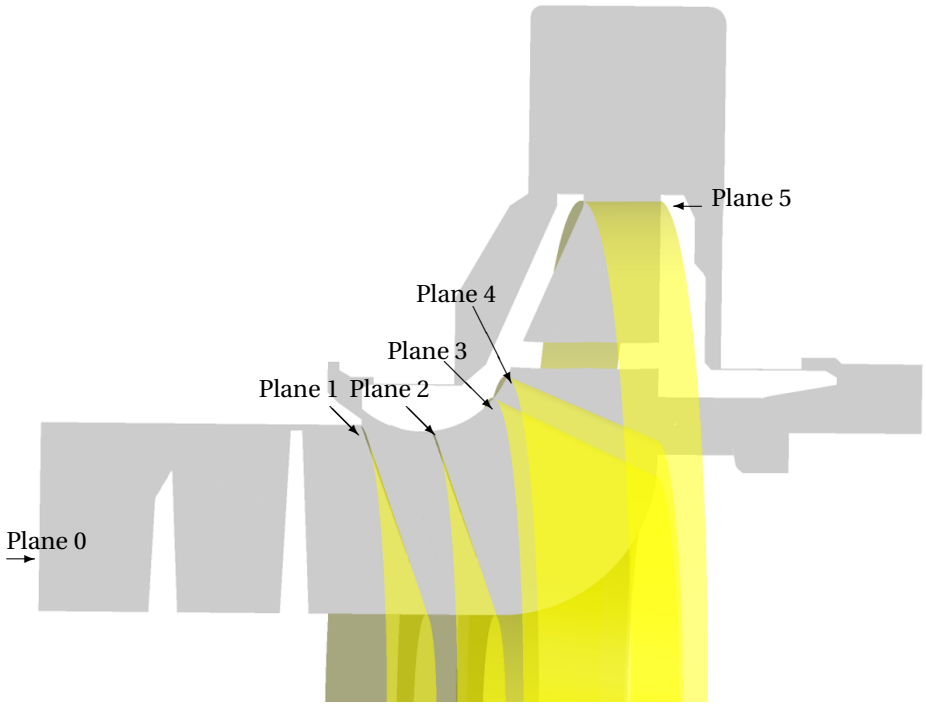

Figure 7.9: Analysis planes

The table 7.5 gives further details to positioning and purpose of the planes.

In the course of the report the data is presented in a non-dimensional way. The methods of how the values are treated and processed is listed in table 7.6.

Table 7.7 presents the efficiency definitions that were used in the course of the project.

Table 7.5: Plane definition

Plane	Positioning	Purpose
Plane 0	Inducer Inlet	Inlet and reference conditions
Plane 1	1 % downstream inducer blade TE	Inducer outlet conditions before injection
Plane 2	Narrow cross section	Impeller inlet conditions after injection
Plane 3	10 % upstream impeller LE	Impeller reference conditions (for blade loading)
Plane 4	1 % upstream impeller LE	Incidence plane
Plane 5	2 % downstream impeller TE	Impeller outlet conditions
Plane 6	2 volute outlet cs-diameters upstream of outlet	Volute outlet conditions

Table 7.6: Methods of non-dimensionalizing

Value	Non-dimensional	Method
Velocities	w/u_2	
Pressure	$c_p = \frac{p-p_3}{0.5\rho w_3^2}$	
Pressure ratio	$p_{tot}/p_{0,tot}$	
Reduced static pressure	$p - 0.5\omega^2 r^2$ [Pa]	
Reduced static pressure coefficient	$c_{p,reduced} = \frac{p_{reduced}-p_{reduced,3}}{0.5\rho w_3^2}$	
Mass flow	$\Phi = C_{m2}/u_2$ Φ/Φ_{nom}	
Incidence	$\beta_{Blade} - \arcsin\left(\frac{c_{m,4}}{w_4}\right)$ [°]	
Loss coefficient	$\zeta = \frac{\Delta p_{tot}}{0.5\rho u_2^2}$	
Head	Ψ/Ψ_{nom} $\Psi = 2gH/u_2^2$	$H = \frac{p_{6,tot}-p_{0,tot}}{\rho g}$
Power	$P/P_{nom,CFD}$	$P = \omega \sum M_{A,rotating}$
Axial force	$F/F_{nom,CFD,leakagefront}$	$F = \int p_{st} dA_{ax,rotating}$

Table 7.7: Efficiency definitions

Efficiency	Equation
Volumetric efficiency	$\frac{\dot{m}}{\dot{m}+\dot{m}_{sp1}+\dot{m}_{sp2}}$
Overall efficiency	$\frac{\dot{m}gH_{tot,6,0}}{P_{Inducer}+P_{Impeller}+P_{RR}}$
Hydraulic efficiency impeller	$\frac{(\dot{m}+\dot{m}_{sp1}+\dot{m}_{sp2})gH_{tot,5,2}}{P_{th}}$

Table 7.8: Averaging methods

Averaging method	Property
Mass average	Velocity, total pressure, entropy
Area average	Static pressure, force
Mixed out average	mixing losses, velocity, total pressure

In table 7.8 the averaging methods for the different properties are presented based on the theory from chapter 2.5. When applying the mixed out averaged condition to the leakage injection and the impeller exit flow the total pressure loss due to downstream mixing is of interest. The method is applied on the velocity in stationary frame. Continuity equation shall be used to determine the averaged velocity after mixing, however in rotating geometries the continuity equation can only give information on the meridional velocity. Therefore the mass flow averaged velocity in stationary frame is used. The mixed-out method applied like

described provides reasonable and meaningful results when compared to the impeller-model where the only losses that occur in the diffuser are the downstream mixing losses of the impeller outflow. These are close to the mixed-out losses determined by the mixed-out averaging.

The sidewall gaps are investigated in terms of velocity and pressure distribution. Planes and polylines are defined with constant radius to extract information on the static pressure on the rotor wall and the average circumferential velocity for the rotation factor and velocity in relative frame of reference for Rossby number.

7.2.2. Impeller-model

The choice of a reduced model was made based on the effects investigated on the full scale model. The effect of leakage on the inducer head curve 8.17 can be neglected, therefore the inducer is not modeled in the reduced geometry. To achieve similar inlet conditions for the impeller the outlet velocity profile of the inducer is taken into account. Including the volute to the numerical model requires a 360° degrees simulation since no periodicity can be placed to the asymmetric geometry. The key differences in the models can therefore be expected to be found in the inlet velocities to the sidewall gaps. Instead of the volute and inducer the model will feature frictionless inlet and outlet domains with constant cross sections. Because leakage injection through the pressure relief orifices occurs only in every second passage the model needs to feature two passages one with injection and one without. When no leakage is present only a single impeller passage is simulated. The interface between the frictionless diffuser and the impeller passage features the mixing plane model for reasons of consistency to the full-annulus model. In this case however the frozen rotor model is more reasonable since the outlet geometry is symmetrical and therefore changing the relative position between rotor and outlet domain would be meaningless.

Impeller mesh

The impeller domain features the same settings as the mesh for the full scale model. A block at the outlet is added to the impeller domain that allows for the attachment of the leakage flow paths. The mesh statistics and figures related to the impeller mesh can be seen in section 7.2.1.

Inlet mesh

The mesh is created in *CFX TurboGrid*. The hub and shroud curves were modified to extend one impeller outlet radius upstream of the impeller inlet. The mesh statistics are presented in chart 7.9.

Table 7.9: Mesh statistics inlet domain

Parameter	Value
Minimum Face Angle	15°
Maximum Face Angle	178.2°
Maximum Element Volume Ratio	2
Minimum Volume	$9.48e-16$ [m^3]
Maximum Edge Length Ratio	200
number of cells	154818

Outlet mesh

Table 7.10: Mesh statistics outlet domain

Parameter	Value
Minimum Face Angle	23.6°
Maximum Face Angle	175.9°
Maximum Element Volume Ratio	517
Minimum Volume	$3.49e-15$ [m^3]
Maximum Edge Length Ratio	2100
number of cells	56500

The method for the outlet domain is similar. The hub and shroud files are manipulated so that the out-

let extends one impeller outlet radius downstream of the impeller outlet. Furthermore the cross sectional area is kept constant so that because of the increasing radius hub and shroud converge. Since the walls of the diffuser feature the free-slip boundary condition measures for wall refinement are not taken. The mesh statistics are presented in table 7.10.

Leakage Front & Leakage Back & Balance Holes

The inlet geometry of the secondary flow paths have to modified since these are no longer connected to the volute but directly to the impeller outlet. The inlet to the side gaps is designed symmetrically which is another change to the original geometry since the volute channel height is varying over the circumference. The inlet width was designed with 3.5 % of the outlet radius. The meshes were done with the same method in *ICEM CFX* on a two dimensional basis and then extruded. The mesh statistics can be taken from the following chart 7.11.

Table 7.11: Mesh statistics side gaps

Parameter	Value front	Value back
Minimum Face Angle	22.16°	9°
Maximum Face Angle	157.8°	153.33°
Maximum Element Volume Ratio	45.8	8.77
Minimum Volume	$9.9e-17$ $[m^3]$	$3.52e-16$ $[m^3]$
Maximum Edge Length Ratio	870	1200
Minimum y^+	0.002	0.012
Maximum y^+	14	47
number of cells	475026	312002

The next figure 7.10 shows the overall model and the mesh lines on the boundary surfaces.

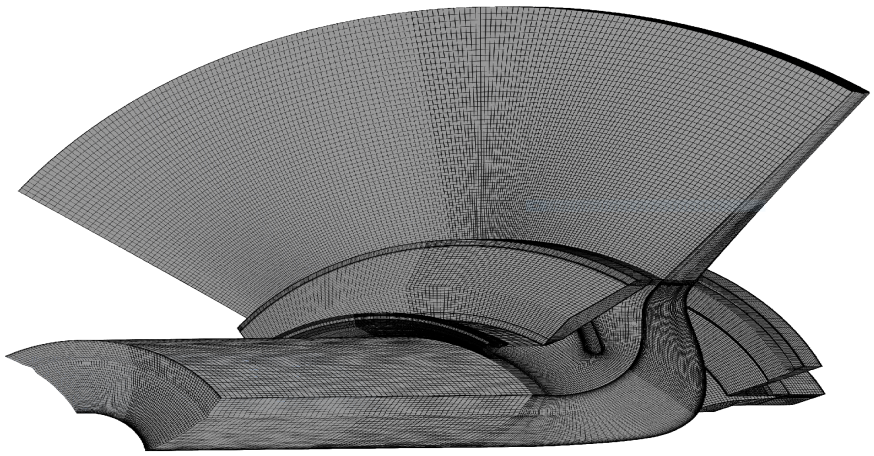

Figure 7.10: Impeller model

Pre-Processing

The setup for the simulations agree well to the setup for the full scale model. The same turbulence and interface models are used. Inlet and outlet domains feature free-slip walls. All the domains feature periodic boundary conditions at 45° or 90° respectively. The outlet boundary condition is mass flow of the respective operating condition.

For the inlet condition the total pressure is defined according to the total pressure at the exit of the inducer. Furthermore the velocity profile of the inducer exit is exported (plane 1) and defined as inlet velocity directions for the reduced model. The inducer features reverse flow at low flow coefficients, which cannot be taken as inlet condition for the numerical solver. Therefore the outlet velocity profile for nominal operation is taken for all operating conditions. The investigated geometry features an uneven number of inducer and impeller blades. The inflow for the individual passages in the full scale model varies around the circumfer-

ence. When calculating on a single impeller passage the 360° velocity profile is circumferentially averaged to achieve an averaged impeller performance. The velocity directions are imported with *ANSYS CFX-Pre* in polar coordinates.

8

Full-Annulus Model

In this chapter the results of the full annulus geometry are presented. In the following section the performance of the pump without the modeling of the secondary flow paths will be shown followed by a section that deals with the full scale model including both leakage paths. The global characteristics are compared to experimental test data.

8.1. Results of model without sidewall gaps

8.1.1. Global characteristics

Before analyzing the local flow field of the individual loading points the global characteristics shall be presented. Operational requirements change for rocket engine turbopumps for example during start-up. Generally a stable characteristic curve features always decreasing head coefficient with increasing flow coefficient.

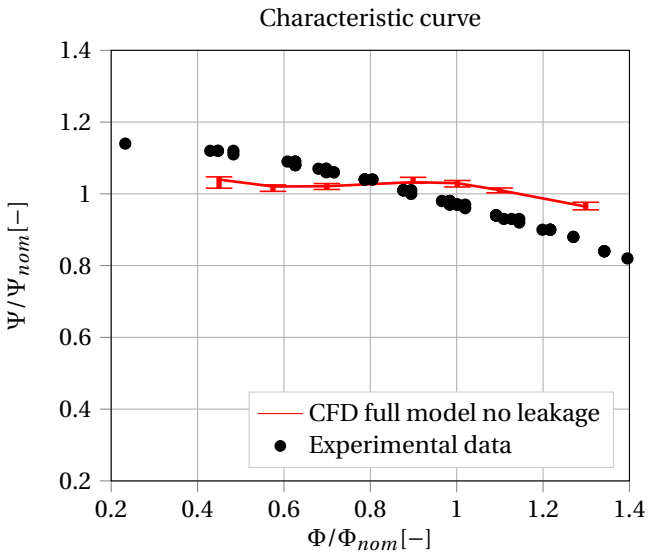

Figure 8.1: Characteristic curve of experiments and CFD

In the experiments static pressure is measured 5 diameters upstream of the inducer and 5 diameters downstream of the volute total pressure is determined with the meridional velocity from the continuity equation. The numerical domains do not extend 5 diameters upstream and downstream of the components which makes a direct quantitative comparison of the data difficult. However the stability and shape of the curves shall be compared and the differences investigated. The experiments were performed on lower rotational speeds and mass flow and for a larger range of flow coefficients. In figure 8.1 the experimental values and the numerical results are presented. The plot for the numerical results includes small error bars which are

based on the remaining fluctuations of the global performance data at the end of each simulation. Diverging results between experiments and numerical tests are common and expected countless factors play a role that increase modeling errors in numerical simulations. The major differences can be enumerated as follows.

- **Stationary simulation**: According to Gülich the interaction between volute and impeller can only be captured well in transient simulations.
- **High residuals**: Connected to the low mesh quality around some extreme geometric features the residuals of the simulations remain high $RMS \approx 1e^{-3.5}$ when properties reach constant values.
- **Turbulence Modeling**: The effect of different turbulence models on the performance is unknown since only the *SST*-Model was used, large regions of separation and curved channels create difficulties to the model to capture the effects correctly.
- **Interface problems**: Connected to the stationary simulation, an interface choice needs to be made between rotating and non-rotating domains. Neither of the choices can represent the behavior and on top of that can create issues when large recirculation is present. This point will be further explained in the following.
- **No cavitation**: Cavitation has a detrimental effect not only on the service life of the component but also on the performance of the pump if present, the effects of cavitation and flow instabilities on the performance have been investigated in a lot of research e.g. [1] and [7].

Saddle-type head curve

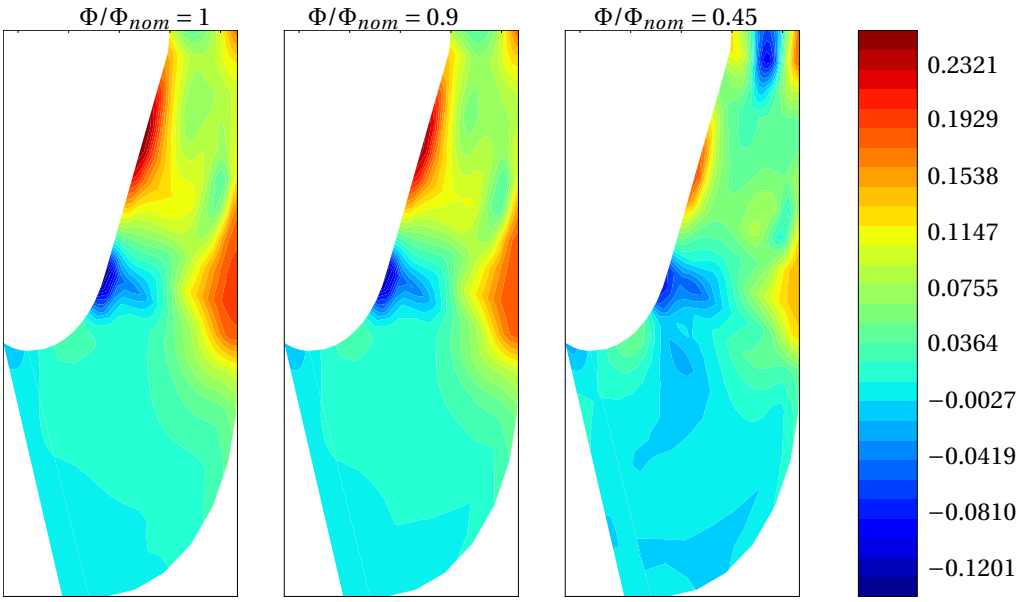

Figure 8.2: Radial velocity $c_{rad}/u2$ on meridional surface impeller

Figure 8.1 clearly shows that the head curve derived from experiments features stable characteristics. The simulation data however feature an instability that Gülich describes as "saddle-type instabilities". Around nominal flow coefficient the results are close to the experiments but at overload and low partload the discrepancy increases to about 10%. As described the quantified differences play a minor role compared to the stability behavior from simulations and experiments. There are multiple hypothesis for this kind of behavior of the simulations. The behavior at partload is subject to very complex and three-dimensional flow patterns. However Gülich indicates mechanisms that are typically found in pumps that feature saddle-type instabilities. A sudden change in flow behavior at the impeller exit can cause the head curve to rise. This change can be the sudden onset of flow recirculation into the impeller due to large separation at low flow coefficients or a sudden change of location of separated flow or recirculation. Figure 8.2 shows the radial velocity averaged over the circumference and on the meridional view. It can be seen that indeed at lowest operating load the impeller outlet features recirculation. Gülich explains the increase in head at low flow coefficients as follows:

"The recirculation zone blocks a part of the impeller outlet section. In the diffuser, too, recirculation blocks a part of the cross section, which might improve the pressure recovery in the healthy flow" [21].

A second hypothesis is that the difference between experiments and numerical results comes from the effect of secondary flow paths on the flow in the passage. According to literature the characteristic behavior of the pumps at partload is susceptible to slight changes of the impeller inlet flow. Leakage injection changes the flow field of the approaching flow and also in the passage through balance hole injection. This hypothesis can be checked in the next section when the secondary flow paths are modeled as well.

A third explanation to the instabilities is that the individual components feature local minima or maxima in hydraulic performance. When these overlap instable characteristics can be the result.

Furthermore Gülich points out that pumps with volute casings are less susceptible to these instabilities. That underlines that the pressure recovery in the collector has major impact on the stability of the characteristic curve. When the impeller outlet pressure varies over the circumference the local flow coefficient of the individual passages changes which creates a sort of averaged behavior of the impeller since every passage behaves differently. The described effect is not modeled with a mixing plane interface choice since the upstream and asymmetric effect of the volute tongue on the impeller flow is circumferentially averaged.

A last theory comes up when investigating the flow field and the interfaces of the full scale simulations. As can be seen in figure 8.3 the interface closes part of the passage when recirculation is expected. In figure 8.4 the amount of closed area of the interface is shown with changing mass flow conditions. According to the CFX-Manual [16] the mixing plane is able to deal with small amounts of recirculation but at partload high amounts of flow enter the impeller passage which the mixing plane prevents. So according to the manual: "Stage analysis is not appropriate when the circumferential variation of the flow is significant relative to the component pitch (for example, a pump and volute combination at off-design conditions)" [16]. In the course of the report the different hypothesis shall be investigated in more detail. The closing shown in figure 8.3 shows local differences around the circumference the closing occurs in all the cases downstream of the volute tongue. As can be seen in the axial cut of the volute the flow around the tongue is forced inwards directed to the impeller exit. It is a common behavior that the tongue incidence changes due when mass flow is lowered. When flow angles turn inwards locally the interface downstream of the volute tongue closes since the recirculation into the impeller outlet cannot take place at the same time as an averaged outlet flow coming from the impeller. The mixing plane interface approach cannot cope with that amount of recirculation and blocks the interface downstream of the volute tongue.

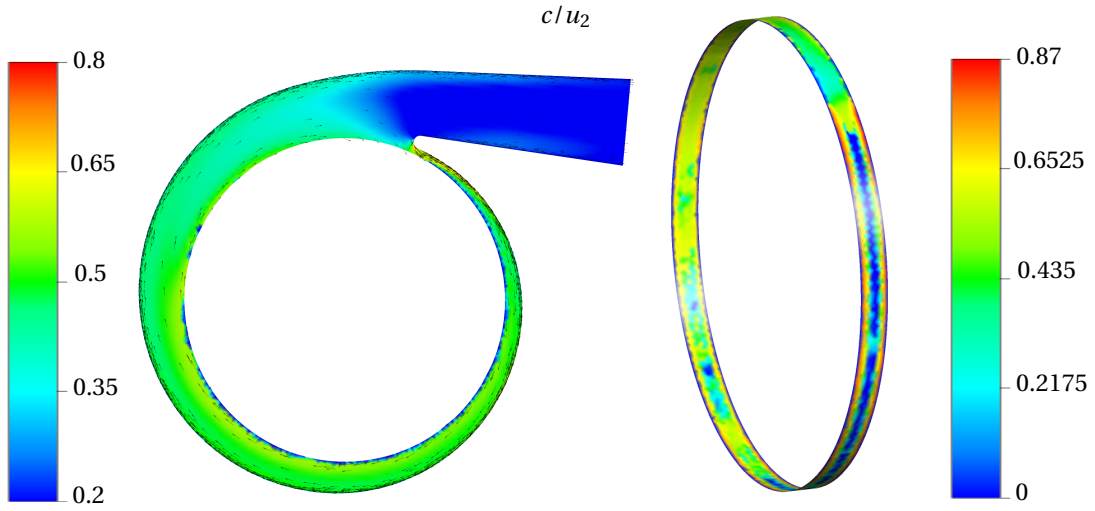

Figure 8.3: Closed area of impeller to volute interface at $\Phi/\Phi_{nom} = 0.45$

Shaft power and efficiency

The global characteristics of the pump in terms of shaft power and efficiency are presented in the following figure 8.5. It can be seen that the shaft power determined from the numerical results is generally lower

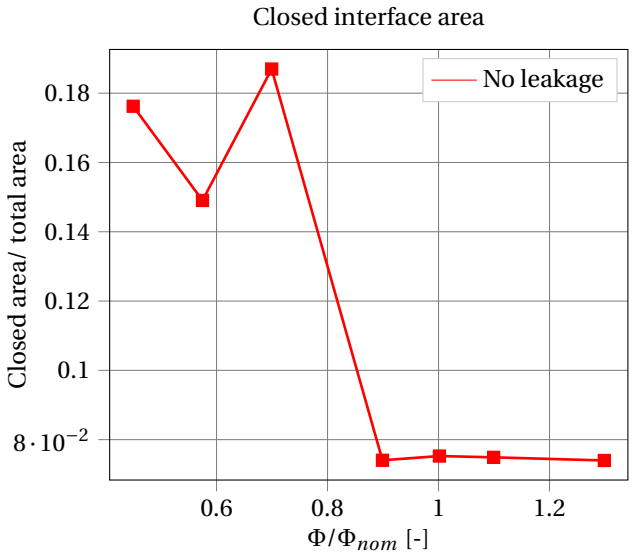

Figure 8.4: Closed interface area ratio

than the experimental values. The difference to the experiments increases with decreasing flow coefficient from 13 % to 22 % of the nominal shaft power from CFD. Due to disk friction and an increased mass flow in the impeller the power and efficiency level is expected to be closer to the experimental results when the secondary flow paths are modeled as well. In the efficiency curve one can see that the efficiency from CFD is overpredicted. This is linked to lower shaft power and for high flow coefficients to the higher useful work determined from numerical simulations. The efficiency in the experiments is about 18 % lower comparing with the efficiency from numerical tests around nominal loading conditions and 14 % lower at partload. The highest efficiency in the experiments is reached around the nominal flow coefficient in the numerical simulations the highest efficiency is reached at slightly overloaded conditions.

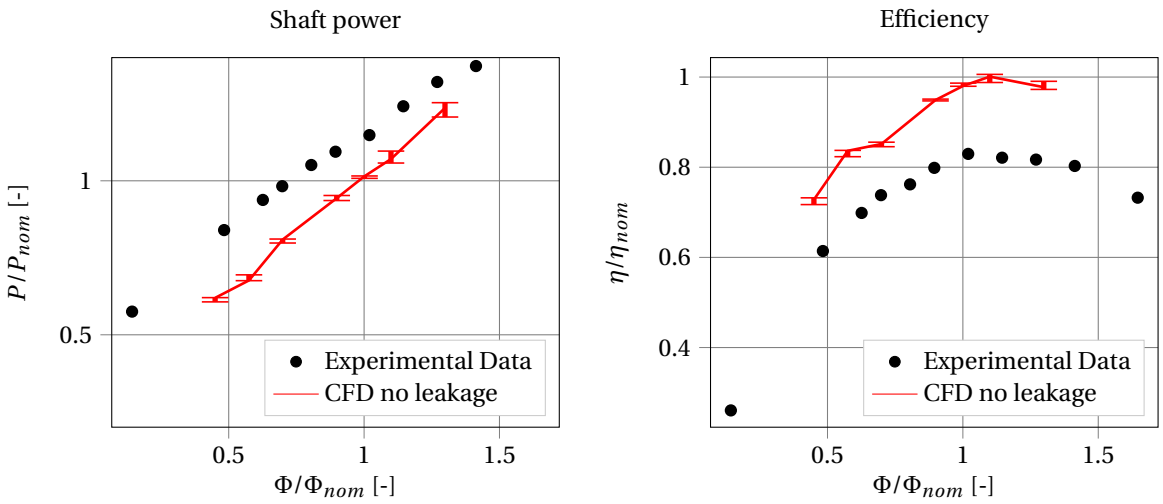

Figure 8.5: Shaft power and efficiency characteristics

Component analysis

A closer look at the performance of the individual components helps understanding the shape of the characteristic curve better. The system has been evaluated with the help of analysis planes according to figure 7.9. The characteristics of the components are presented in figure 8.6, from top to bottom first the impeller then the experimental data and the total head curve, below that the inducer and then the volute. The main components are displayed over the range of loading points that are investigated. It can be seen that the

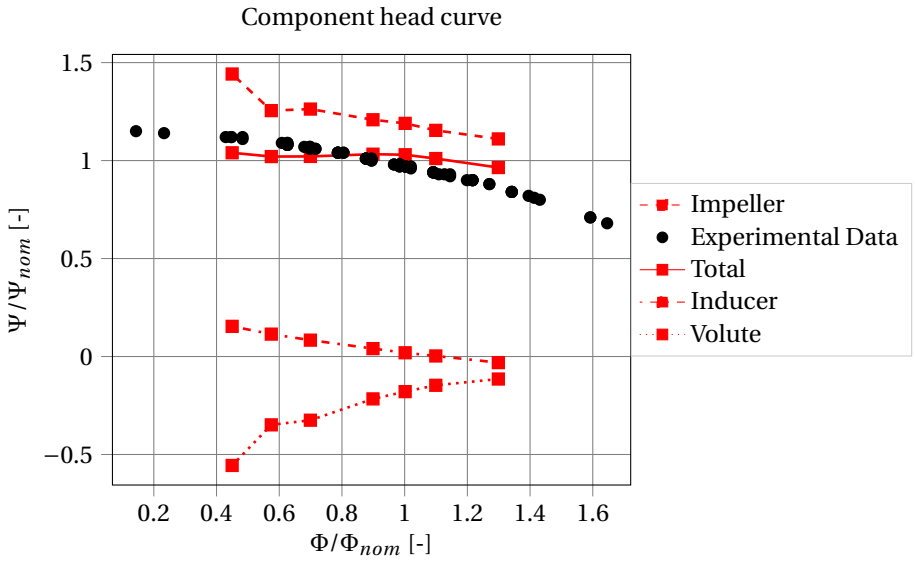

Figure 8.6: Characteristic curve of individual components

inducer plays a much smaller role to the transfer of useful work than the impeller, at high flow coefficients the inducer even reduces the total pressure in the fluid. The total pressure drop in the volute increases drastically with low flow coefficients. When comparing the volute behavior to the impeller curve it can be seen that the components are strongly coupled and that with a steep increase of head rise in the impeller at very low flow coefficients the volute generates higher losses. The impeller has the highest impact on the overall pumping system. The reason for the increase of total pressure of the overall system at $\Phi/\Phi_{nom} = 0.45$ still needs to be found.

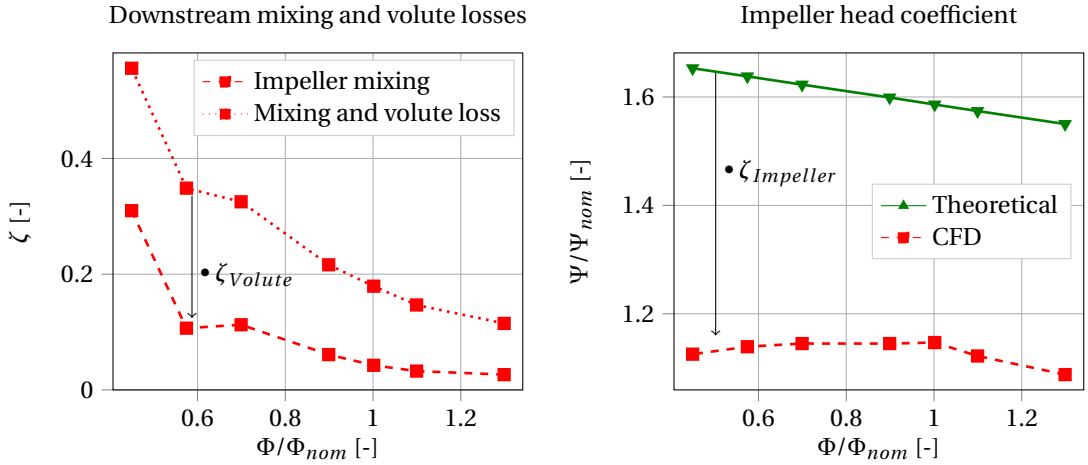

Figure 8.7: Mixing losses and impeller head curve with consideration of mixing losses

Impellers with high specific speeds have high hydraulic losses due to non-uniformities [21]. According to Gülich the downstream mixing losses of the impeller that happen in the volute have to be accounted to the impeller. Especially at low flow coefficients the non-uniformities at the impeller exit are expected to be very high which leads to increased mixing losses in the volute. The mixing losses have been determined calculating the mixed-out average at the impeller outflow on plane 5. In figure 8.7 the mixing losses are presented, along with the overall total pressure losses occurring in the volute. The overall total pressure drop between plane 5 and the volute exit at plane 6 is higher than the mixing losses, the difference of these pressure losses are volute losses. The mixing losses of plane 5 are accounted to the impeller. The steep increase in total pressure of the impeller in figure 8.6 is explained with an increase in the dynamic pressure, the velocity profile is highly non-uniform leading to a large increase in mixing losses.

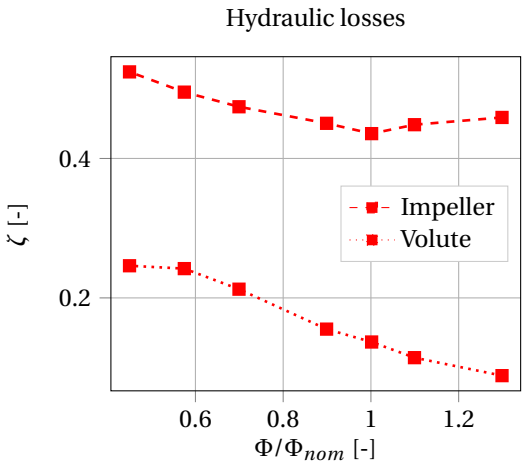

Figure 8.8: Hydraulic losses in volute and impeller

The dissection of mixing losses of the impeller and volute losses can lead to a better understanding of the origin of the saddle characteristics of the overall system. The plot on the right side in figure 8.7 shows the resulting head coefficient of the impeller when mixing losses are accounted for. The saddle-type instabilities are no longer present and the shape of the curve is flattened out. The hydraulic losses of the impeller can be determined by the difference between the theoretical head determined from blade angles assuming zero losses and the numerically determined head curve. The hydraulic losses of the volute are determined from the total pressure drop in the volute minus the mixing losses that are accounted to the impeller.

In figure 8.8 the hydraulic losses of both components are presented. It can be seen that the hydraulic losses in the impeller are minimal at nominal flow coefficient. The volute however behaves differently, a loss minimum cannot be located in the investigated loading range, at a flow coefficient of $\Phi/\Phi_{nom} = 0.45$ the loss increase stagnates and a loss maximum is reached. With this dissection of the components it is possible to explain the saddle shape of the overall characteristic curve. The losses in the volute increase steadily with decreasing mass flow but reach a maximum at around $\Phi/\Phi_{nom} = 0.55$. When comparing the volute performance to the effect of the closed interface at low flow coefficients some dependencies can be seen. The closed interface area peaks at flow coefficients below $\Phi/\Phi_{nom} = 0.72$ further decreasing the mass flow does not lead to increased blocking of the passage. Therefore the losses in the volute which are high due to the blocked passage do not increase further which leads to the kink of the characteristic curve at low flow coefficients.

8.1.2. Local flow field

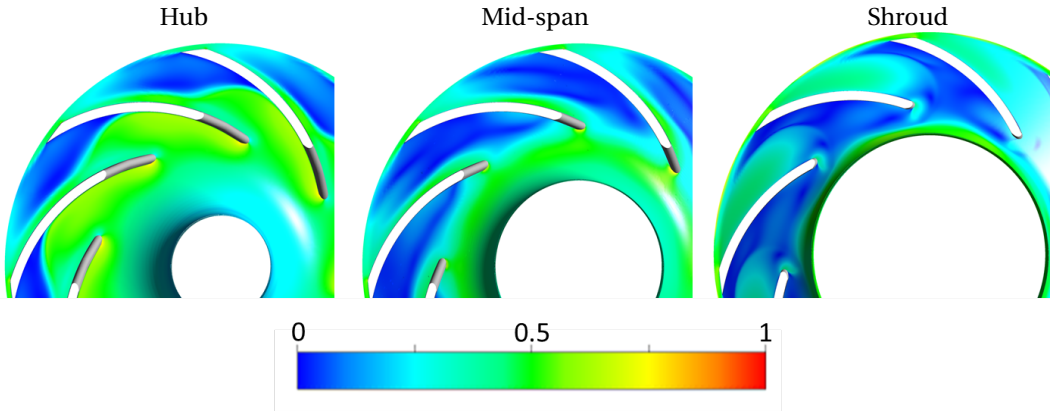

Figure 8.9: Velocity in relative frame of reference w/u_2 in design operation

The flow field in the impeller shall be further investigated. The figure 8.9 shows the velocity in relative frame for nominal operation for three different locations (5 %, 50 % at 95 % of the span; from left to right) 8.9.

It becomes easily evident that the impeller features large regions of separated flow. Separation occurs always on the suction side of the blade. At semi-span separation occurs at around 20 % of the blade coordinate (measured from the leading edge). At the hub the separation happens further downstream at approximately 70 % of the blade coordinate.

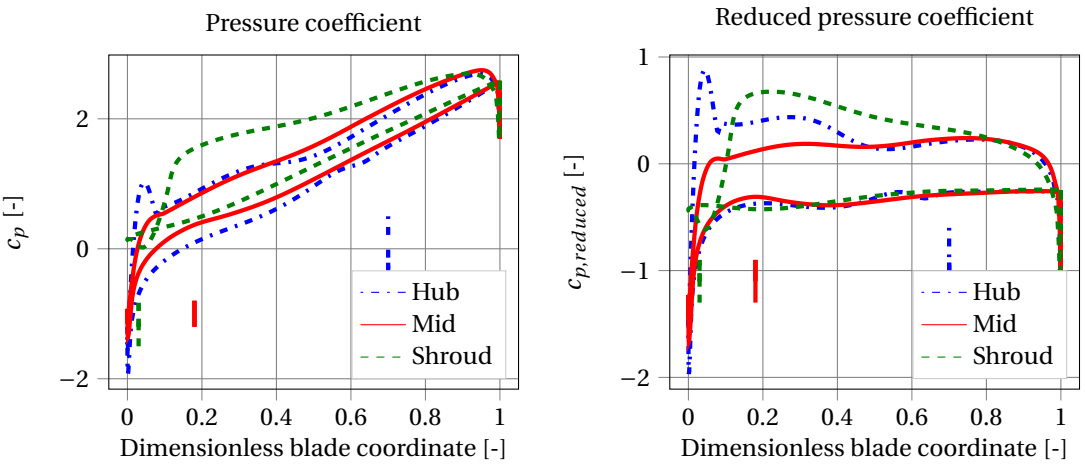

Figure 8.10: Blade loading for nominal operation

As one can already see in the meridional view in figure 8.2 at the shroud the flow is reversed and separation occurs directly at the leading edge. In the blade passage the large area of separation narrows the effective flow passage and fluid is accelerated leading to a drop in static pressure on the pressure side. This can be seen in the blade loading shown in figure 8.10, the point of separation is marked below the loading line of the suction side.

The blade loading of one of the impeller blades is shown in figure 8.10 for the three different locations at nominal operation. At hub and midspan high velocities at the leading edge lead to low static pressures. At the shroud due to the separated and low momentum flow the static pressure does not drop to such low values. The shroud features reverse loading to about 10 % of the blade length. Comparing the hub to the midspan curve it becomes evident that there is a shift in stagnation region towards the pressure side closer to the hub. This leads to high super-velocities on the suction side close to the leading edge and to low static pressures. The pressure side close to the hub shows a drop in static pressure at around 40 % of the blade coordinate. This drop is due to the narrowed cross section because of the separation on the suction side.

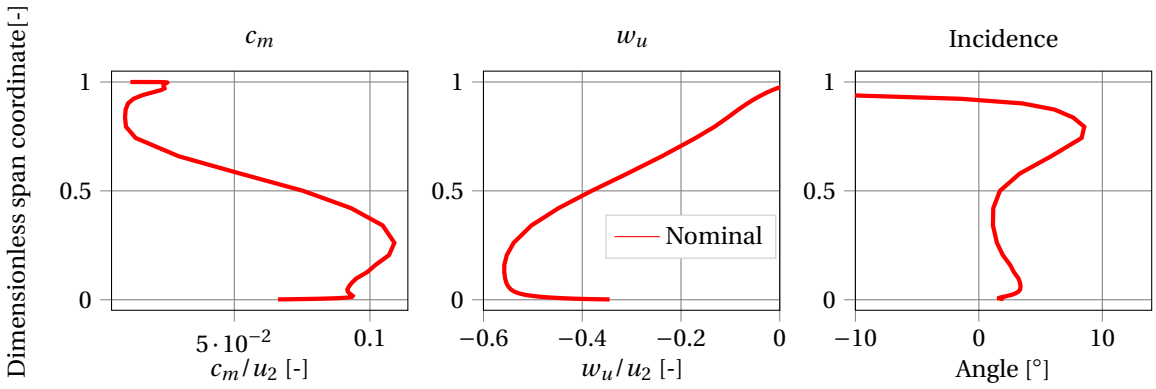

Figure 8.11: Velocity components 1% upstream of leading edge nominal operation

The change of velocity components and the incidence angle at 1 % upstream of the leading edge over the span is presented in figure 8.11. On the left the meridional velocity is plotted showing low momentum flow close to the shroud and higher velocities around the hub. The center plot shows the circumferential velocity

in relative frame presenting a similar trend. The incidence presents the behavior according to the results seen in the in the blade loading. The approaching flow angle is well aligned with the blade and a positive incidence of 1° closer to the hub the stagnation region moves further to the pressure side and incidence is increased to almost 3°, which is in agreement to the blade loading at midspan and hub. The flow field close to the shroud features reverse flow leading to large negative incidence angles at 95 % of the span. The changes are also seen in blade loading and incidence in the following 8.12 and figure 8.13.

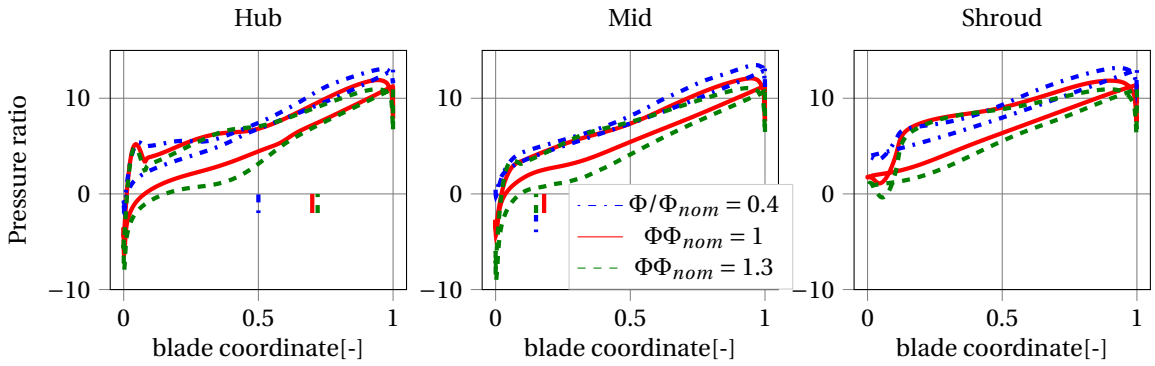

Figure 8.12: Blade loading pressure ratio for nominal, partload and overload

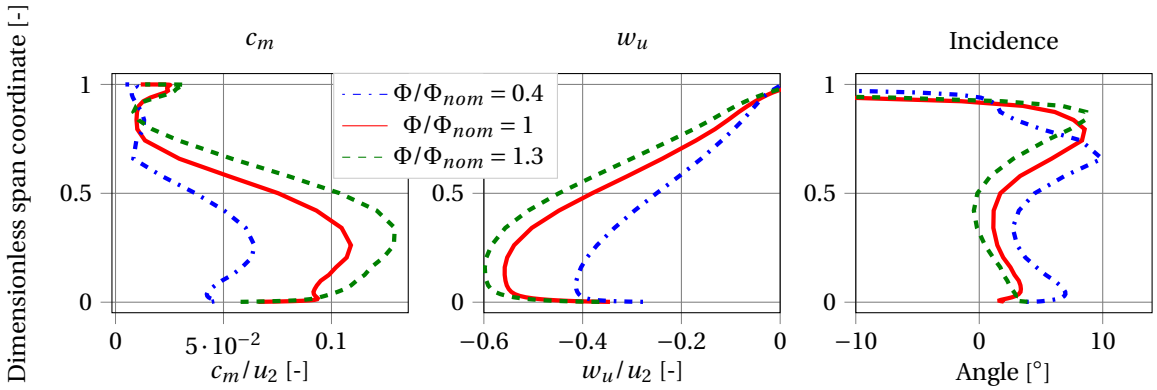

Figure 8.13: Velocity components 1% upstream for nominal, partload and overload

The behavior at partload and overload shall be investigated as well. For that the flow coefficients $\Phi/\Phi_{nom} = 0.45$ and $\Phi/\Phi_{nom} = 1.3$ are presented. The flow fields are shown in figure 8.14, the separation region remains on the suction side over the full range of investigated operating points. Especially at low coefficients the area of separated flow increases drastically on all shown span locations. This is in agreement with the increase in hydraulic losses shown in figure 8.8. At high operating conditions the flow at the hub stays attached longer than at nominal conditions.

The loading on the blades increases with increasing mass flow especially due to lower pressure on the suction sides. The separation at the hub is shifted upstream for low flow coefficients and slightly downstream for higher flow coefficients. At mid-span the nominal point features separation furthest downstream in the passage. The meridional velocity clearly shows the increase in flow speed but mainly at mid-span and lower. The incidence changes with flow coefficient. With increasing flow coefficient the incidence reduces due to an increasing meridional velocity and the stagnation region shifts slightly to the suction side.

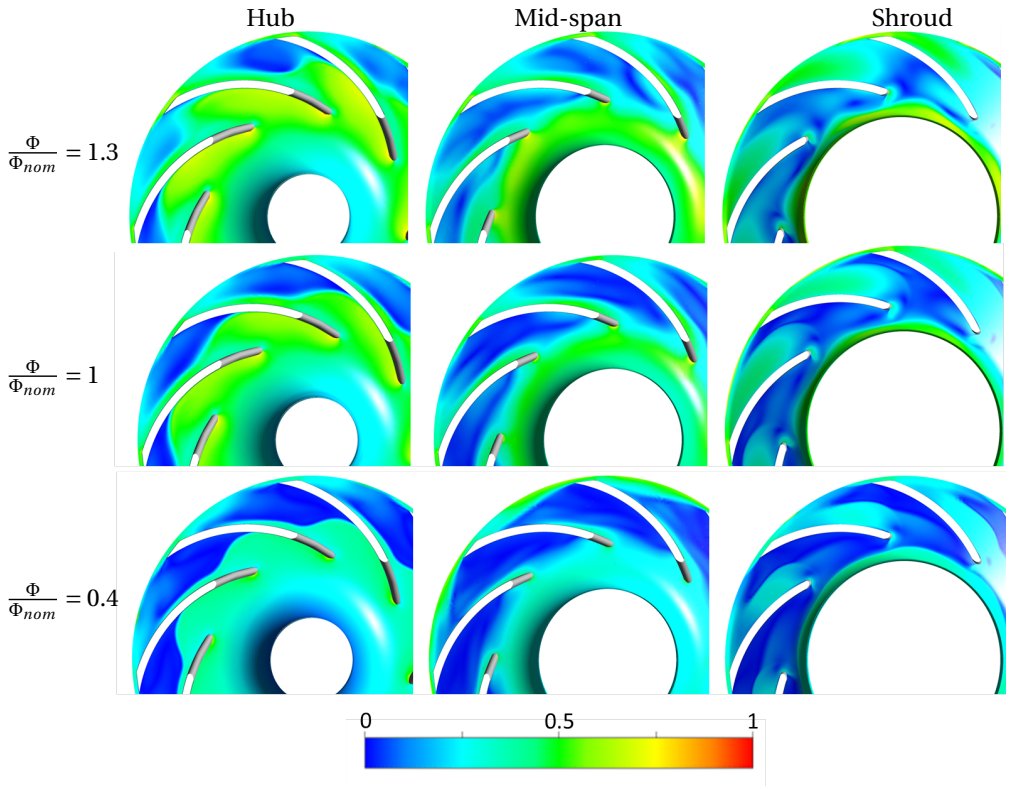

Figure 8.14: Flow field showing velocity in relative frame of reference w/u_2

8.2. Results of model with sidewall gaps

8.2.1. Hydraulic losses due to leakage injection

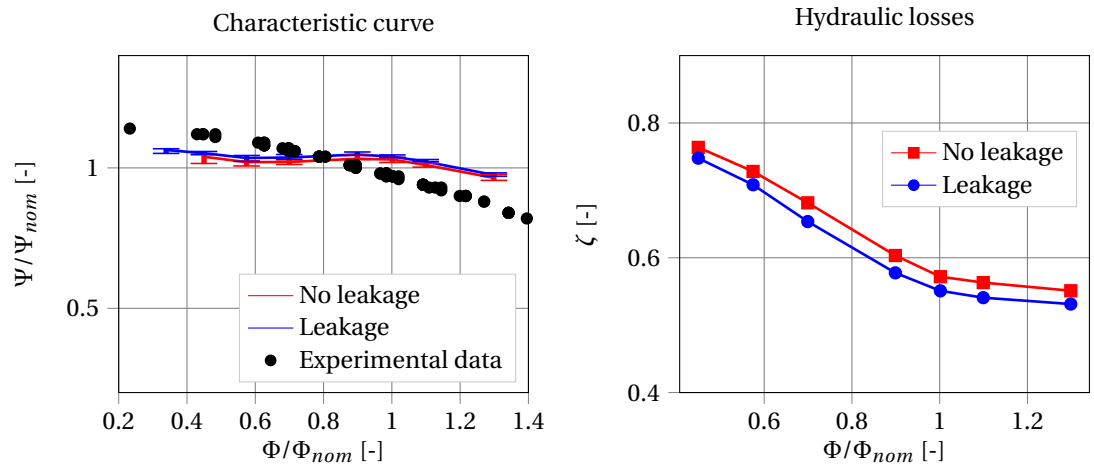

Figure 8.15: Characteristic curve and combined hydraulic losses of impeller and volute

The head curve of the model with leakage shows an interesting behavior compared to the curve without leakage. The shape and stability behavior is not changed by the leakage modeling. The head coefficient shows a constant and slight increase when leakage paths are modeled. The increase of $\Delta\Psi = 0.01$ to $\Delta\Psi = 0.015$ lies within the range of the numerical accuracy judging by the fluctuations of the global data, however the trend is stable over the full range of operating points investigated, which leads to the conclusion that the overall hydraulic losses decrease with $\Delta\zeta = 0.02$. Furthermore the Q-H curve proves that the missing modeling of the secondary flow paths is not the reason for the saddle characteristics of the performance curve seen in the results from the previous section. This behavior needs to be accounted to the volute losses connected to the blocked interface which was discussed in the previous section in figure 8.4.

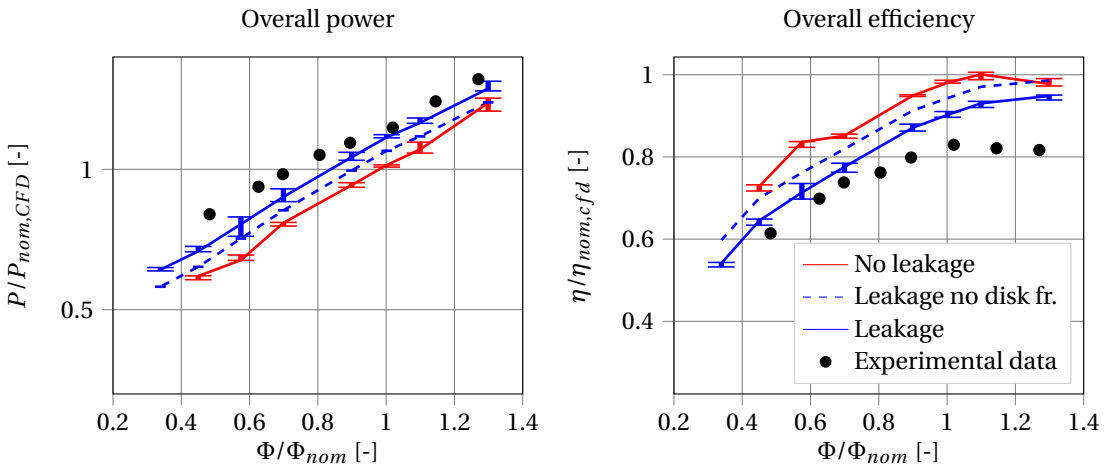

Figure 8.16: Power and efficiency overall

The overall power and efficiency of the pumping system with the modeling of leakage paths is shown in figure 8.16. The plots show the experimental results in combination with both curves for the model with secondary flow paths and without secondary flow paths. Efficiency is defined here with the numerically determined shaft power. The dashed line indicates the performance when disk friction is not taken into account. The power curve of the full model including the leakage paths shows a better agreement to the experimental results, around nominal operation the power determined from the experiments is about 3 % higher with reference to the nominal shaft power, at partload the results show higher discrepancies to the experiments, here the power from the experiments is about 13 % higher than the numerically determined shaft power. One can also see that the shaft power determined from shear stresses in the *CFD* is subject to high numerical fluctuations especially at lower flow coefficients for the simulation with side gaps. The dashed line indicates the shaft power without taking the disk friction in the side cavities into account. It can be seen that the shaft power increases for about 5 % to 6 % of the nominal power constant over the mass flow range. The difference between the power curve of the simulation without leakage paths and the dashed line is mostly the effect of increased mass flow in the impeller, however changes in the flow field due to leakage injection can change the shear stresses on the rotating surfaces and the shaft power. It can be seen that the power due to higher mass flow in the impeller increases with decreasing flow coefficient this is in agreement with the increasing total leakage mass flow at low operating points. The efficiency curves present a similar behavior. Due to the modeling of disk friction the efficiency drops 4 % to 5 % of the nominal efficiency. The increased mass flow in combination to hydraulic changes of the flow field lead to a efficiency reduction of 3 % to 0 % around nominal and overload and 7 % at partload. The overall efficiency reduction ranges from 8 % points around nominal operation to 11 % points at partload with reference to the nominal efficiency. The point of highest efficiency is shifted towards higher flow coefficients when leakage paths are included.

The component breakdown helps to understand in which part of the pump the performance changes most and how the individual components are impacted by the injection of leakage flow. It is presented in figure 8.17. The plot shows from top to bottom the impeller behavior for both models, the overall behavior, the experimental data, the inducer and then the volute. The blue lines with circles represent the simulations with leakage and the red lines with squares represent the simulations without leakage. The impact of the leakage injection on the inducer is negligible, neither shape nor quantity of the performance shows effects, this could be expected because the leakage is injected downstream of the inducer passage. The impeller and the volute show changes due to the modeling of leakage. In both cases it seems as if the curves are shifted in the direction of lower flow coefficients. The behavior can be explained since the local mass flow in the impeller and the volute is increased due to the circulation of leakage flow. The head of the impeller decreases but at the same time the losses in the volute are reduced so that the changes in the overall head curve are small.

The effects shall be further investigated by applying the mixed out condition to the impeller exit flow field. This results in the hydraulic losses of the impeller and volute with and without secondary flow paths shown in figure 8.18. The hydraulic losses in the volute reduce to about $\Delta\zeta = 0.025$ to $\Delta\zeta = 0.045$ in the impeller the

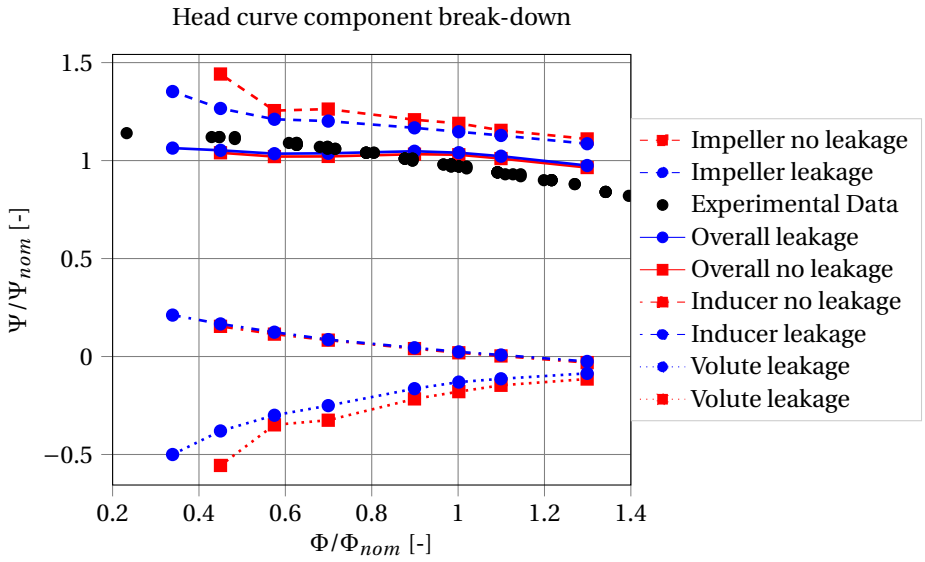

Figure 8.17: Characteristic curve of the individual components with and without leakage

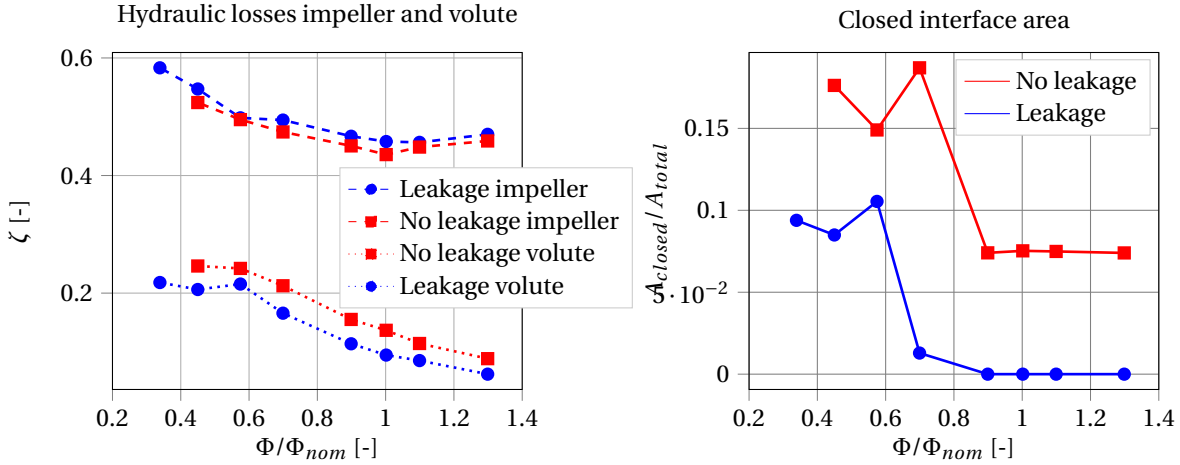

Figure 8.18: Left: Hydraulic losses in impeller and volute; Right: Closed interface area between volute and impeller

hydraulic losses increase from $\Delta\zeta = 0.01$ to $\Delta\zeta = 0.025$.

Effects of leakage injection on impeller

The effect of the leakage injection on the blade loading and the incidence angle and the overall separation region in the impeller is investigated in this section and can be linked to the change in hydraulic losses in the impeller. The first figure 8.19 shows a cut of the full geometry including arrows indicating the velocity in relative frame of reference projected tangentially on the cutting plane.

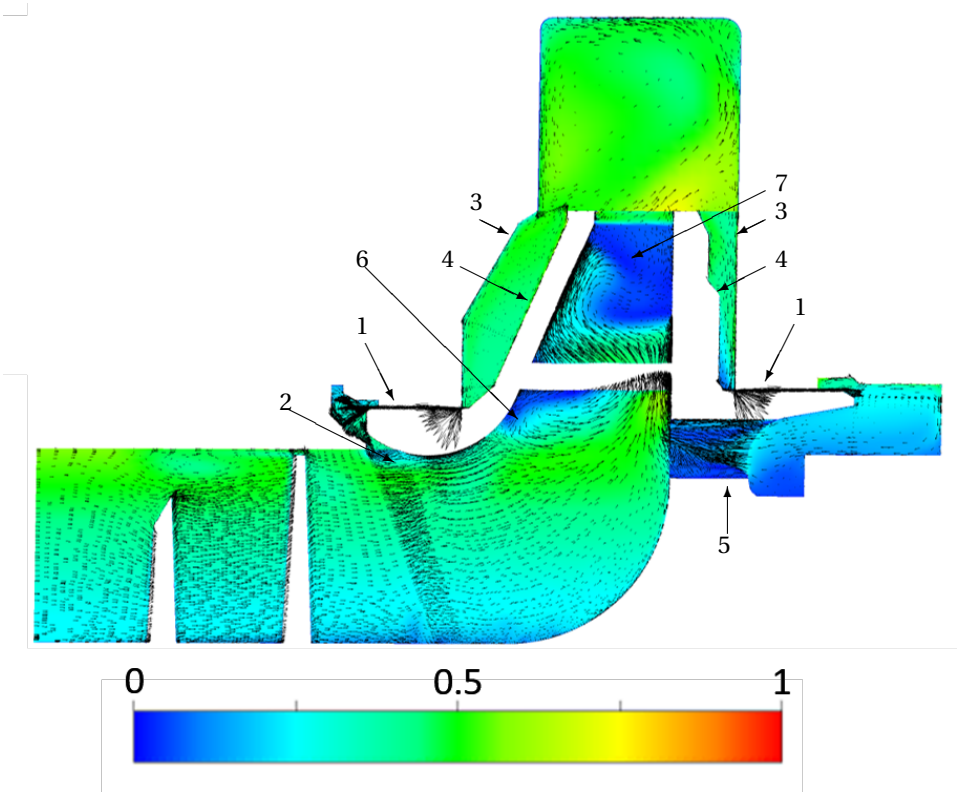

Figure 8.19: Cut along axis of rotation showing velocity in relative frame of reference at nominal operation w/u_2

Several flow phenomena are presented in the cut. At number two high momentum leakage flow enters the passage and leads to a recirculation region downstream of the injection region. The same effect occurs downstream of the balance hole injection. In number five the flow through the balance holes is visible, understandably the flow velocity in relative frame of reference is low because the flow in the holes is mainly rotating with the geometry. The arrows however indicate the high velocities in axial direction. The flow injection of the leakage through the balance holes leads to a wake downstream of the injection location in the impeller passage close to hub at the entrance of the blade passage. The flow in the sidewall gaps develops in agreement to the description in literature. In both sidewall gaps the flow close to the casing wall flows radially inwards and along the rotating wall a radial outwards flow develops due to centrifugal forces. In the center of the passage flow velocities are low in radial direction.

Table 8.1: Flow phenomena description

Marker	Description
1	Seal paths, high velocities in axial direction
2	Flow separation due to leakage injection
3	Flow inwards directed along casing wall
4	Flow outwards directed along rotor wall
5	Acceleration in hole and flow separation in passage downstream of injection (not visible on the slice)
6	Recirculation at leading edge close to shroud
7	Large separation region at suction side of blade

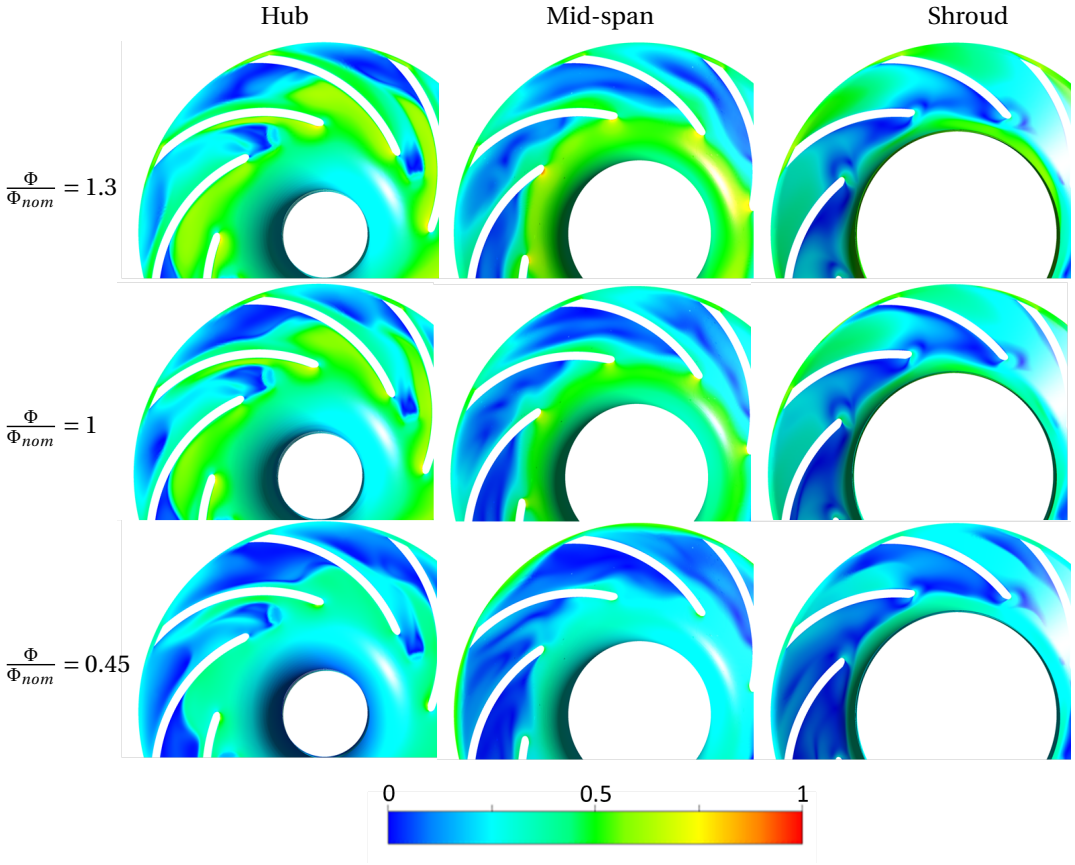

Figure 8.20: Flow field showing velocity in relative frame of reference w/u_2 with leakage injection

The low momentum wake flow due to the balance hole injection can better be seen in the velocity field close to the hub. The full velocity profile for overload nominal and partload for the model with sidewall gaps is presented in figure 8.20. The injection in every second passage is best visible on the plane close to the hub. Flow enters the passage perpendicular to the main flow direction and causes a wake of low momentum directly downstream of the balance holes. This region narrows the cross sectional area at the blade passage inlet. When leakage injection occurs on the suction side the flow is accelerated and the onset of separation is shifted downstream of the blade coordinate. When leakage injection takes place on the pressure side of the blade the wake interferes with the flow around the leading edge locally changing the loading and the incidence. The plot also shows the flow field for different operating conditions, it can be seen at the hub that the wake due to leakage injection in the passage grows with decreasing flow coefficient. The examination is plausible because the ratio of leakage flow over overall mass flow is higher at low flow coefficients. When comparing the flow field of the model without leakage injection to the flow field of the model with leakage injection at midspan and shroud, differences are at most very slight.

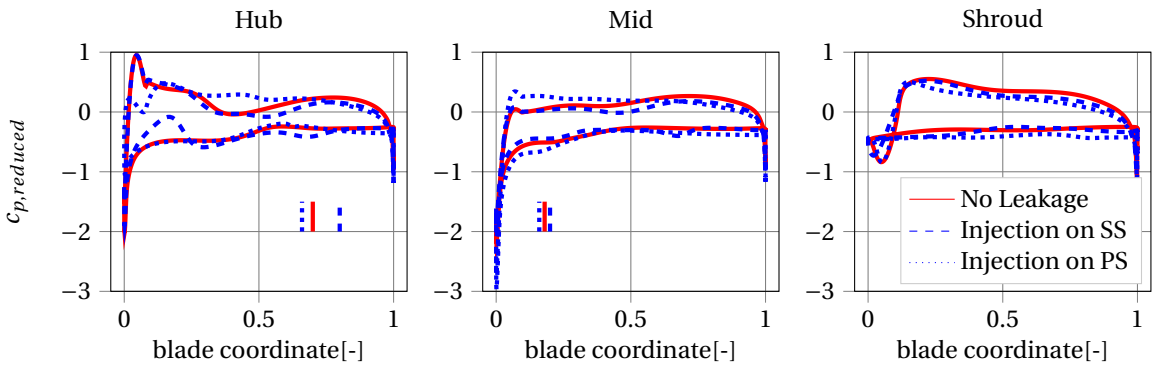

Figure 8.21: Blade Loading with and without leakage injection

Further insights regarding the change of flow in the passage can be obtained when looking at the blade loading and the incidence angles 8.21. In the blade loading plots three graphs are shown each for hub, midspan and shroud. The red line indicates the loading of the model without leakage paths, the blue dashed represents a blade for which leakage injection through the balance hole is located on the suction side and the blue dotted shows a blade with leakage injection on the pressure side. The graph at the hub shows the largest differences between all the curves, this can be expected since the injection takes place through holes in the hub on the same streamwise location as the leading edge. One can see that the side on which the leakage occurs shows the largest differences to the loading of a blade without leakage injection. When leakage occurs on the suction side at the hub for the first 25 % of the blade (upstream of the injection location) the flow decelerates more than normal so static pressure increases to higher values than normal. When approaching the injection region the pressure drops drastically. The velocity is increased due to the narrowed effective cross section of the blade passage. As indicated the flow on the suction side experiences an aftward shift of flow separation. The overall loading at the hub is decreased around the first 25 % of the blade coordinate.

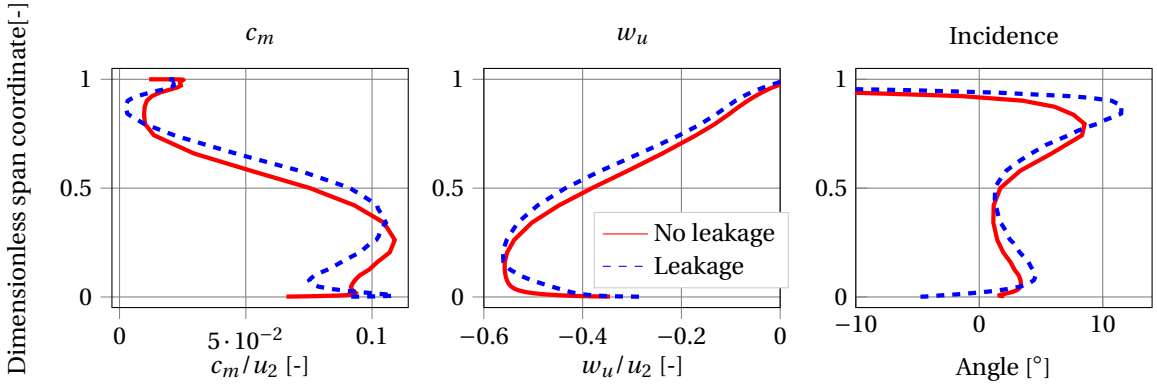

Figure 8.22: Velocity components and incidence angle at 1% upstream of the leading edge

When leakage occurs on the pressure side the wake interferes with the leading edge. The local incidence at the hub reduces and stagnation region moves in direction of the suction side. The pressure peak reduces and loading is reduced. The separation happens around 5 % upstream of the no leakage separation point. Because of the aftward shift of the separation region of the proceeding blade the velocities increase further downstream which leads to an increased loading around 50 % of the blade coordinate.
There are only minor changes to the shape of the blade loading in midspan, when leakage occurs on the pressure side the loading increases on both pressure and suction side, when leakage occurs on the suction side the loading reduces slightly. Changes at the shroud are negligible. Due to the large wake region around the hub of the impeller and reduced loading because of leakage injection at the hub the increase in hydraulic losses in the impeller becomes understandable. The velocity and incidence plots presented in figure 8.22 present similar results to the plots without leakage injection with increased mass flow.

Volute flow

The component analysis of the pump with and without leakage indicates that the losses in the volute are reduced when leakage is implemented. The loss curve of the volute 8.18 also shows that minimal losses are not yet reached in the investigated flow regime, a minimum can be expected at very high flow coefficients. The impeller exit flow features higher mass flow due to the reinjection of leakage at the impeller inlet. Therefore the volute is subjected to increased mass flow locally, the reduction of hydraulic losses is understandable due to a shift in mass flow. Figure 8.23 however indicates that the volute performance shift cannot only be explained with the shift in mass flow. Especially at low flow coefficients the volute losses are higher without leakage paths even when the shift in local mass flow is considered. A small effect can be found due to increased friction losses in the volute without leakage paths. In this model the faces that are connected to the sidewall gaps and the impeller tip are modeled as walls with the no-slip condition, however when looking at shear stresses and the accounted friction losses the overall increase in performance when the sidewall gaps are included cannot be explained with that effect only. The area of the closed interface reduces over the full flow regime when the leakage paths are added to the model 8.18. As explained before, the closed interface is

linked to the losses in the volute. Further investigations of the volute flow field are necessary to understand the effects of the volute tongue better. The flow entering the volute features higher velocities in stationary frame at the hub side of the volute.

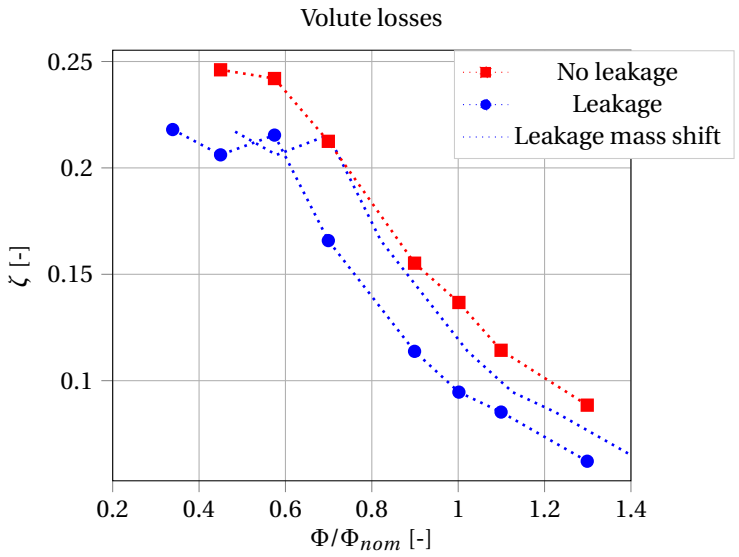

Figure 8.23: Volute losses both models and mass shift

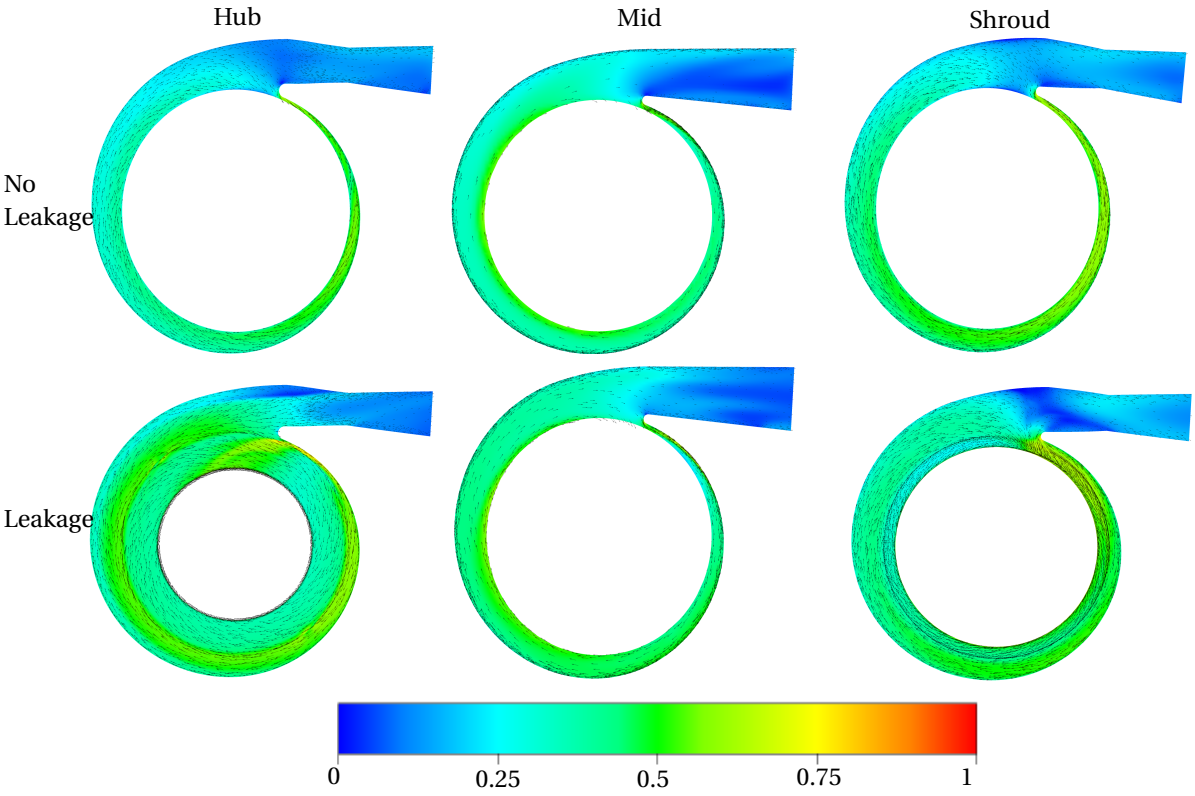

Figure 8.24: Velocity in stationary frame c/u_2 at hub, mid and shroud in volute with and without sidewall gaps $\Phi/\Phi_{nom} = 0.45$

Secondary flows are built up according to figure 8.25 leading to higher velocities and radial outward velocities at the hub and lower velocities which are directed radially inwards at the shroud. This effect can be seen throughout the investigated flow regime, however the secondary effects due to higher non-uniformities and lower meridional velocities increase their impact on incidence and flow field close to the tongue. The

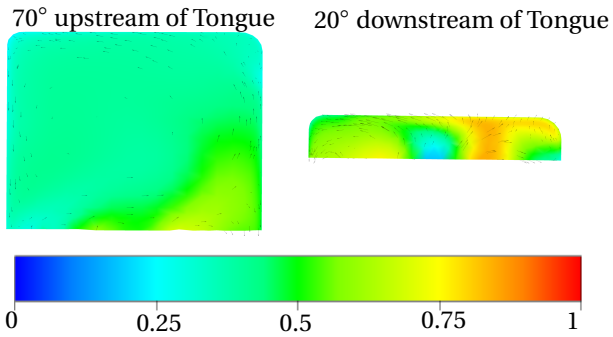

Figure 8.25: Spanwise velocity profile 70° degrees upstream and 20° downstream of volute tongue at $\Phi/\Phi_{nom} = 0.45$

incidence at the tongue varies across the span according to these secondary flows. High incidence values especially at the shroud region are found in both models with and without leakage. High incidence angles mean a shift in stagnation region to the volute outlet and lead to high velocities in the narrow cross section. It is possible to see the shift in stagnation region in both models. In both cases the flow around the tongue at the shroud features some reverse flow from the volute outlet back into the volute passage. This effect is larger in the model with leakage. When looking at the flow field at midspan and hub the comparison between the models with and without leakage can give further knowledge on why the pressure recovery is better in the volute when leakage paths are modeled as well. Especially at the hub the incidence at the volute tongue is lower and stagnation region is located very close to the leading edge. The overall level of velocities in hub and midspan is higher as compared to the model without leakage and features less separated flow. The improvement in volute performance is due to increased secondary effects caused by the leakage paths. Some hypothesis on why the implementation of the leakage flow causes these stronger secondary effects are possible. The injection through the balance holes can cause a drastic change in the impeller outflow leading to more non-uniform impeller outflow and larger secondary flows in the volute passage.

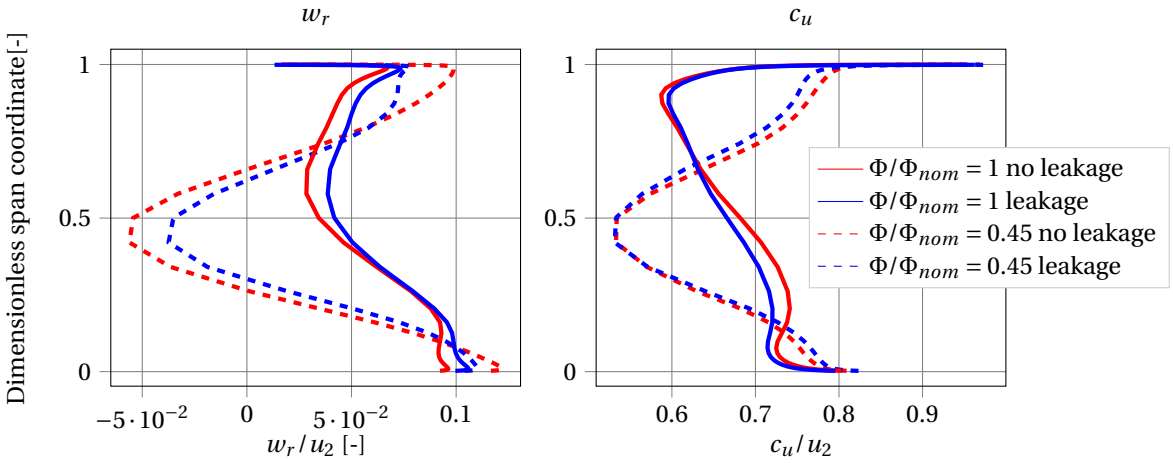

Figure 8.26: Impeller outflow velocity distribution in radial and circumferential direction for $\Phi/\Phi_{nom} = 1$ and $\Phi/\Phi_{nom} = 0.45$ with and without leakage

The impeller outflow velocity profile (plane 5) is presented in figure 8.26. It shows the radial and circumferential components for nominal operation and partload operation for both the models with and without leakage. One can see that the outflow profile becomes very non-uniform at low flow coefficients featuring reverse flow in the center of the passage. This is in agreement to the increased mixing losses at partload downstream of the impeller. When comparing the model with and without leakage big changes in velocity profile cannot be identified, if any, at partload the profile is slightly more uniform. The balance injection does not cause a strong divergence in outlet flow profile from the baseline case without leakage. The increased secondary effects in the volute because of leakage modeling could also be explained with the additional spanwise asymmetry which is introduced volute geometry because of the secondary flow paths. The front and back leakage paths are not symmetric so that the volute geometry becomes asymmetric in spanwise direc-

tion, which allows for larger secondary flow effects perpendicular to the main flow direction.

The plots of the leakage model in figure 8.24 show the velocity field in the sidewall gap entrances as well. Especially at the shroud the large amount of radial inflow in the gap becomes visible. The sidewall gaps feature a frozen rotor interface to the volute which allows for flow in both directions. The inward flow enters the side gaps with high radial velocities a similar effect can be seen on the hub but to a lesser extend. Flow in the front side gap upstream of the of the tongue is retarded due to the injection in radial direction at the tongue. This increases the disk friction and axial thrust at low flow coefficients in the front cavity which will be presented in the following.

Mixing losses due to leakage injection

As mentioned in the literature study the injection of leakage flow to the main passage creates a less uniform velocity profile. The mixing losses from leakage injection have to be quantified. The velocity components at plane 2 after the front leakage injection are shown. One can see the increase of meridional velocity at 85 % of the span, furthermore the circumferential velocity in relative frame of reference is reduced which reduces the flow angle close to the shroud. In the meridional plot in figure 8.28 it can be seen that similar effects occur when leakage is injected to the passage through the balance holes. In both locations were leakage is injected the circumferential velocity in stationary frame increases locally which leads to non-uniformities in the flow. The inlet to outlet plots in figure 8.29 show that the local total pressure is slightly increased due to the leakage injection (Pressure ratio 1.07 to 1.12).

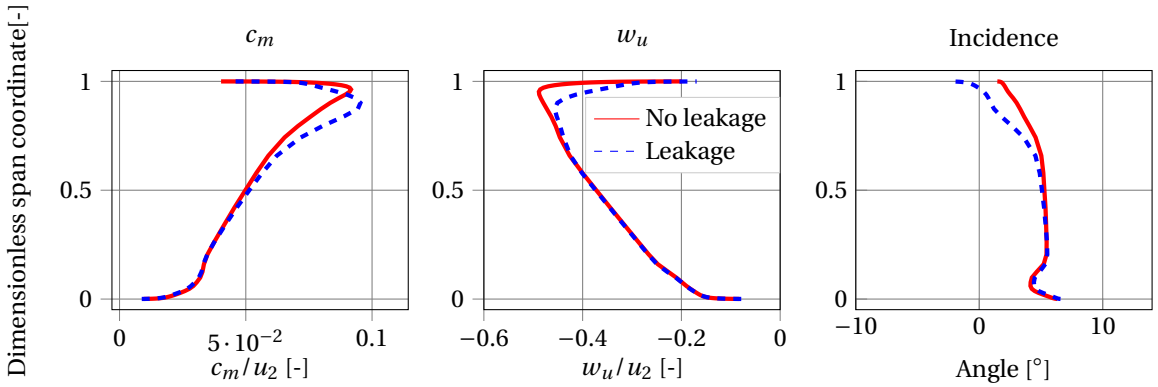

Figure 8.27: Velocity components and incidence at plane 2 nominal operation

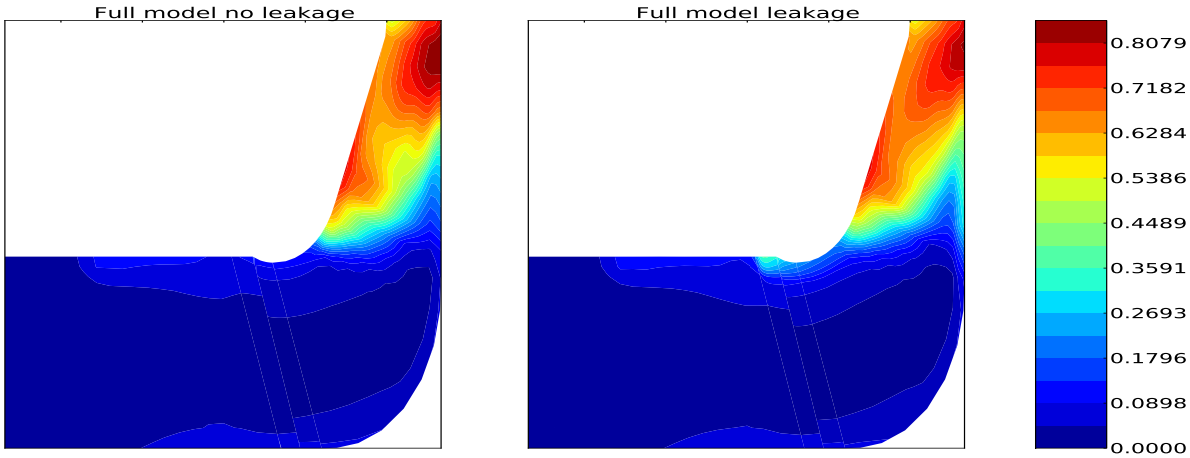

Figure 8.28: Circumferential velocity in stationary frame c_u/u_2 at nominal operation

When applying the mixed out average method on the flow downstream of the injection region the increased mixing losses due to injection can be evaluated. The mixing losses of plane 2 are presented in figure 8.30. The difference between the simulations with and without leakage determines the amount of mixing losses due to leakage injection. It can be seen that in both cases the mixing losses downstream of the inducer increase at flow coefficients lower than $\Phi = 0.73$, this is due to increased recirculation and higher disturbances in the inducer exit flow. The mixing losses of the numerical results when leakage is injected are always higher than the losses without injection. The mixing losses due to injection increase with lower overall mass flow. This is also expected since the effect of the leakage flow which is comparatively constant over the operating regime is aggravated when the overall mass flow is decreased. The mixing losses for the front leakage increase from $\zeta_{mixing} = 0.004$ to $\zeta_{mixing} = 0.007$. The total pressure is increased on plane 2 due to leakage the downstream mixing losses need to be accounted which leads to an overall leakage mixing effect and a very slight increase in total pressure of $\Delta\Psi = 0.0015$. This value is in very good agreement with the mixing loss model

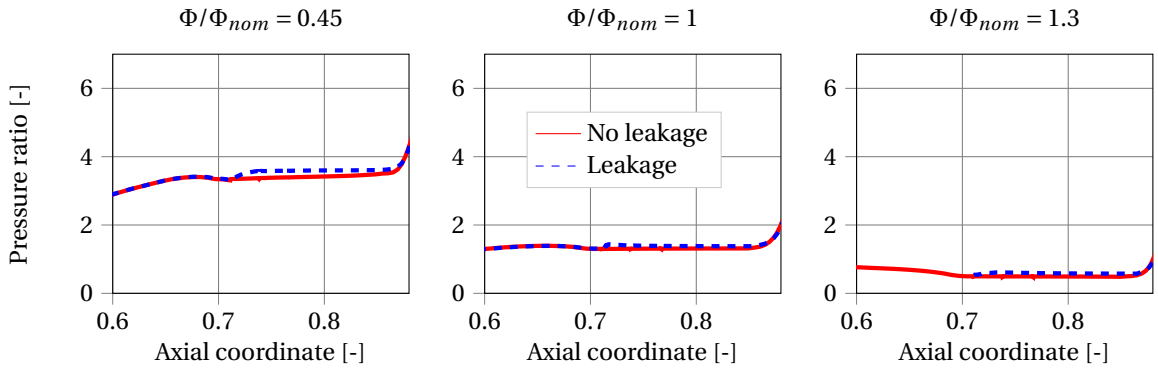

Figure 8.29: Total pressure ratio at front leakage injection location

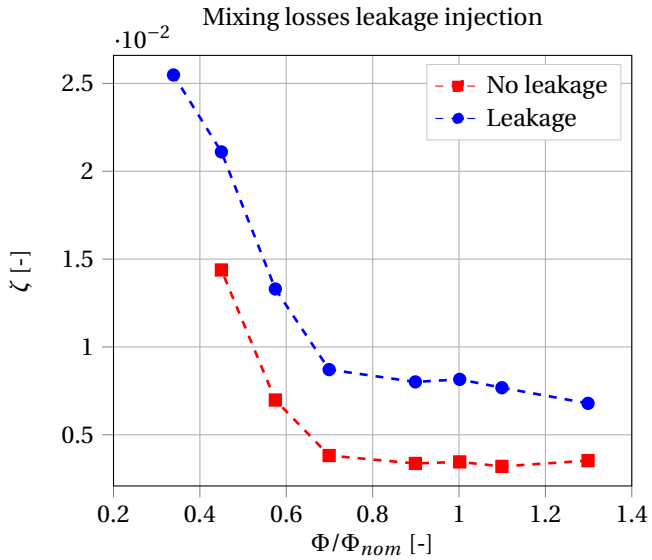

Figure 8.30: Mixing losses at plane 2

presented in the literature study by Shapiro (1953) [19].

$$T\dot{S} = -(m_m + m_c)\frac{\Delta p_{tot}}{\rho} = m_c(v_m^2 - v_m v_c \cos\alpha) \tag{8.1}$$

Using the injection angle and nominal flow conditions the mixing model predicts an increase head coefficient $\Delta\Psi = 0.0017$. The mixed out averaged method as well as other averaging methods are creating large errors when applied to flow fields with a high amount of recirculation. An equivalent analysis of the mixing losses due the balance hole injection is therefore difficult to perform, because both the mass flow averaged total pressure in the middle of blade passage and area averaged velocities for the mixing analysis are giving unreasonable results.

However, compared to the lost power due to disk friction and lost work due to leakage extraction the mixing losses downstream of the injection location play a minor role in the overall loss balance.

8.2.2. Secondary losses and thrust

The secondary flow paths have been added to the numerical model in order to be able to investigate the different loss mechanisms and the axial thrust on full scale level. The sidewall gap inlets are connected to the volute and the outlets to the impeller passage and impeller inlet respectively. The first figure 8.31 shows the leakage mass flow with respect to the nominal mass flow rate and the volumetric efficiency over the investigated operation range. Around nominal design the changes in overall leakage mass flow are minor 12.6% to 12.1% of the nominal mass flow. At flow coefficients below $\Phi/\Phi_{nom} = 0.7$ the behavior changes and leakage increases through both leakage paths, the change happens more drastically in the front path which leads to

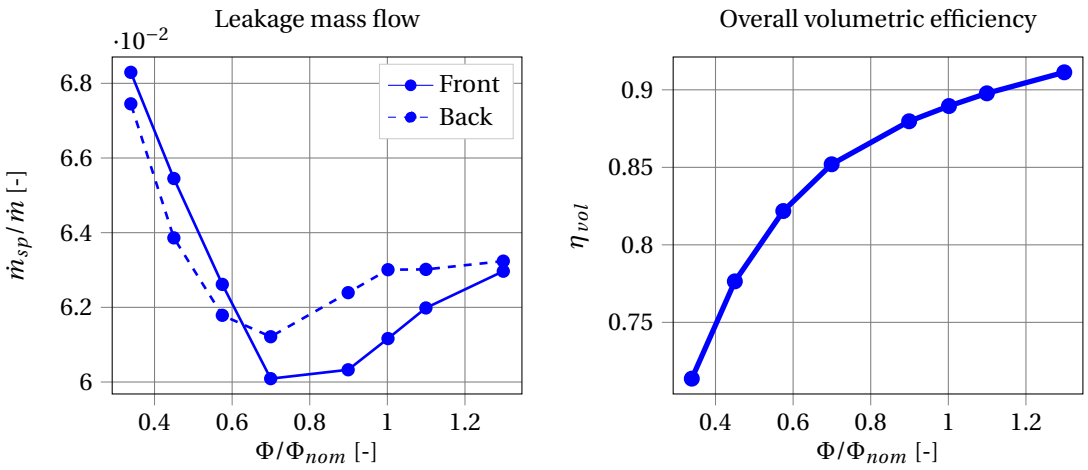

Figure 8.31: Leakage mass flow and volumetric efficiency

higher mass flow through the front seal as compared to the back seal. Around design operation the leakage through the balance holes is 3 % higher than through the front seal. The volumetric efficiency shows a steady increase with higher flow coefficients since compared to the change of overall mass flow the leakage mass flow remains roughly constant. At overload the volumetric efficiency reaches values over $\eta = 90$ % and at partload the efficiency drop to almost $\eta = 70$ %. The increase in leakage mass flow at low operating conditions needs to be further investigated in the course of this section.

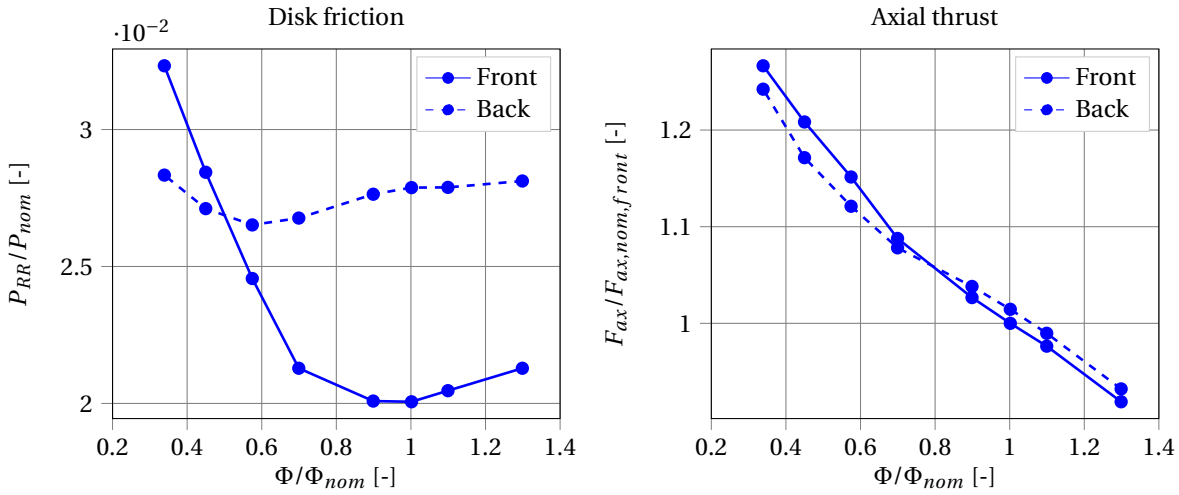

Figure 8.32: Axial thrust and disk friction

The axial thrust in the sidewall gaps and the disk friction of the sidewall gaps are presented in figure 8.32. A similar trend as with the leakage mass flow can be seen here. The disk friction increases in both leakage paths at low flow coefficients, however the trend is larger and at higher flow coefficients for the front leakage path, which leads to an overall increase of disk friction in both leakage paths from 5 % around nominal conditions to 6 % at low flow coefficients (both values normalized with the overall shaft power at nominal loading). Disk friction, leakage mass flow and axial thrust feature a shift in quantity comparing front and back leakage. The axial thrust generated in the side cavities features a steady increase with decreasing mass flow due to the higher static pressure level. The resulting force shifts the direction pointing towards the inlet and then opposite when flow coefficient is reduced. The thrust generated in both leakage paths is balanced well (resulting force ranges from 0 % to 2 % of the force of the front side at nominal operation).

In the following the flow properties in the side gaps shall be investigated to identify the origin of the steep increase of friction and thrust especially on the front side. The pressure distribution and the distribution of

circumferential velocity can lead to a better understanding of the flow mechanisms in the side cavities. Further investigations will follow in chapter 11, where the differences between full-annulus model and impeller model are presented.

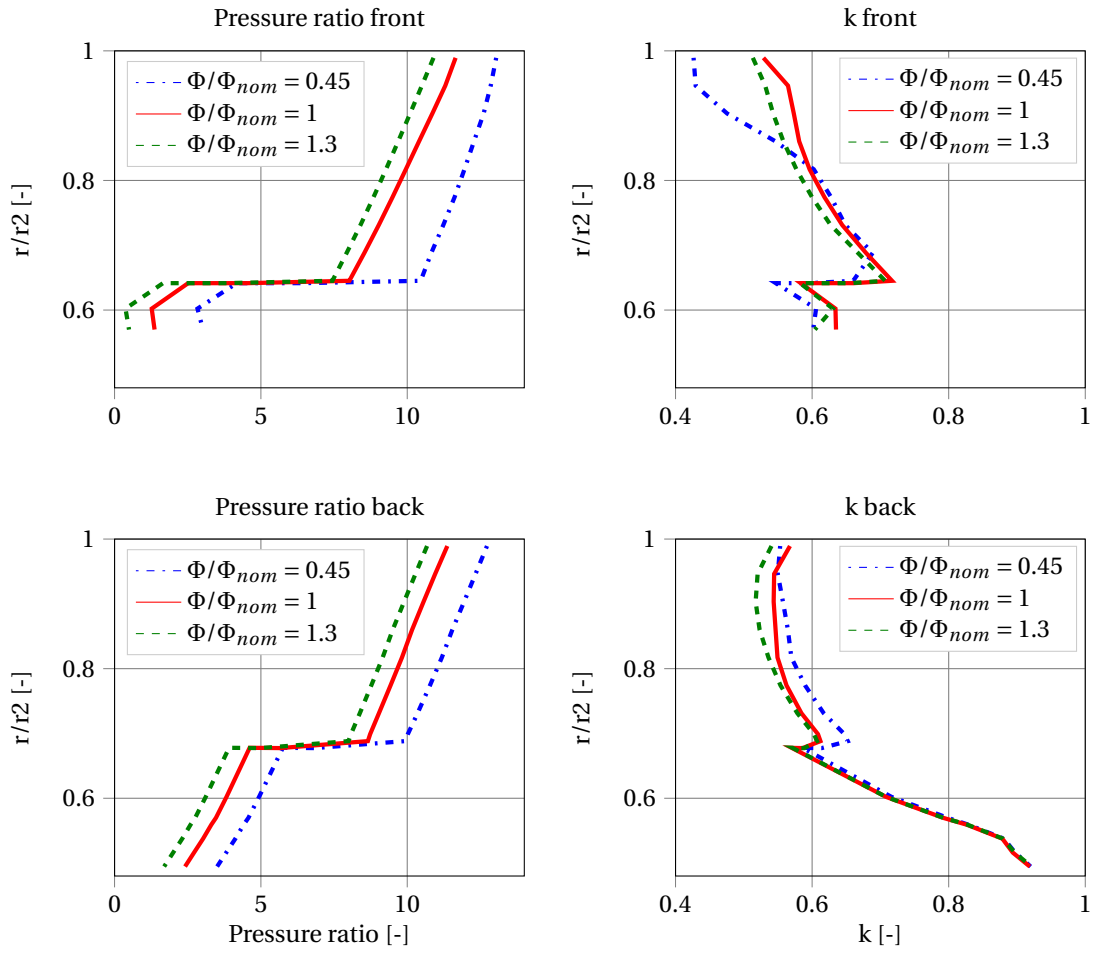

Figure 8.33: Pressure and rotation factor distribution for front and back leakage path

Multiple investigations can be made looking at the plots presented in figure 8.33. On the left side the static pressure distribution is displayed for the front and for the back leakage path for the three different flow coefficients. It shows how the pressure ratio changes with the change in dimensionless radius. The pressure in the cavity drops almost linearly for the two higher flow coefficients. When the radius of the seal is reached and the flow is deflected in the axial direction the pressure drops drastically. When exiting the seal the pressure gets further reduced to reach static pressure of the exit. The pressure distribution for the low flow coefficient features a slightly different shape. The pressure at the inlet does not drop with the same gradient as the other two distribution lines. The pressure drops less in the cavity in the simulations with low flow coefficients. This results in an increase of axial force in the front at that operating condition. The leakage mass flow increases due to a larger static pressure difference across the seal. The investigations can directly be linked to the curves of the leakage mass flow and the axial thrust, which show the steep increase of mass flow and thrust in the front leakage. The back leakage shows a slightly similar behavior but with less pronounced effects, this is also mirrored in the results previously presented. The right side presents the development of the rotation factor k. It can be seen that the rotation factor increases with decreasing radius. In the seal the rotation is reduced and downstream of the seal rotation factor increases again. The most interesting phenomenon can be observed when comparing the low flow coefficient distribution to the higher distributions. Especially at the front side gap inlet the rotation factor is much lower which means that the circumferential velocities in the gap at the inlet are reduced. The only difference to the other conditions can come from interaction with the volute flow. It seems that low momentum fluid enters the side gaps and leads to a reduction of the rotation factor at low operating conditions. The increase of the disk friction especially on the front side can easily be explained

with the lower circumferential velocities in the cavity. Low rotational speed of the core flow leads to larger velocity gradients in the boundary layer on the rotor wall and therefore increased shear stresses. The low flow velocities in the side gap are presented in the previous section in figure 8.24 upstream of the tongue. The large injection of fluid in radial direction at the volute tongue into the front cavity blocks the upstream flow in the cavity and reduces velocities.

8.3. Conclusions

The different loss mechanisms and effects on axial thrust have been analyzed. In figure 8.34 the impeller efficiency is presented for both the simulations with and without leakage paths it is defined with the theoretical power evaluated from Euler's turbine equation applied on blade angles. The impeller efficiency allows for a clear dissection of the loss mechanisms. The hydraulic efficiencies are presented on the top. It can be seen that the hydraulic efficiencies are very close for both simulations, but that the leakage injection increases hydraulic losses slightly. The hydraulic efficiency is defined according to table 7.7 takes into account the local mass flow in the impeller passage which is higher due to leakage injection, the disk friction in the sidewall gaps is not added to the power balance. The difference between the two hydraulic efficiencies must therefore be due to the injection of leakage flow and the increased hydraulic losses. Taking disk friction into account lowers the efficiency further. The by far largest impact however is due to loss of useful work due to the extraction of leakage flow. The effective impeller efficiency is shown, here the impeller mass flow is reduced by the leakage mass flow.

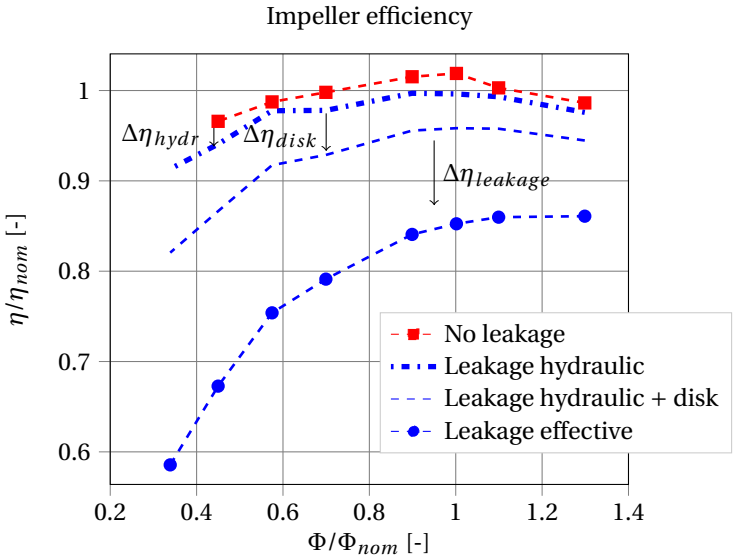

Figure 8.34: Efficiency drop due to leakage

In the following chart 8.2 the effects are summarized and quantified. The efficiency drop is quantified relative to the efficiency of the baseline simulations without leakage at flow coefficients $\Phi/\Phi_{nom} = 1.3$ and $\Phi/\Phi_{nom} = 0.45$.

Table 8.2: Effects on impeller efficiency full model

Mechanism	Flow coefficient high	low
Hydraulic losses due to leakage injection	1.5 %	2.9 %
Disk friction losses	2.8 %	7.3 %
Leakage losses through seals	8.5 %	20.2 %
overall	12.8 %	30.4 %
Axial Thrust	-2 %	2.5 %

9 Impeller-Only Model

A numerical model shall be implemented to capture the relevant effects of leakage and sidewall gaps on the performance and thrust of the pump. The model should offer higher flexibility and lower modeling and calculating effort. The effects shall be captured with higher accuracy than by analytical models in literature.

9.1. Hydraulic losses due to leakage injection

In this section the results of the simulations of the impeller model will be presented. The model with leakage is compared to the model without leakage and the losses are quantified.

The figure below 9.1 shows the characteristic behavior of the impeller models with and without leakage including the experimental data. There are several observations possible from the figures. The error bars indicate the fluctuations of the global data when residuals are not decreasing anymore. It can be seen that the model with leakage shows the highest fluctuations and uncertainties over the full range of flow coefficients. Investigations of these effects showed highest residuals around the mixing plane from impeller to diffuser and also at balance hole injection region. However certain trends and conclusions can still be observed. Since the geometry misses the volute and the losses accounted to the volute the head curve resembles more the impeller head curve. The saddle shape of the head curve that can be observed in the full scale model due to the volute losses is not present when the impeller is investigated. Comparisons between the models should therefore be performed on the impeller component only. The shaft power due to leakage increases approximately 10 % of the nominal shaft power. Still the power from the torque analysis from numerical results under predicts the shaft power compared to the power determined from experimental data. The efficiency curves show highest efficiency at the highest flow coefficient. Again the efficiency is defined with the shaft power determined from shear stresses on the rotating surfaces from numerical results.

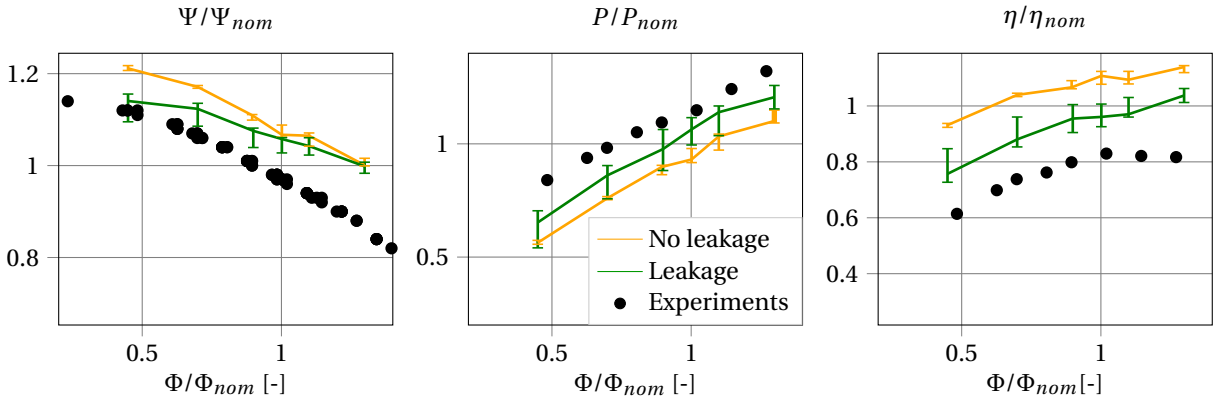

Figure 9.1: Characteristic curve of head, power and efficiency

The hydraulic losses with and without leakage shall be compared by applying the mixed-out average

method to account for the downstream losses of the impeller flow. Although all the losses in the friction-less diffuser geometry count for impeller losses, the same method as in the full scale geometry is applied to avoid misleading interpretations, the mixed-out approach delivers values which are close to the total pressure drop in the diffuser anyways. The hydraulic losses in the impeller with and without leakage are presented in the following figure 9.2. The head curve already indicates larger differences between the two impeller models at low flow coefficients. The same effect can be seen in the hydraulic losses. It can be observed that also in the impeller-only model the losses with the leakage injection are higher $\Delta\zeta = 0.01$ around nominal operation and $\Delta\zeta = 0.06$ at partload operation. The shape of the loss curve indicates a loss bucket around nominal and slight partload operation.

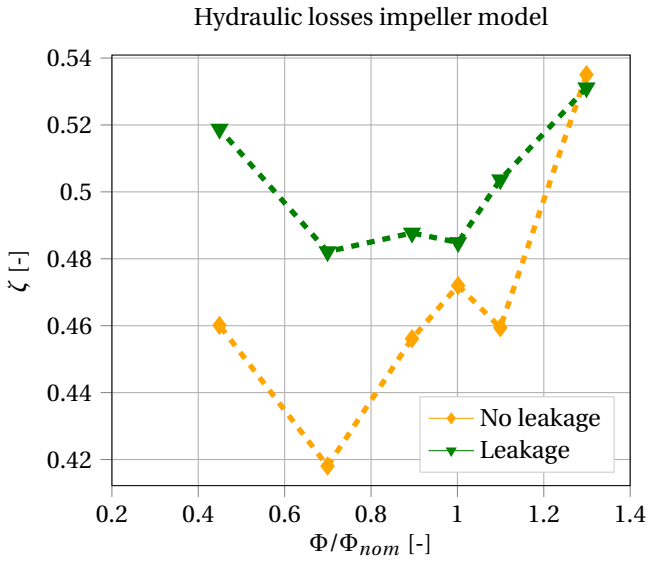

Figure 9.2: Hydraulic losses of impeller model with and without leakage

The mixing losses at plane 2 are shown in figure 9.3. The difference between the two models represents the increased downstream mixing losses due to the non uniform velocity profile. Also in this case the total pressure at plane 2 is increased due to the injection of high momentum flow and downstream mixing losses are accounted for so that the overall effect of the mixing losses due to leakage injection at the front leakage is negligible compared to the other effects.

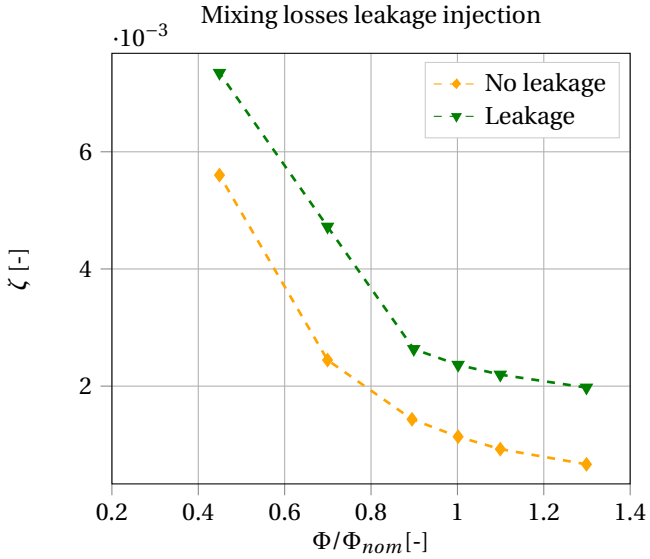

Figure 9.3: Mixing losses after leakage injection

9.2. Secondary losses and thrust

The behavior in the sidewall gaps is analyzed. The disk friction and the axial thrust generated in the sidewall gaps are presented below in figure 9.4. The disk friction curves show a rather constant but decreasing behavior with decreasing mass flow.

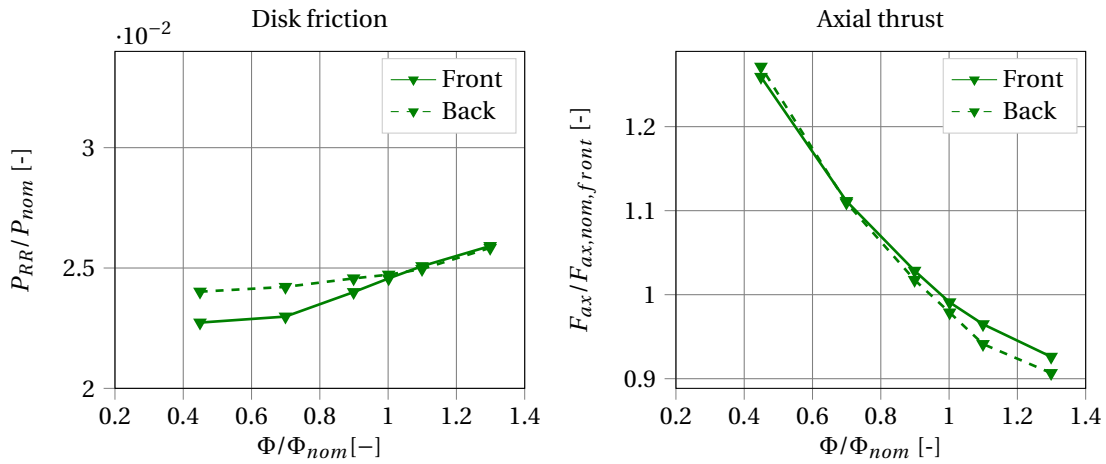

Figure 9.4: Disk friction and axial thrust of impeller model

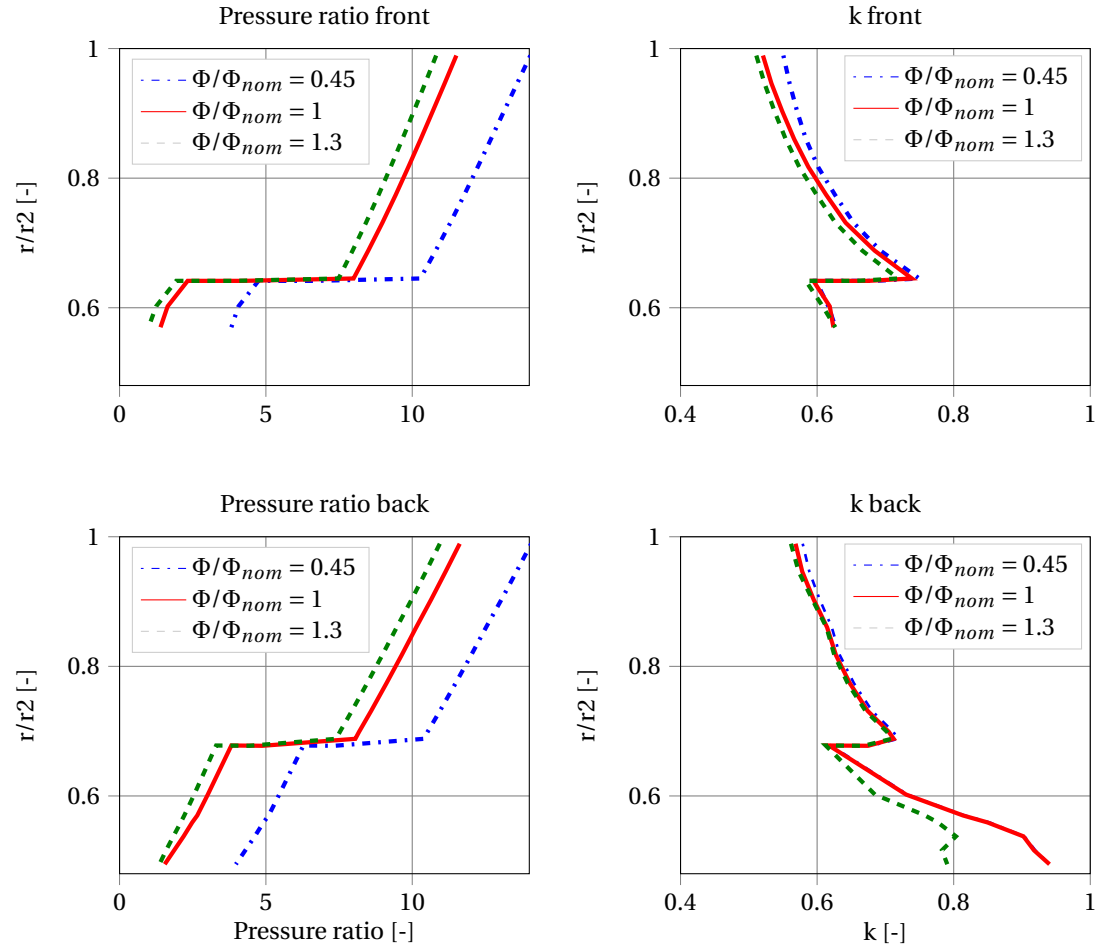

Figure 9.5: Pressure and rotation factor distribution for nominal, overload and partload operation

The disk friction on the front side decreases faster towards lower flow coefficients than the friction on

the hub rotor at the back. The expectations are that this can be explained with local changes of the velocity profile at the side gap entrance. Over the whole investigated operating regime thrust is balanced well. From overload $\Delta F = 3$ % to partload $\Delta F = -1$ % a shift in thrust direction from the sidewall gaps is observed. Also the impeller model features the increase in overall thrust due to the increase in pressure level. There are multiple investigations possible when linking the plots for pressure distributions and rotation factor distribution to the plots of axial thrust and disk friction. Regarding the back leakage the disk friction remains almost constant over the operating regime. The rotation factor for the back seal upstream of the cavity shows a similar behavior. At partload, nominal or overload the change in circumferential velocity is only small in the sidewall gap. Comparing that to the front leakage it is possible to see that the rotation factor increases about 10 % from nominal to partload compared to the 2 % for the back seal. When the rotation factor increases. Disk friction decreases and axial thrust decreases as well due to a larger pressure drop in the side cavity. This is in good agreement to the thrust curve when comparing the thrust at the front and at the back. The front cavity shows smaller increase in thrust due to the increase in rotation factor. In general the back leakage path features a higher rotation factor around nominal loading at the inlet and therefore lower axial thrust at higher flow coefficients. The changes in rotation factor can be linked to the averaged velocity profile in the impeller exit. The meridional view 9.6 of the averaged circumferential velocities in stationary frame shows that the flow field at the front leakage entrance changes to a larger amount as compared to the back leakage entrance . It can also be seen that the overall circumferential velocity in stationary frame increases with decreasing flow coefficient. The change in local flow field causes a change momentum in the leakage flow entering the side gaps thereby changing thrust and losses.

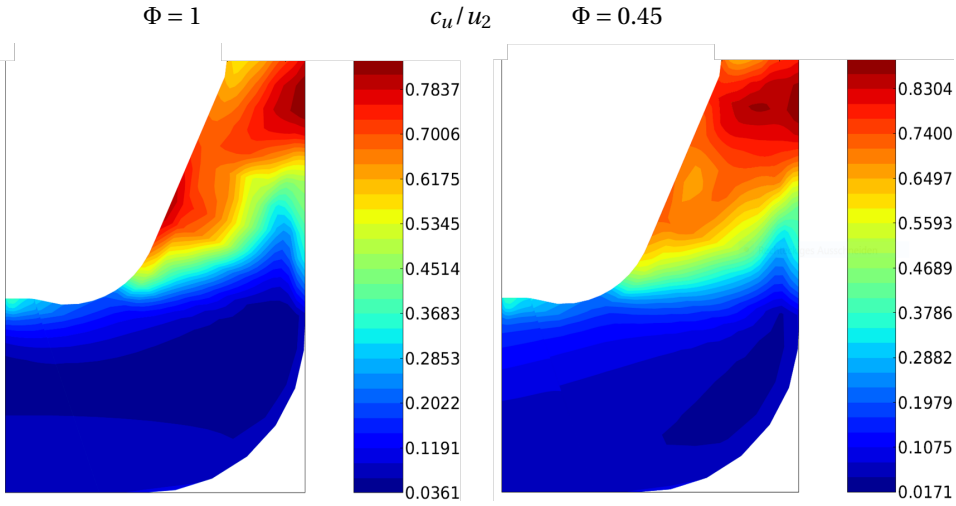

Figure 9.6: Circumferential velocity in stationary frame c_u / u_2 averaged on the meridional plane

9.3. Conclusions

The different loss mechanisms and axial thrust have been analyzed applying the same methods that were used on the full-annulus geometry. The impeller efficiency is presented in figure 9.7. It can be seen that the reduced numerical model features a larger effect on the hydraulic efficiency. These values however are also subject to high numerical uncertainties. The fluctuations of the impeller-only model are presented in figure 9.1. The trend can still be observed. The chart 9.1 summarizes the effects of the individual loss mechanisms and the axial thrust.

The largest effect by far is again the lost power due to leakage mass flow. Furthermore it can be seen that all the loss mechanisms increase their impact on the efficiency when flow coefficient is lower.

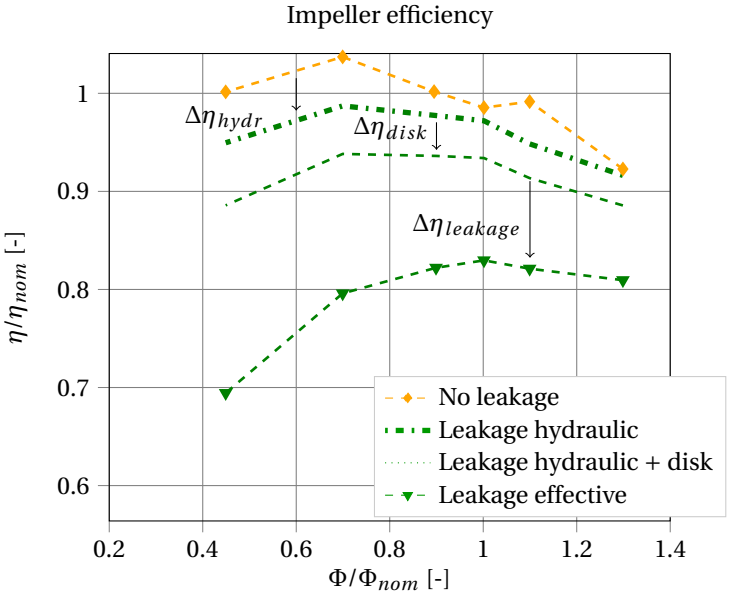

Figure 9.7: Efficiency drop due to leakage

Table 9.1: Effects on impeller efficiency impeller model

	Flow coefficient		
Mechanism	high	low	
Hydraulic losses due to leakage injection	0.8 %	5 %	numerical error ±3%
Disk friction losses	3.3 %	6.3 %	
Leakage losses through seals	8.3 %	19.7 %	
overall	12.3 %	31 %	
Axial Thrust	3 %	-1 %	

10

Analytical Model

In this chapter the implementation of the common analytical models from literature for losses and thrust due to secondary flow paths and their results are presented. The two introduced models are taken from Gülich [21] and [20] who refers to the work by Zilling (1973) [15] and Möhring (1976) [29] which focus on the modeling on the rotation factor with superimposed through-flow as it is present in the investigated case.

10.1. Program structure

As presented in the modeling section of the literature review the models are based on the equation of conservation of angular momentum in the sidewall gaps and empirical correlations from experimental data. Modeling the rotation factor and the development of it in the side cavities allows for predictions in terms of disk friction, axial thrust and leakage mass flow. The formula are presented in section 4. In this section the implementation of the models and its functionality is presented. The simplified geometry of the sidewall gaps is captured in the model using the parameters presented in figure 10.1.

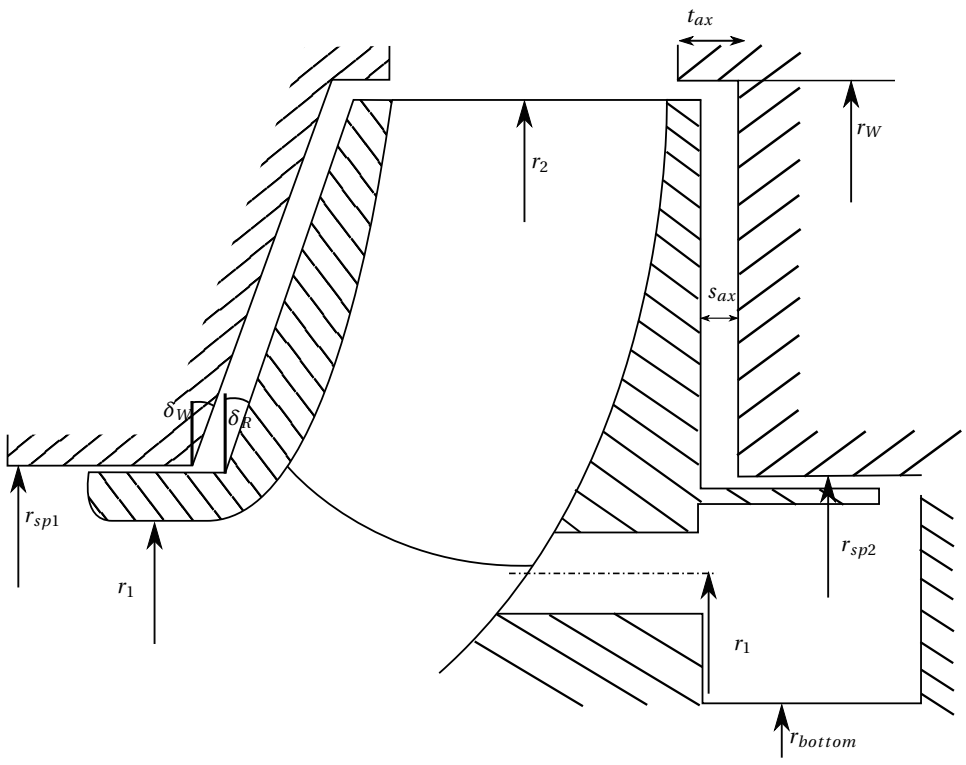

Figure 10.1: Meridional view and geometry definition

The flow chart 10.2 presents the working principle of the analytical model based on the correlations from Gülich.

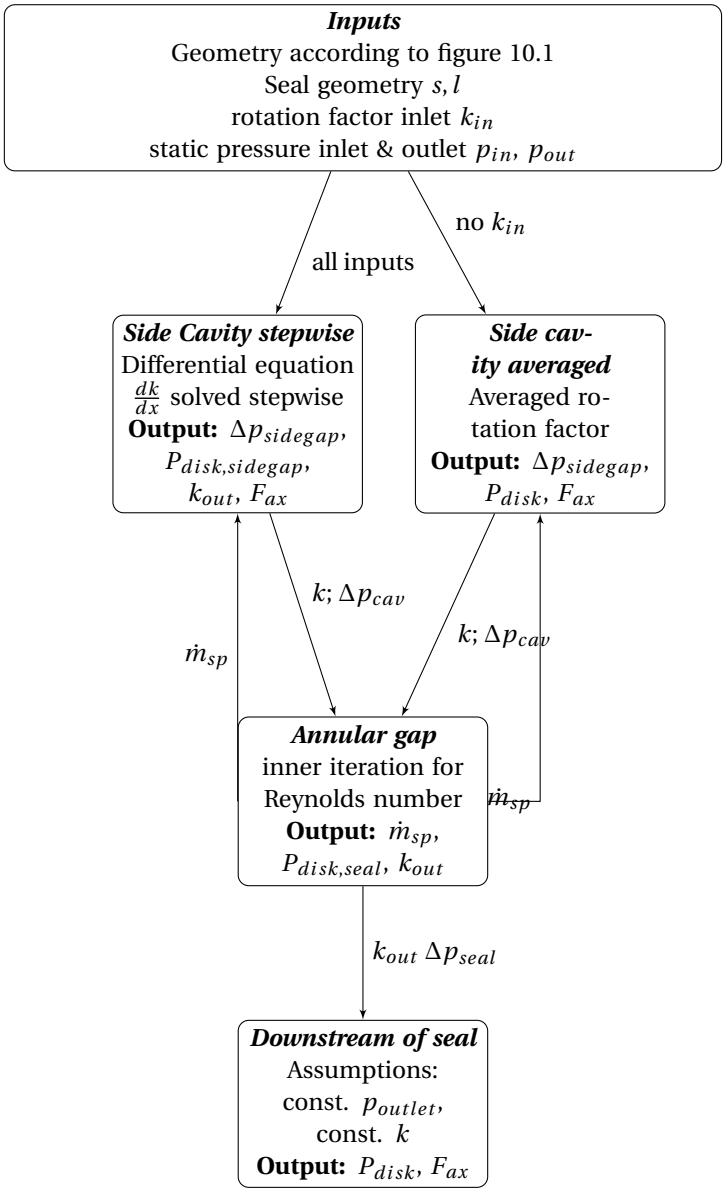

Figure 10.2: Work flow of empirical loss and thrust model program

According to figure 10.2 the inputs for geometry inlet rotation factor as well as the static pressure difference generated by the impeller is needed from the user.

Depending on whether the iterative method is used or the averaged method, the inlet condition of the rotation factor k_{in} is needed as well. The assumption on the inlet rotation factor can be $k_{in} = 0.5$ or based on numerical results of simulations without sidewall gaps. Based on the presented equations the pressure drop and the disk friction as well as the development of the circumferential velocities in the side cavity is calculated based on the input values. The leakage mass flow impacts all the desired values. The annular gap module deals with the seal and calculates the leakage mass flow and the disk friction in the annular gap based on the input from the side cavity module. An inner iteration is required for the leakage mass flow since the Reynolds number which determines the friction coefficient λ depends and the axial flow speed which is directly connected to the leakage mass flow by the continuity equation. The resulting leakage mass flow is then given back to the side cavity module where the pressure drop is recalculated along with the axial thrust and disk friction. The iteration is performed until the difference between two iterations becomes less than 0.1 %.

The region downstream of the seal features the assumption of constant k and constant pressure. The results presented in the previous chapters show that pressure drops further after the seal and the rotation factor increases. A possibility to extend the program and add a second side cavity loop to the working principle needs to be investigated in further research. However the implemented model follows the instructions presented in *"Centrifugal Pumps"* by Gülich [21].

The seal gap width has the highest impact on the leakage mass flow and therefore also changes the axial thrust and disk friction. In the next figure 10.3 the seal gap width has been changed and the effect on the leakage mass flow as well as disk friction and axial thrust can be seen. This change has been done for the averaged model and for the geometry of the front sidewall gap. Large changes in the seal gap width cause divergence in the iterative method that solves the differential equation.

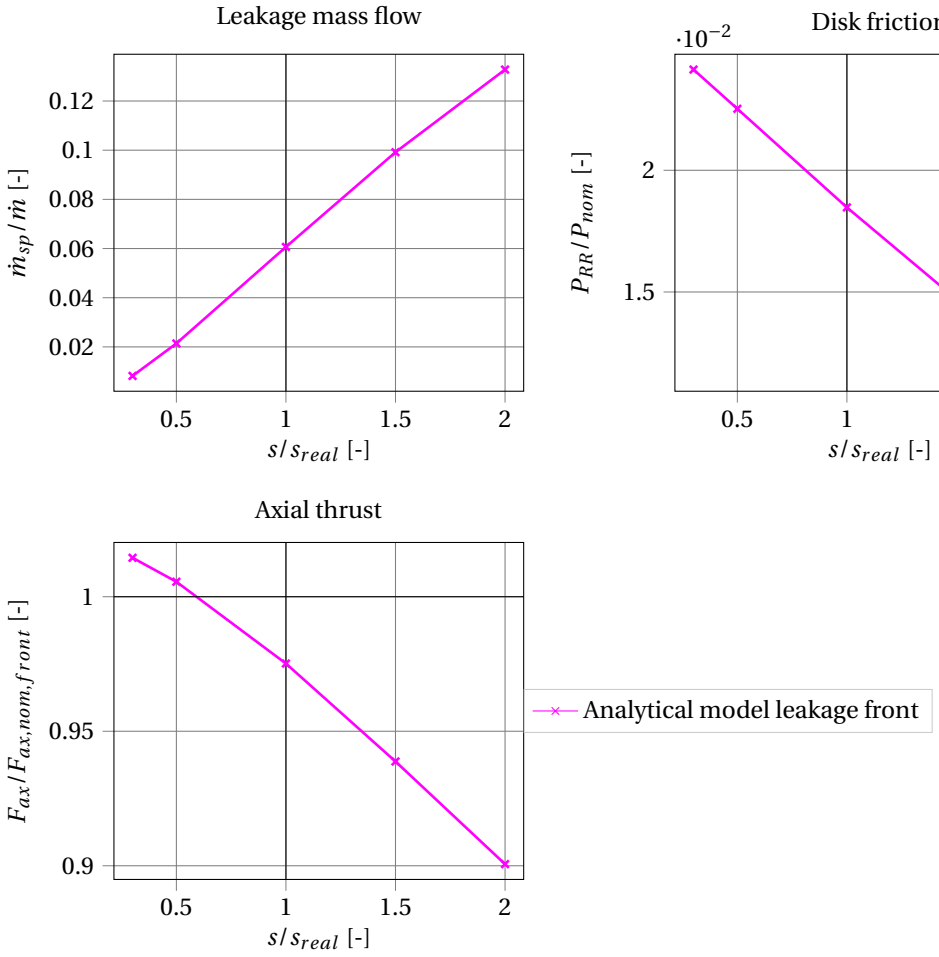

Figure 10.3: Impact of seal gap width on mass flow, disk friction and axial thrust in the front sidewall gap

Leakage mass flow is largely dependent on the seal gap width. One can see, that reducing the width by two leads to a reduction of leakage mass flow by three. The disk friction and axial thrust change as well since the rotation factor changes with the leakage mass flow. Higher mass flow leads to lower thrust and lower disk friction. The difference in the two models becomes evident in the following plots 10.4. When changing the gap width the leakage mass flow changes according to figure 10.3. The amount of leakage mass flow impacts the rotation coefficient in both models. The averaged rotation coefficient increases from $k = 0.53$ to $k = 0.59$ when leakage mass flow is tripled from $0.5s$ to s_{actual}. The iterated method starts with the same inlet rotation factor which is an input for that method. Throughout the passage the rotation factor increases for all amounts of through-flow. When leakage is increased the increase in rotation factor is increased. One can see that this leads to a large pressure drop in the side cavities. Looking at the resulting pressure distribution the two models show large differences in the shape of the curves. The average method features a larger gradient in pressure drop at the entrance of the side cavity which is then slightly reduced towards the seal. The iterative method increases the gradient in pressure drop with decreasing radius, which leads to large differences at

lower radii to the averaged approach. In both cases the pressure drop is higher when leakage flow is increased. A higher pressure drop in the side cavity leads to a smaller pressure difference across the sealing path. The pressure difference across the seal is coupled to the flow velocities in the sealing paths and therefore also to the overall leakage mass flow. The lower the pressure difference across the seal the smaller the leakage mass flow. Therefore the leakage mass flow through the side gaps has a self-stabilizing effect when directed radially inwards, this is in agreement with the investigations from literature [21].

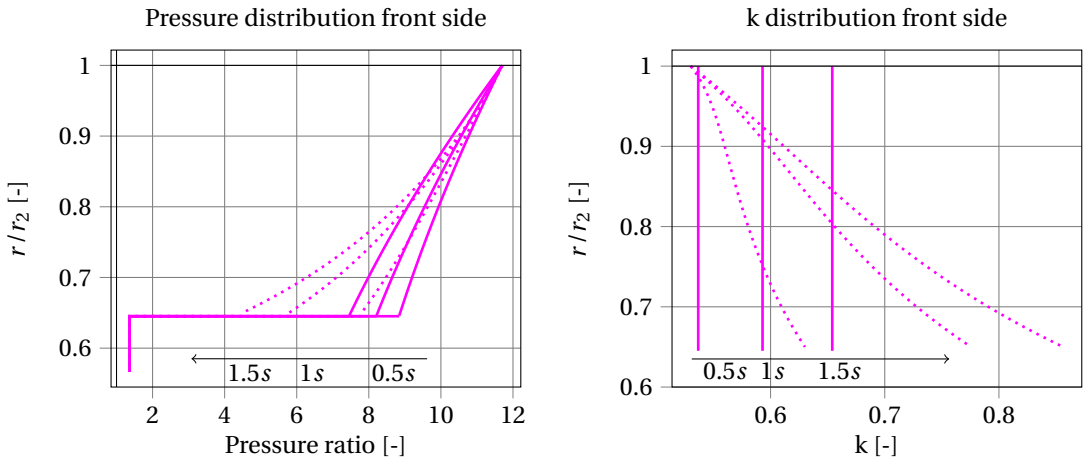

Figure 10.4: Impact of leakage mass flow changes on both models

10.2. Results

First, one of the analytical models is selected to be compared to the reduced numerical model. It is compared with the full-annulus model including secondary flow paths in nominal operation.

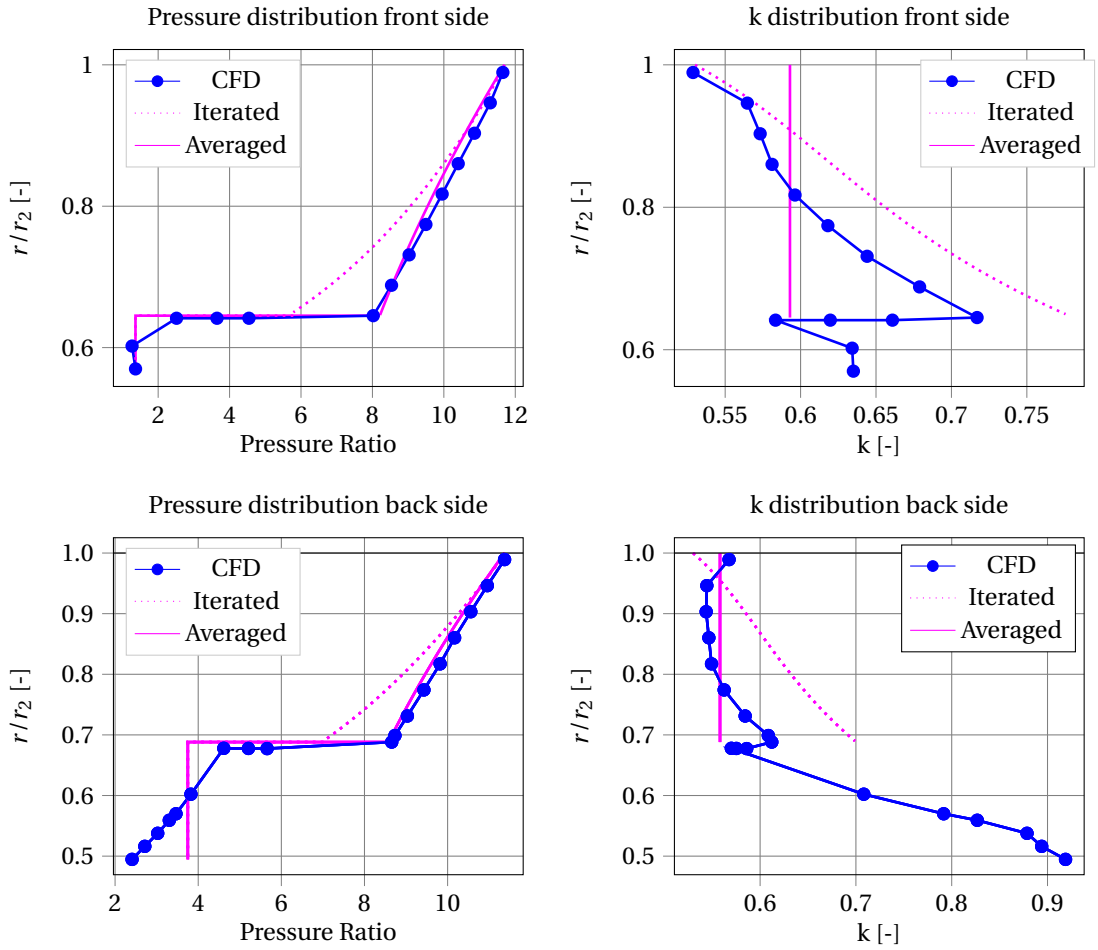

Figure 10.5: Comparison of both analytical models to numerical results in nominal operation for front and back seal

There are several observations possible. One can see that the assumption of constant pressure at the outlet does not agree with the numerical results. This leads to a larger pressure difference across the sealing path assumed in the analytical model. However the resulting leakage mass flow rate from the analytical model is still predicted lower than the numerical simulations suggest as it will be shown in the next chapter 11. The assumption for the effective roughness in the seal enters the equation. The numerical simulations were performed with the smooth wall boundary condition. To create comparable results the roughness in the seal should be chosen accordingly. The *CFX*-manual [16] provides a range of roughness values that are connected to the smooth wall assumption of $(0 < h_s^+ < 5)$ with $(h^+ = hu_\tau/\nu)$. Gülich gives values for the equivalent sand grain roughness $(\epsilon < 100\nu/w)$. These calculations lead to roughness values of $\epsilon < 2.5 * 10^{-6}$. The best results for leakage mass, disk friction and axial force have been obtained with roughness values of $\epsilon = 1.5 * 10^{-6}$.

As can be seen in figure 10.5 the iterated model overestimates the increase in rotation factor in the side gap. This leads to a large pressure drop, low axial forces, low disk friction and low leakage mass flows. The averaged method shows a better agreement to the pressure distribution from numerical results, the same trend can be seen in terms of axial forces and disk friction as well as leakage mass flow. Therefore the averaged method from Gülich is used for the comparison to the numerical models. Looking at the back side cavity similar observations are possible. The pressure drop is overpredicted by the iterated model along with the increase of the rotation factor throughout the cavity. The averaged rotation factor shows a better overall agreement to the rotation factor from numerical results.

The assumption that the pressure reduces to the outlet pressure is wrong and leads to misleading results especially for the backside cavity. As on can see in figure 10.5, the pressure drop downstream of the seal in the back is not insignificant. The outlet pressure assumption is adapted so that an outlet pressure of the seal is assumed to be 22 % of the static pressure difference in the impeller. With this correlation the analytical model gives better results when compared to numerical results than with the outlet pressure assumption. The number of balance holes is expected to influence the pressure drop in the chamber downstream of the back side seal. A second analysis of a pump which features balance holes in every passage follows in chapter 12.

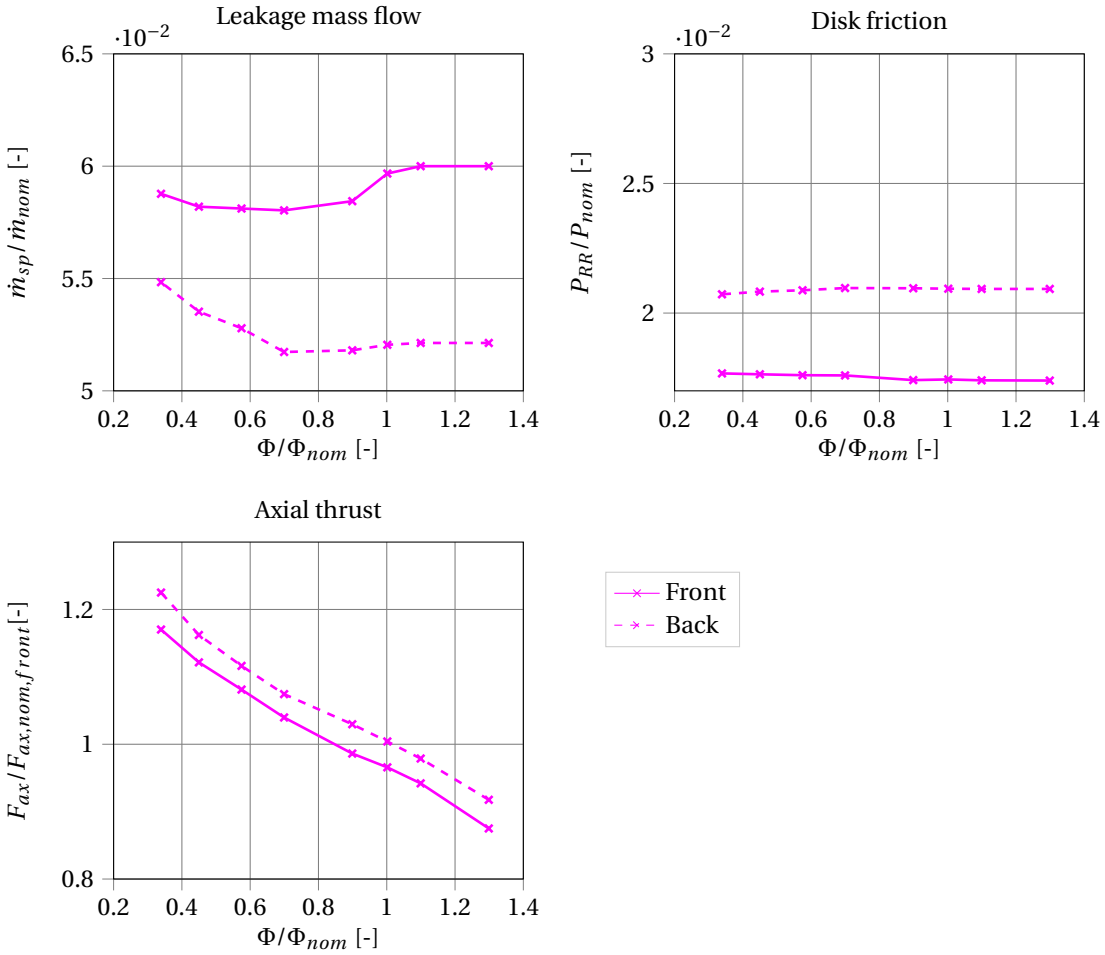

Figure 10.6: Leakage mass flow, disk friction and axial forces of the analytical model

Applying the correlation and using the averaged method to model the rotation factor leads to the results for the first pump 10.6. The driving parameters are the overall pressure level and the static pressures at inlet and outlet. The results of the model do not feature a shift in thrust direction or leakage mass flow.

11

Model Comparison

In this chapter the three different models are compared and the two simplified models are evaluated in their accuracy to predict the major losses. First the two numerical simulations are compared in the global characteristics and then the effects in the sidewall gaps are analyzed. The last section will involve the analytical model as well which leads to a chart in which the losses are quantified and the prediction capabilities are listed.

11.1. Hydraulic losses due to leakage injection

The head curve for both the full scale and the impeller model are presented in figure 11.1. It can immediately be seen that the simulations behave differently. At high flow coefficients the head of the impeller model is determined lower than the impeller head of the full scale model. Around nominal operation the results are closest and the difference in hydraulic performance between leakage and no leakage is modeled best. At low flow coefficients the head of the impeller model exceeds the head of the full scale model in both the leakage and no leakage model. The reason for the differences can likely be found in the inlet conditions. The averaged velocity angles from nominal operation at the inducer exit do not represent the velocity profile at partload.

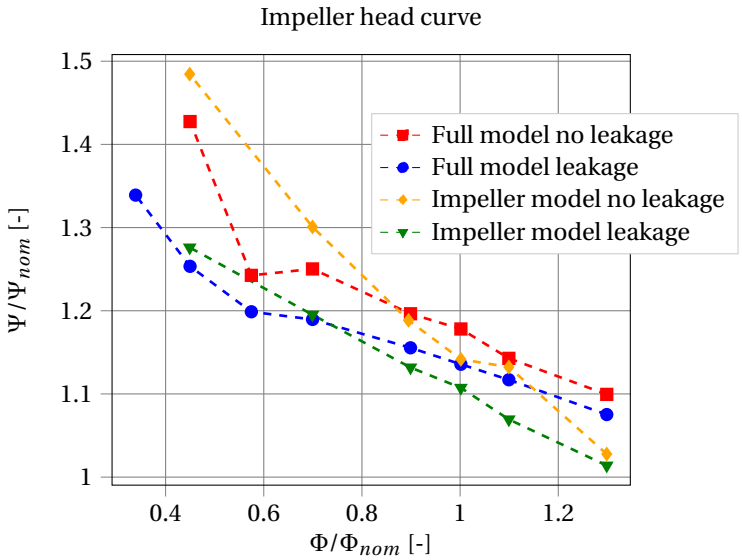

Figure 11.1: Impeller head curve both numerical models

The impeller efficiency of both models is plotted in the following figure along with the hydraulic losses of both models. The losses are in agreement with the head curve showing higher losses of both the impeller models at high flow coefficients and lower losses for low coefficients when compared to the full-annulus results. The difference between simulations with leakage and without leakage makes up for the amount of

hydraulic losses due to leakage injection. The remaining numerical fluctuations ±3 % to ±4 % of the impeller models are higher than in the full-annulus setup. That leads to larger uncertainties when calculating the hydraulic losses. The trend of increased hydraulic losses at low flow coefficients can still be observed. The impeller efficiency of the impeller model is too low at high flow coefficients and too high at low flow coefficients in case of the simulation without leakage. When looking at the differences due to leakage of the individual model it can be observed that even though hydraulic performance drop is over estimated compared to the full-annulus simulation the overall performance difference due to leakage is still within a $1-2$ % efficiency points drop range. At high flow coefficients the overall efficiency drop due to leakage is estimated less than 1 % too low compared to the full scale model.

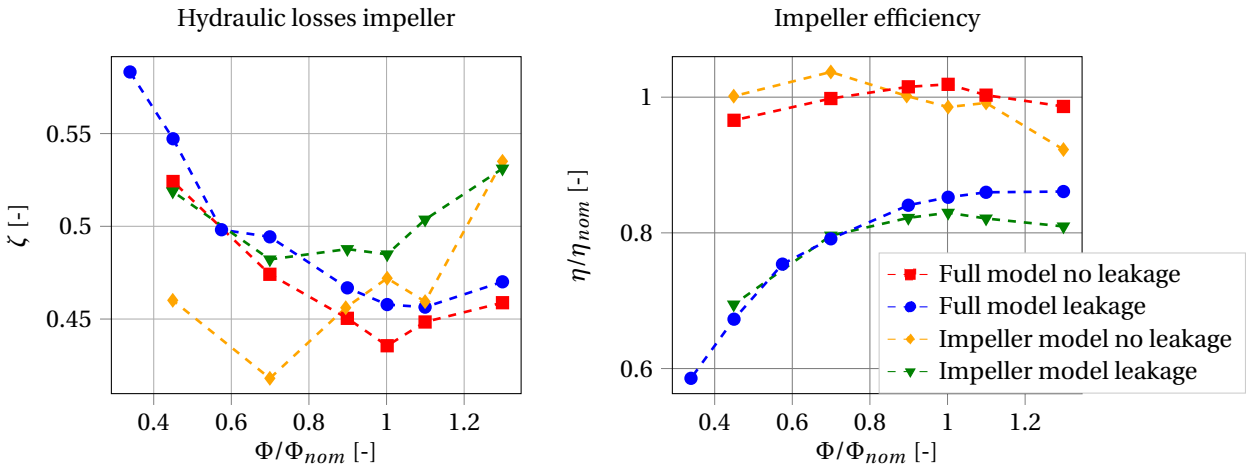

Figure 11.2: Hydraulic losses and efficiency curve both models

11.2. Secondary losses and thrust

The disk friction and the axial thrust is shown for both models and for both sides in figure 11.3. As already explained in the model section, the behavior of the two models and on both sides differ especially at low flow coefficients. Starting with the disk friction, one can see that friction in the backside cavity is higher than in the front in the full scale model, this is understandable even without considering through-flow or circumferential velocities since the wetted area of the rotor is larger in the back. Looking at the full-annulus model calculations the disk friction decreases when lowering the overall flow coefficient and then features a drastic increase starting in the front side cavity. The increase in friction is also visible on the backside but less strong. This effect is due to the volute interaction and strong secondary flows around the volute tongue. The effects can nicely be linked to figure 11.4. The rotation factor for the full-annulus model behaves according to expectations when looking at the friction behavior. Apart from having a larger wetted area the lower rotation factor in the back cavity at high flow coefficients further increases friction which leads to the large difference at high and nominal operation. After increasing slightly in both leakage paths, the circumferential velocities drop drastically in the front side cavity and below the velocities in the back side. This leads to a quick increase of friction in the front. The backside shows a decrease in rotational velocities at flow coefficient around $\Phi_{nom}/2$. The impeller model shows a different behavior. The velocities in the back cavity are higher which leads to a decrease in friction compared to the full scale model but also compared to the front side in the impeller model. That is the reason why we can see that the friction in both sides is almost equal around nominal operation. The velocities in the back side remain almost constant with a slight increase therefore the disk friction decreases only slightly and steadily. The velocities increase more in the front side than in the back side which leads to a larger drop in disk friction in the front side cavity than in the backside cavity. Leakage mass flow can also be explained when looking at the rotation factor. Generally a lower rotational velocity leads to higher leakage mass flow because the pressure drop in the cavity decreases, which leads to an increase in pressure difference over the seal and therefore a larger mass flow. This effect is perfectly visible in the full-annulus model and also in figure 8.33. One can see that the lower rotation factor in the back cavity at higher flow coefficients leads to a slightly higher leakage mass flow. Reducing the flow coefficients first leads to an increase

in circumferential velocities and also to decrease in leakage mass flow in both secondary flow paths. The decrease of velocities at very low flow coefficient then also increases leakage mass flow. The relatively constant rotation factors across the investigated flow regime also lead to comparatively constant leakage mass flows in the impeller model.

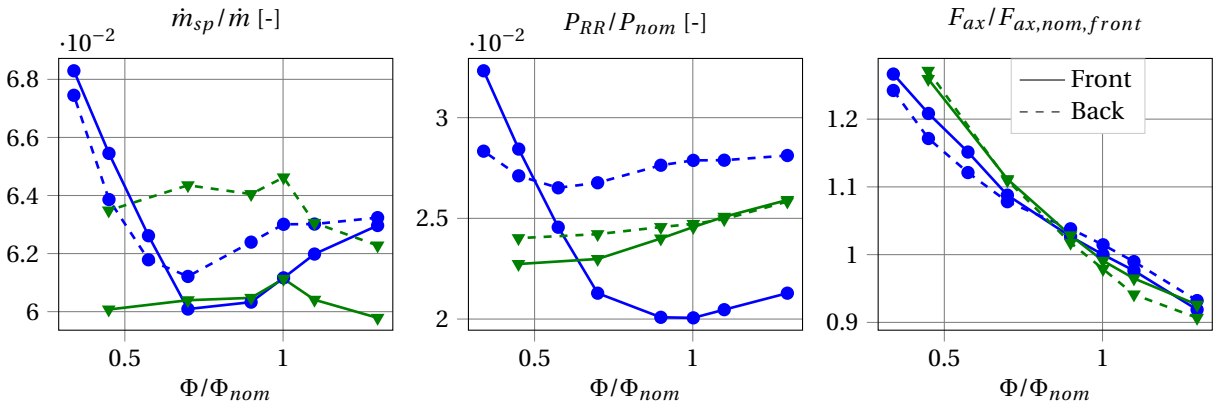

Figure 11.3: Leakage mass flow, disk friction and axial thrust

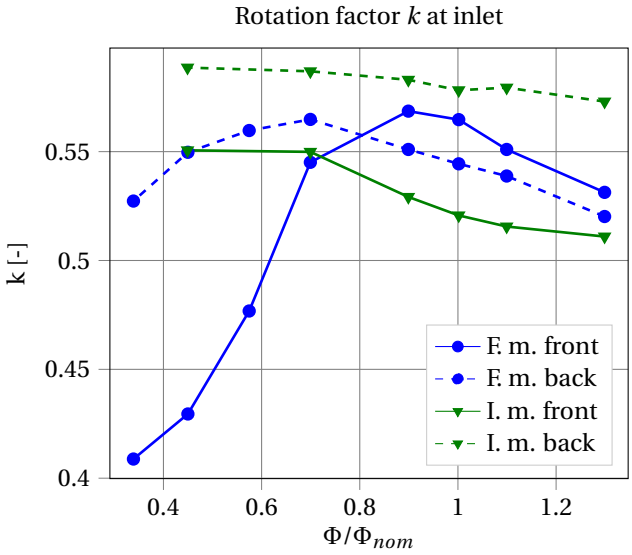

Figure 11.4: Development of inlet rotation factor for front and back leakage

The plot showing the axial forces can also be connected to the rotational velocities at the inlet of the individual sidewall gaps. The forces generally increase with lower mass flow along with the higher outlet pressure of the impeller. The impeller model features a steeper impeller characteristic curve as can be seen in figure 11.1 which leads to a steeper curve of the axial forces in general. When looking at the differences of the two models and the two sidewall gaps it can be seen that at high flow coefficients the back side cavity of the full scale model features a higher axial force than the front side, looking at the rotation factor one can see that the back side has a lower rotational factor which leads to lower pressure drop in the cavity and therefore to higher axial forces. When lowering the flow coefficients the low velocities in the front cavity lead to a drastic increase in forces in the front cavity which leads to a shift in thrust direction. The shift happens at the same flow coefficients at which the shift in rotational factor in the side gap happens. For the impeller model the shift in axial force happens in the opposite direction. This behavior can be explained with the changes in the inlet rotation factor, one can see the rotational velocities in the front sidewall gap increase quicker than the velocities in the back with decreasing flow coefficient. Therefore the front side features a less steep increase than the back leakage which leads to a shift in force direction. At high flow coefficients the back leakage

features lower static pressures due to higher rotational velocities in the sidewall gap entrance than the front leakage.

The Rossby number $\frac{w}{\omega r}$ gives information about the governing forces in flows in rotating passages. Flows in which rotation dominates have Rossby numbers much smaller than unity. Figure 11.5 shows the behavior of the flow in terms of Rossby numbers in different locations. The left figure shows the development at the impeller outlet and right shows the development upstream of the sidewall gap entrance. At the impeller exit the Rossby number steadily decreases, this is expected since the flow turns out more tangentially with lower mass flows leading to a larger circumferential velocity in stationary frame and a smaller circumferential velocity in relative frame and flow where rotational effects dominate the behavior. When looking at the Rossby number upstream of the leakage entrances a different behavior can be seen. Around nominal operation the Rossby numbers drop similar to how the impeller exit flow behaves. Below nominal operation the Rossby number increases especially close to the front leakage path. The reason for that can be found when looking at the volute flow field presented in figure 8.25. Close to the tongue flow with high radial velocities enters the side gaps thereby blocking the upstream circumferential flow. The circumferential velocities decrease and disk friction and axial thrust increase. The plot also shows the development of the Rossby number in the model without leakage. Similar trends can be seen when compared to the leakage model but the increased secondary effects in the volute with leakage become evident (large differences in velocities in front and back side). This underlines one problem with analytical models from literature because here the rotation factor at the inlet needs to be assumed or taken from numerical simulations which do not feature secondary flow paths. Even when numerical results are present, taking the inlet rotation factor from simulations without leakage paths is likely going to give errors since the side cavities effect the flow in the volute and therefore the assumption as such.

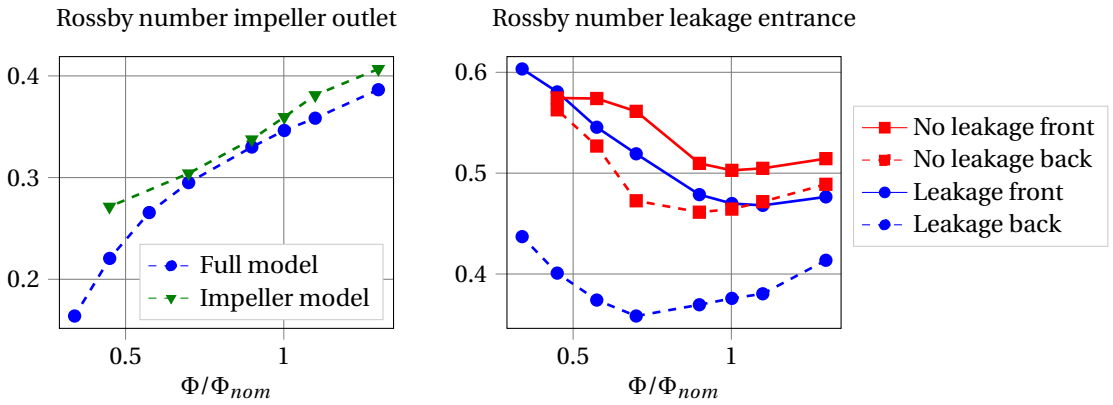

Figure 11.5: Rossby number at impeller exit and at entrance of secondary flow paths

11.3. Limitations and accuracy

The analytical model needs to be included to assess whether the losses and the thrust are captured with higher accuracy in the impeller model than in the analytical model. The main loss mechanisms which are leakage losses and disk friction and the axial thrust generated in the side cavities are presented in figures 11.7 and 11.6. One can easily see that the analytical model underestimates the amount of disk friction generated in the side cavities and that the impeller model gives a better result when compared to the full annulus simulations. The thrust behavior has been analyzed and thrust in the side cavities is overpredicted in the analytical model. When assessing the absolute values of the resulting force the impeller model gives good results but the development trend that the full annulus model presents cannot be captured. Leakage mass flow is captured with good agreement in the impeller model except for partload operation where drastic changes in the inflow conditions cause a steep increase in leakage in the full annulus calculations.

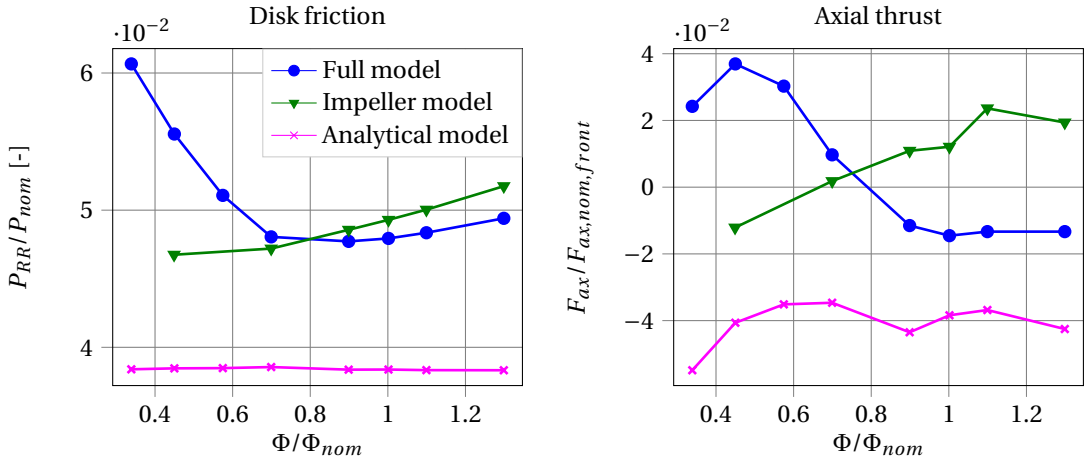

Figure 11.6: Disk friction and axial thrust of all models

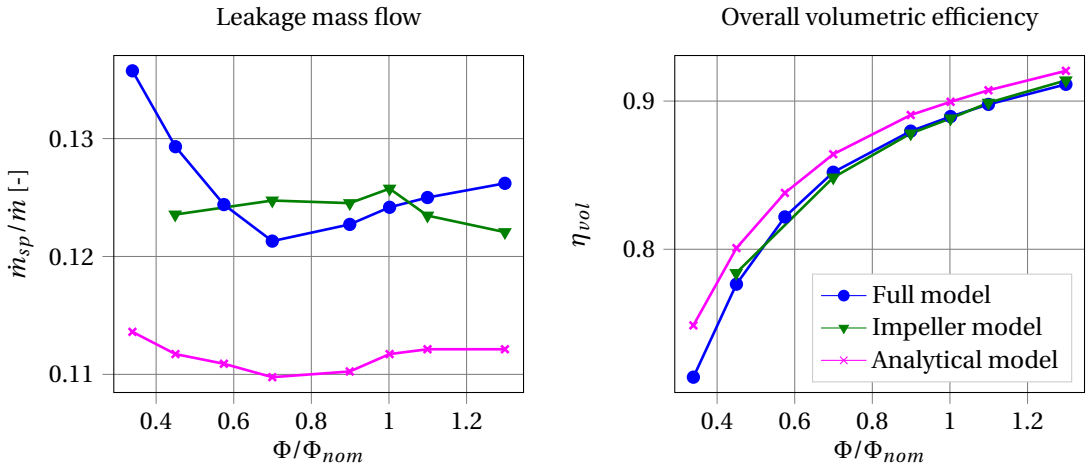

Figure 11.7: Leakage mass flow and volumetric efficiency of all models

The effects are summarized in table 11.1. Here the individual loss mechanisms are quantified. The hydraulic losses are shown with their effect on the efficiency drop. The overall efficiency drop is shown in which all losses due to secondary flow paths are added.

The next figure 11.8 visualizes well how the prediction capabilities of the impeller model are improved when compared to the analytical model. Here the quantified effects from both models have been applied to the efficiency curve of the full scale model without leakage paths. One can see that the impeller model delivers values for leakage mass flow and disk friction as well as hydraulic losses due to leakage injection that match the full model leakage well. When the analytical model is applied the overall losses are underpredicted so that the resulting efficiency is estimated too high.

Table 11.1: Losses and thrust model comparison

Mechanism	Full model		Impeller model		Analytical model	
	high	low	high	low	high	low
$\Delta\eta_{hydr;impeller}$	1.5 %	2.9 %	0.8 %	5 %	–	–
$P_{RR}/P_{nom,CFD}$	4.95 %	5.55 %	5.2 %	4.7 %	3.8 %	3.8 %
$\dot{m}_{sp}/\dot{m}_{nom}$	12.7 %	13.7 %	12.2 %	12.4 %	11.2%	11.3 %
Overall efficiency drop	12.8 %	30.4 %	12.3 %	31 %	9.6 %	24.1 %
$F_{ax,resulting}/F_{ax,nom,front}$	-1.5 %	3.6 %	2 %	-1.2%	-4 %	-4.2 %

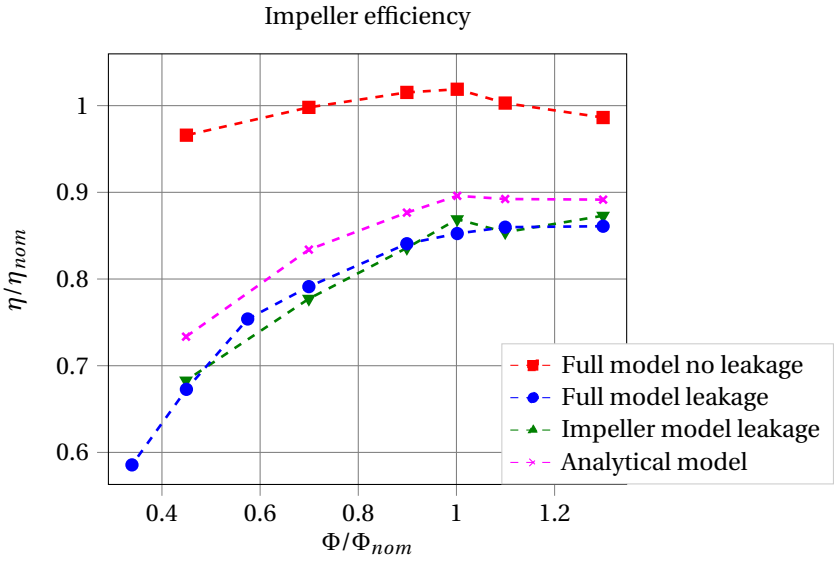

Figure 11.8: Impeller efficiency all models

The table 11.2 quantifies the prediction capabilities relative to the results of the full annulus model.

Table 11.2: Prediction capabilities

Mechanism	Impeller model		Analytical model	
	high	low	high	low
$\Delta\eta_{hydr;impeller}$	-46.6 %	72 %	–	–
$P_{RR}/P_{nom,CFD}$	5 %	-15.4 %	-23.3 %	-31.6 %
$\dot{m}_{sp}/\dot{m}$	-4 %	-9.5 %	-11.9%	-17.6%
Overall efficiency drop	-4 %	-2 %	-25 %	-21 %
$F_{ax,resulting}/F_{ax,nom,front}$	33 %	-66%	166 %	17 %

The figure 11.8 and table 11.2 show how the prediction capabilities are higher in the numerical impeller model. Especially in terms of losses the overall efficiency drop is captured within approximately 80 % improved accuracy. All loss mechanisms are captured better in the impeller model: Disk friction approximately 60 % and leakage mass flow rate by about 60 %. Additionally hydraulic losses due to leakage injection are captured in the numerical model and not in the analytical model. The thrust modeling is subject to high uncertainties especially because the force on both leakage sides is well balanced in the examined case. Still the uncertainties when compared to the full annulus results are decreased by 50 %.

The analysis is solely based on the comparison between numerical results and empirical correlations. Experimental data that give information on the losses and thrust generated in the side cavities are not present in the two investigated pumps. The experimental data that are available merely show the global characteristics. Figure 8.1 shows how the characteristic curve differs between numerical results and experimental data revealing the limitations that numerical simulations of pumping systems are subjected to. A major source of errors in the calculations made is the interface modeling of the impeller volute intersection. The available interfaces in *ANSYS-CFX* are frozen- rotor approach and stage mixing approach. When frozen rotor approach

is picked only a single relative position to the volute is investigated which can lead to results that feature extreme upstream clogging effects originating from the volute tongue. The stage-mixing plane approach uses a circumferential averaging method and should only be applied when small or no recirculation through the interface is present. Using the stage mixing plane on volute impeller interfaces is not recommended. Both methods create numerical errors that lead to diverging characteristics of the pump behavior. Cavitation is not modeled in the numerical calculations which impacts the pump performance as well if present in reality. Turbulence modeling and the lack of roughness resolution in the models render numerical loss calculations uncertain to about ±10% [21]. The conclusions based on the hydraulic performance of the pump in both cases, full annulus and impeller model need to be drawn with caution. Small effects like the change of hydraulic losses due to leakage injection can likely be a result from wrong modeling of the pump. Residuals and the remaining fluctuations in the properties remain high for the simulations (Root Mean Square $RMS = 1e^{-3.5}$) and fluctuations in power and pressure from ±0.2 % in nominal operation and full annulus to ±5 % impeller model partload. Trends can be analyzed and understood but the quantifications of the hydraulic losses in tables 11.1 and 11.2 need to be questioned.

When assessing the leakage losses and thrust however the difference between two simulations that are set-up in the same way is investigated. The interfaces between the leakage path's and the main passage create less errors since the frozen rotor approach can better be applied here due to the rotational symmetry. So the investigation of the differences between two simulations can still be meaningful because both simulations are subject to the same source of errors. Further reassurance that the results can be applied to real pump cases can be found when looking at the analytical results. These have been established over a long period in the 20^{th} and 21^{th} century and validated with experimental data on multiple occasions. The trends and quantities determined by the numerical models can be anchored with the analytical estimations. The physical effects that are explained in literature can be found in the numerical results as well, for example: Impact of circumferential velocity on friction and leakage mass flow, recirculation in volute effects flow in side gaps. This gives confidence to the meaningfulness of the results.

12

Second Pump

12.1. Sidewall gaps design

On the basis of the analytical model the outline of the sidewall gaps in a second pump design has been defined. The pump is designed for the same application and flow regime featuring similar geometric constraints in terms of diameter length and weight. The key criterion for the sidewall gaps is the balance of the axial forces. The minimum of losses associated with the secondary flow paths play a subordinate role. The design of the sidewall gaps is subject to many geometric constraints due to the impeller geometry. The position of the inlet and outlet of the front gap is determined by the impeller and volute geometry. In this case the sidewall gaps are directly attached to the impeller outflow and not designed openly to the volute. This aspect encourages the implementation of a reduced numerical model also for this pump since the side cavity entrance does not need to be manipulated for the reduced model.

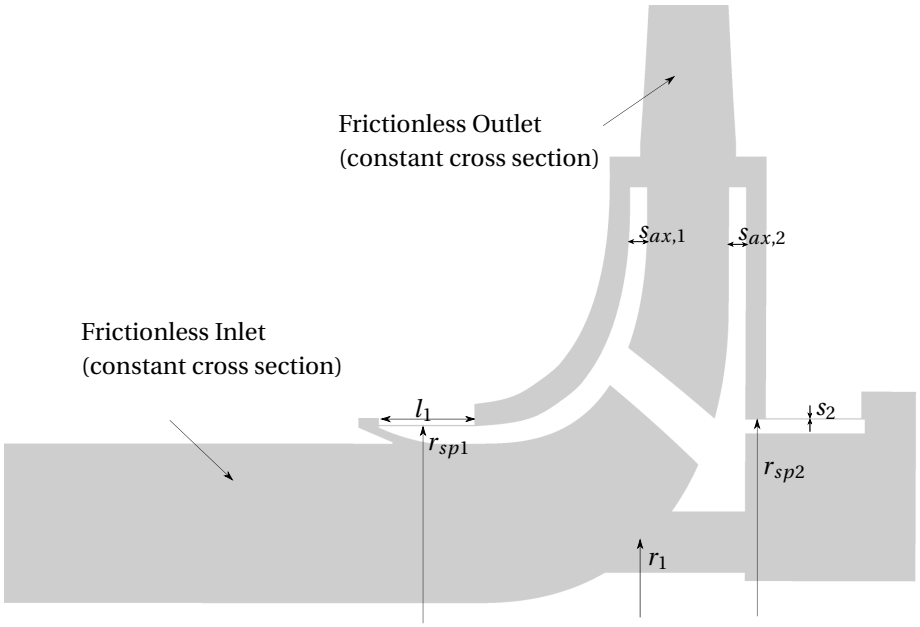

Figure 12.1: Sidewall gap design parameters

Figure 12.1 shows the sidewall gap design in a meridional-cut view. The implemented seals feature the same characteristics in terms of length l and gap width s as in the previous pump. To reduce the leakage flow the radius r_{sp1} where the seals are implemented must be chosen as low as possible, to allow for a large pressure drop in the side cavity upstream and therefore a smaller static pressure difference across the seal gap. The minimum seal radius on the front seal is determined by the shroud thickness and inlet radius.

The side cavity design was done based on the geometric parameters that enter the equation for the rotation factor without through-flow 4.17. The shroud has been designed with a constant thickness which determines the shape of the rotating wall in the front cavity. The remaining parameters that enter the correlations are presented in figure 3.2 in the literature review. The stator angle δ_W and the side gap width s_{ax} are chosen so that the rotation factor k_0 gets largest. A high rotation factor leads to lower disk friction and a larger pressure drop in the side cavities which reduces the leakage mass flow. The calculations yield maximum k_0 with smallest angle δ_W and smallest t_{ax} which is the overlap of the volute geometry over the side gap entrance and directly linked to the side gap width s_{ax} according to figure 10.1. The leakage exit is designed so that the injection takes place at small angles relative to the main flow direction to reduce mixing losses.

Gülich [21] gives a recommendation for the smallest axial clearance to allow for a core flow region in the flow field. The axial clearance should be designed so that $0.015 < \frac{s_{ax}}{d_2} < 0.04$. Furthermore, excessive fluid volumes in the sidewall gaps shall be avoided in order to prevent high disk friction losses.

Thrust balancing has been performed for nominal operation, values for static pressure difference across have been taken from a single full-annulus calculation without sidewall gaps. The radius of the backside seal has been changed in order to match the axial thrust generated in the front leakage path. The remaining design choices for the backside cavity have been made similarly to the front side. Minimal angle and minimal axial clearance are the key parameters that describe the backside cavity's geometry. Downstream of the backside seal a larger volume is present. The bottom radius of that chamber is determined by the shaft diameter in that region. The balance hole position and diameter was chosen according to guidelines stated in [21]. The balance hole injection should take place in all the impeller passages to achieve a more uniform passage behavior. The diameter should be chosen so that the overall cross sectional area of the balance holes is 5 times larger than the cross sectional area of the sealing clearance. Information on the preferred injection location could not be found. The preceding study on the first pump does not hint at better injection locations, since only one location is investigated. The injection needs to take place on lower radii than the seal. The center of the impeller passage is chosen again.

The balancing of the forces for the first design loop was done with the assumption that at the outlet of the seal the static pressure of the outlet of the whole leakage path is reached. The number of balance holes is expected to play a role and with balance holes in every passage the correlation applied for the analytical model for the preceding pump of 22 % of the overall static pressure difference seems too high for this pump.

12.2. Numerical results

The setup of the single-impeller model was done according to the preceding numerical model. However some differences are applied to the second pump. The interface between the impeller and the outlet diffuser is defined with the frozen-rotor method. The choice is reasonable since the diffuser merely represents a frictionless space with constant cross section which is rotationally symmetric. Furthermore only a single impeller passage is calculated since every passage features balance hole injection and therefore a symmetrical flow field between the individual passages can be expected. The interfaces between the balance holes and the backside cavity and the impeller are defined with the frozen rotor interface.

The resulting flow field in three different operational conditions can be seen in figure 12.2. There are multiple investigations possible. The figure shows the velocity profile in relative frame of reference close to the hub at mid-span and close to the shroud. One can see that for all the flow coefficients the differences between hub, shroud and midspan are smaller compared to the preceding pump. This can be explained with the blade design which features changing blade angles over the span. The previous pump featured constant blade angles. The blade angles are higher close to the hub and lower close to the shroud leading to a more uniform velocity profile and blade loading from hub to shroud.

The other main investigation can be made when comparing the velocity profiles in different operating conditions. Around nominal loading separation occurs on the suction side and a region of low momentum flow develops over the pressure side originating from the leading edge. When flow becomes more meridional towards higher flow coefficients the separation region on the suction side shrinks but the region of low momentum flow on the pressure side remains. When the flow becomes more circumferential towards lower flow coefficients the separation region on the suction side grows, the low momentum region on the pressure side reduces. These observations are different to the ones made on the previous pump. A major difference

between the two blade designs that can explain the behavior is the sharp leading edge of the second pump when compared to the thick leading edge of the blades of the preceding impeller. Flow around blades with sharp leading edges features higher sensitivity to changes incidence angle as compared to blades with thick leading edges. In agreement to this the first impeller shows a rather similar flow field between different flow conditions (separation is always present at the suction side and at all operating points) whereas the second impeller shows more drastic changes due to changes in mass flow.

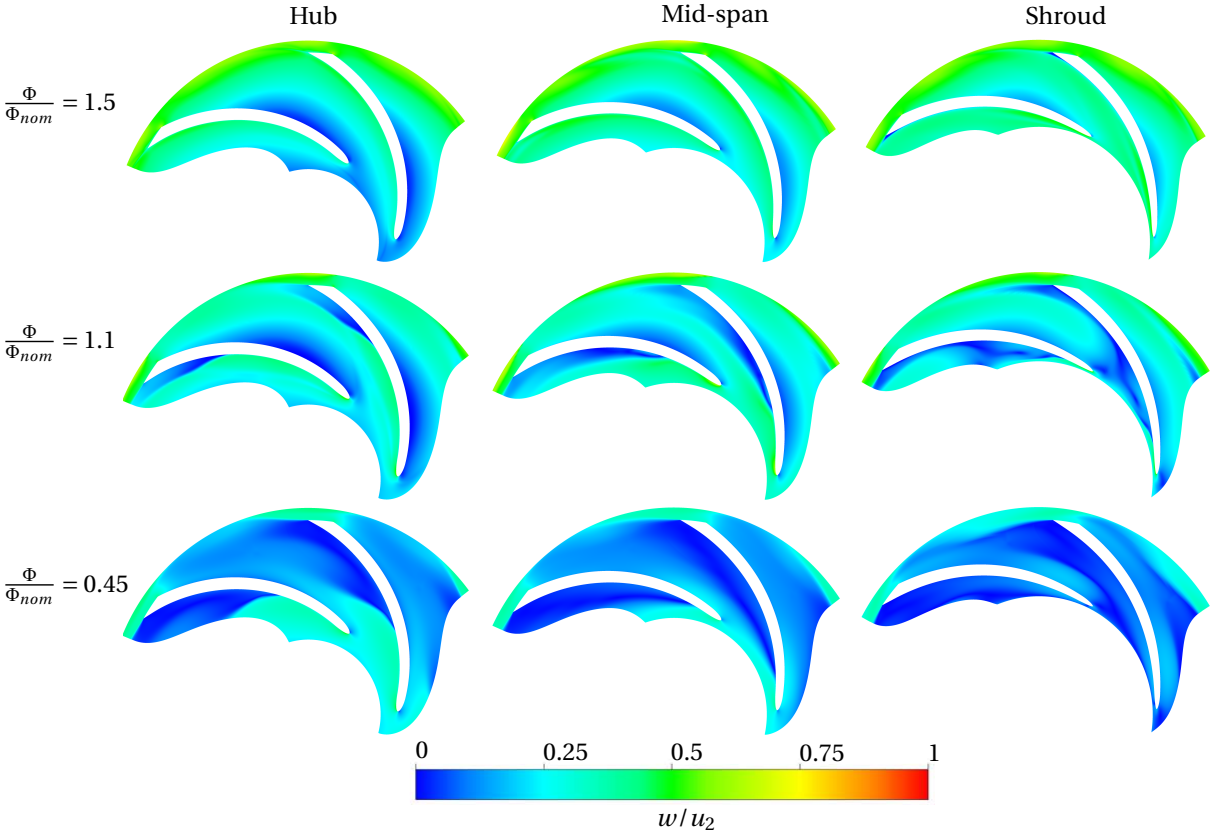

Figure 12.2: Impeller flow field around nominal operation, partload and overload

The following figure 12.3 shows the characteristic curves along with the hydraulic losses of the two models with and without leakage. In both cases the characteristic curves show a decrease in head coefficient with growing flow coefficients. A saddle-type shape like in the previous pump cannot be investigated. This is also in agreement with the analysis that the saddle-shape originates from the volute in the first pump since the volute is not present in the simulations of the impeller-only model. Experimental data are not available for this pump.

When comparing results with leakage and without leakage a couple of investigations can be made. At low flow coefficients the leakage injection leads to higher hydraulic losses in the main passage at loss minimum leakage increases losses by about $\Delta\zeta = 0.07$. This is in agreement with the investigations on the preceding pump. At high flow coefficients the leakage increases the performance by about $\Delta\Psi = 0.01$ and hydraulic losses are lower by about $\Delta\zeta = 0.02$. The loss minimum at around 60 % of the nominal flow coefficient reveals limits of the impeller model to capture the pump behavior as well as a full annulus calculation. This is something that has been seen in the previous reduced model as well. The highest efficiencies and lowest losses are reached at partload which is not shown in the full-annulus calculations.

There are multiple possible explanations for this effect. However, the key idea of the reduced numerical model is to capture the effects due to secondary flow paths which has been achieved with an improved accuracy when compared to analytical models. When reducing the numerical model by the inducer and the volute the performance impact of the individual components is missing. When only comparing the impeller performance the upstream and downstream effects of the inducer and volute are also missing. At partload for example the inducer creates recirculation at the impeller entrance and a change in the approaching flow angle. In the reduced numerical model the nominal flow field of the impeller outlet has been circumferentially averaged which creates an idealized velocity profile especially at partload which can lead to an overestima-

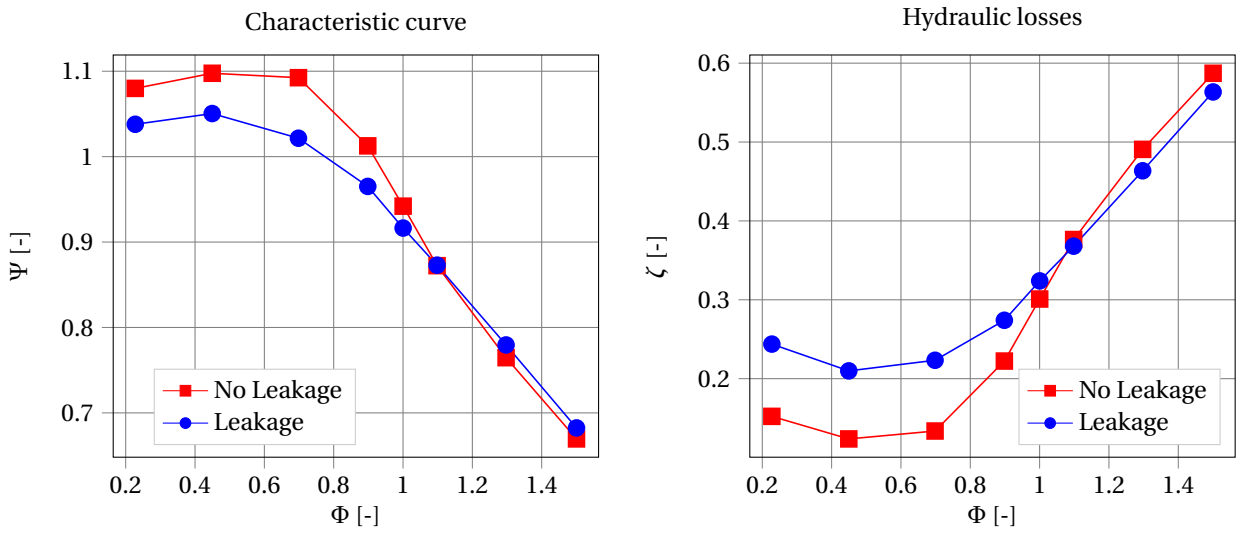

Figure 12.3: Characteristic curve and hydraulic losses second pump design

tion of the hydraulic performance.

The following figure 12.4 shows the velocity profile on the same locations and operating conditions as in figure 12.2 but when leakage paths are added to the impeller passage. The velocity profile at overload and around nominal operation show interesting effects of the leakage injection through the balance holes on the main passage.

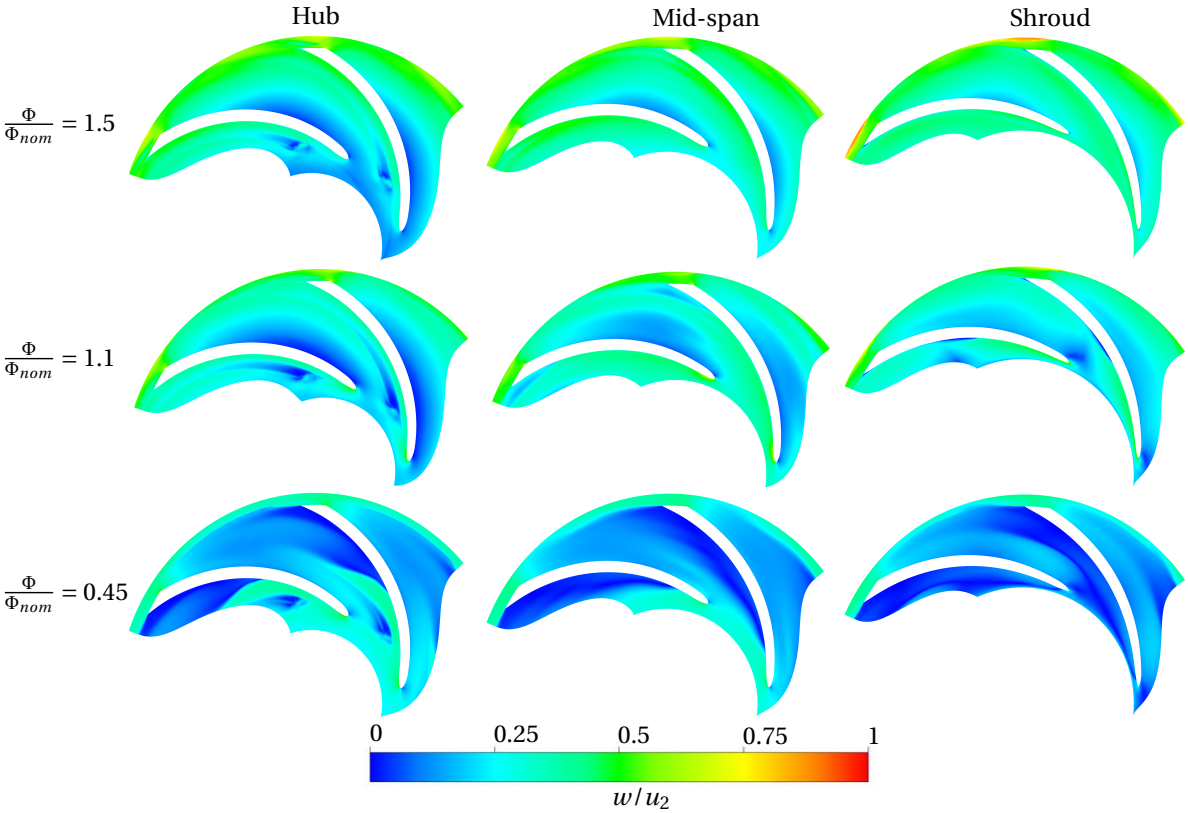

Figure 12.4: Impeller flow field with leakage around nominal operation, partload and overload

As seen in the previous pump the leakage injection leads to flow recirculation downstream of the balance

holes, which can always be seen close to the hub. The flow around the blades features regions of low momentum on the pressure side at overload. The leakage injection leads to a slight reduction of the size of the region which can be seen at slight overload $\Phi/\Phi_{nom} = 1.1$ and at $\Phi/\Phi_{nom} = 1.5$. In these cases the hydraulic losses are lower when leakage injection takes place. At $\Phi/\Phi_{nom} = 1.1$ more investigations are possible. Without leakage a separation on the suction side of the blade is easily visible and starts around 30 % of the blade length, when leakage flow is injected the separation onset is shifted downstream to 80 % of the blade length. As can be seen when looking at the wake downstream of the leakage injection at overload it is better aligned with the main flow, which helps the flow stay attached for a longer and increase the hydraulic performance.

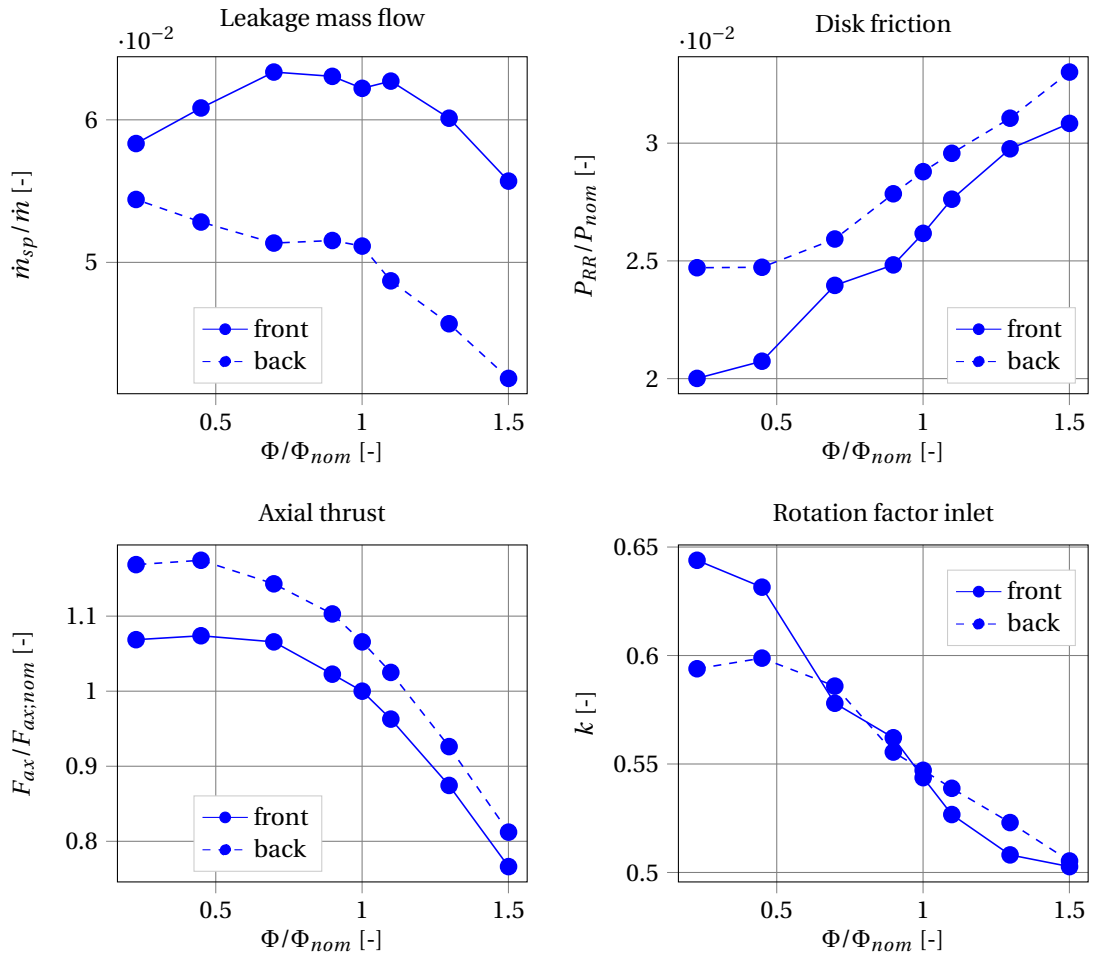

Figure 12.5: Loss and thrust behavior second pump

When the flow becomes more tangential at lower operating conditions the wake downstream of the injection location is tilted towards a more circumferential direction and interferes with the leading edge of the blade. This leads to a reduction of the frontal loading and the effective work output to the flow as seen in figure 8.21. This effect has been seen in the previous pump at all the operating conditions, and therefore comparably a more constant hydraulic loss effect of the leakage injection.

The secondary loss effects and the thrust development are presented in figure 12.5. The leakage mass flow increases from overall 10 % around partload to 11.5 %. Even though the same seal geometries (length and width) are implemented a slight reduction of leakage mass flow compared to the previous pump has been achieved. The seal diameter on both front and back seal has been reduced which allows for a larger pressure drop upstream of the seal and a smaller static pressure difference across the sealing gap. Furthermore a larger difference in leakage mass flow between front and backside cavity can be seen. In the previous pump the leakage mass flow through the backside cavity was higher at high operating conditions. In these conditions the rotation factor at the backside cavity was lower than on the front side cavity. In the currently investigated pump the rotation factor in the backside cavity is higher at high flow coefficients which leads to a reduction of leakage mass flow. When looking at low flow coefficients the rotation factor at the front side is higher which

leads to a reduction in leakage mass flow in the front side.

When looking at the disk friction development of both sides a close connection to the rotation factor at the inlet can be found again. Disk friction is higher in the backside cavity due to the larger rotating area. Due to the increase in circumferential velocities on both sides the disk friction reduces when overall flow coefficient is reduced. The rotation factor on the front side increases more than on the backside so that disk friction decreases more on the front side. In general the disk friction makes up about 6.5 % of the nominal shaft power at high loading and 4.5 % at low operation.

Axial thrust on both sides develops according to the static pressure head of the pump. One can easily see that the axial forces are not balanced well enough. The force is directed to the front side and increases towards lower flow coefficients from 4 % to 10 % of the nominal front side force. A second design loop is necessary where the backside seal diameter is increased. The differences between the analytical estimation and the numerical result originate mainly from the assumption that the static pressure at the seal outlet equals the static pressure at the injection location. A corrected assumption based on the first design loop would be: 11 % of the static pressure difference happens downstream of the seal when constant pressure distribution is assumed.

The impact on the efficiency is shown in figure 12.6. At overload operation the overall losses due to leakage are small when compared to partload operation. The effect is increased especially because of the large changes in hydraulic losses due to the leakage injection over the operating regime. The highest efficiency location is shifted towards higher flow coefficients due to the larger impact of leakage at smaller overall mass flows at partload operation.

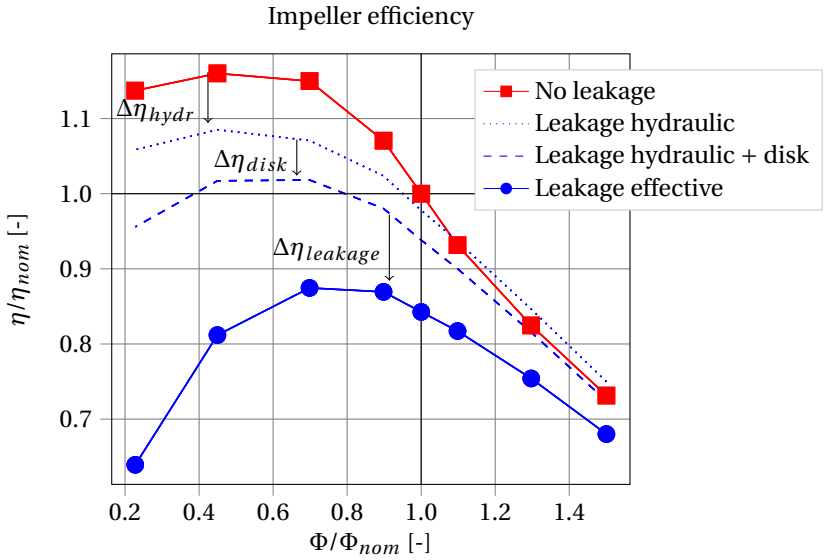

Figure 12.6: Efficiency drop due to leakage

The effects are summarized in the following table 12.1. The minimal flow coefficient investigated is lower than the minimal operating point in the previous pump. Therefore the losses seem larger when directly compared.

Table 12.1: Effects on impeller efficiency

Mechanism	Flow coefficient high	low
Hydraulic losses due to leakage injection	-2.7 %	7.1 %
Disk friction losses	4 %	9.1 %
Leakage losses through seals	6.1 %	33.2 %
overall	7.4 %	43.9 %
Axial Thrust	-5.6%	9 %

13

Conclusions and Recommendations

13.1. Conclusions

A reduced numerical model has been established which captures secondary losses and axial thrust with improved prediction capabilities. Furthermore the effect of leakage injection on the hydraulic performance and stability of the pumping system is captured with the new model which was not possible with the available models from literature. The impeller model offers a flexible and easy to set-up alternative to computationally expensive full-annulus simulations. The number of cells is reduced by the number of passages and meshing procedures are simpler since complex asymmetric and non-turbo components such as the volute are not part of the model.

Based on the findings on the first pump that was investigated the prediction capabilities in terms of disk friction have been improved. The analytical model for disk friction under predicts by about
≈ 30 %
which is also in agreement to the uncertainties mentioned in literature that are associated to disk friction loss prediction. The impeller model offers higher accuracy when compared to the full annulus calculations. In the investigated operating regime the disk friction prediction is predicted with ≈ 12 % with higher uncertainties at partload. These uncertainties result mainly from the interaction to the volute flow which is not captures in the impeller-only model.

The other secondary loss mechanism which is the leakage loss through the annular seal is captured with improved accuracy when comparing to the full annulus calculations. The leakage mass flow is well predicted by the impeller-only model by ≈ 6 % and leakage is predicted to about ≈ 16 % accuracy. Again the models diverge towards low partload operation due to the interaction with the volute flow.

The hydraulic losses due incidence change are not captured in analytical models. The model for the mixing process when leakage is injected [19] proves to be quite accurate the effect however plays a negligible role compared to the incidence change and wake building due to the leakage injection in the impeller passage. The impeller-model fails to present the same hydraulic characteristics as the full annulus model, which can be expected since downstream and upstream effects of the inducer and volute on the model are not captured and averaged inlet conditions are applied. The effect of the leakage injection shows same trends but the losses are overpredicted in the impeller model especially at partload ≈ 70 %. However leakage losses and disk friction make up the major part of the overall losses so that the overall loss prediction is improved upon the analytical model by about 80 % relative to the accuracy of the analytical model.
Investigations on the second pump show why the hydraulic impact of the leakage injection is hard to predict and therefore is not part of empirical correlations in literature. Even though the pumps are designed similarly and for the same operation and purpose the leakage injection losses behave very differently between pump one and pump two. In the second pump at high operation the leakage injection reduces hydraulic losses and improves the performance at low flow coefficients the injection increases losses.

The axial thrust prediction is subject to high uncertainties because the investigated pump shows a well balanced resulting force over the investigated flow regime. Uncertainties with the force on one side lead to higher uncertainties when the resulting axial force is determined which can even lead to a change in direction

of the force. When looking at the absolute value for the axial force the impeller model predicts the force with 50 % accuracy when compared to the full scale model. The analytical model leads to an overprediction of the axial force of 100 % approximately.

Unfortunately the set of experimental data is not sufficient to base the investigated trends on. The diverging behavior between the global characteristics questions the accuracy of the overall method. In these calculations multiple differences to experimental tests apply, such as: no cavitation, no roughness modeling and a large separation region which leads to uncertainties in any turbulence model. Differences are therefore expected. Especially the quantified hydraulic impact of the leakage injection needs to be dealt with with caution, since the effect is rather small and subject to high numerical fluctuations. The trend in the two investigated pumps that the leakage injection does not lead to a destabilization of the pump characteristics can still be seen.
The focus must rather lie on the investigated differences between the simulation with and without leakage and whether the correct trends in the loss mechanisms are captured. These can also be cross checked with the literature and the implemented analytical model. Differences between the analytical model are there but trends are similar and in good agreement with the physical description of the mechanisms. This gives reassurance that the results are meaningful.

13.2. Recommendations for simulation setup

The setup for the pump calculations is critical to ensure comparable and meaningful results. The issues with the interface models in *ANSYS-CFX* have been addressed. The impeller model features no asymmetric downstream component which allows for frozen-rotor methods to be applied to all domain interfaces. The numerical domains such as inlet, impeller and outlet as well as the sidewall gaps need to be created so that the interfaces match perfectly in axial and radial direction. The solver allows for a circumferential misalignment of the interfaces which needs to be stated in the "rotational offset" option. The inlet, outlet and impeller meshes can quickly be generated in *ANSYS-TurboGrid*, where inlet and outlet can be build without boundary layer resolution. The topology of the impeller mesh should be chosen with special care on the trailing edge according to figure 13.1. The resolution at the no-slip walls should be high enough so that the y^+ is in the range of one to ten. The sidewall gaps should be meshed with *ANSYS-ICEM* on a two-dimensional basis and then extruded to the respective size of the three dimensional model.

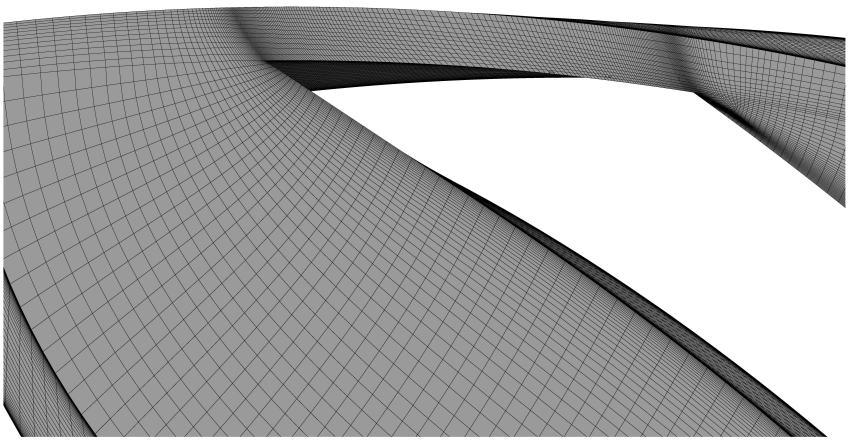

Figure 13.1: Trailing edge mesh refinement

For the full-annulus simulations stationary a frozen-rotor approach between volute and impeller should be chosen. In order to gain a better understanding of the overall performance multiple relative positions to the volute tongue should be investigated. The mixed-out averaging method allows analysis of individual components in case the flow is not allowed to mix out between components. This leads to a clearer dissection and location of losses and performance characteristics of the individual components. The analysis planes should not be located at the interfaces. In case of strong recirculation or large gradients the interfaces create convergence issues between one side and the other. A difference in properties such as velocity and pressure on one side and the next can be the result. The location of the numerical inlet and outlet should be defined at least one impeller radius upstream and downstream of the first and last component. The analysis for the outlet conditions should be performed at one third of the diameter upstream of the numerical outlet. Better results should be expected from transient simulations.

13.3. Recommendations for further research

The findings in this project lead to a number of further questions that should be investigated in following research in order to expand the knowledge on secondary flow paths and improve the existing models.

The methods applied reveal large limitations of steady simulations of volute pumps. In order to get a better understanding and a clearer view of the overall performance full-annulus calculations will always be necessary since the individual components are strongly coupled. When adding the volute to the numerical model unsteady calculations become unavoidable [21] in order to prevent errors originating from interface models in steady simulations. Current investigations by Negishi et. al (2018) [12] showed better agreement to the experimental data of the pump performance with large scale unsteady simulations on fully unstructured meshes. Projects like these with over 40 million cells simulated transient are computationally extremely expensive.

The interfaces at the balance hole injection can lead to convergence issues as well. A possible solution to this problem which is also connected to the problem of incorrect meshing of radial machinery in *ANSYS-TurboGrid*, as discussed and seen in figure 7.4, can be fully unstructured meshing of the geometry also performed by Negishi et. al (2018) [12]. With this approach interface definitions can be avoided, but the relative position to the volute is hard to change.

The investigations on the balance hole injection performed in this project reveal that in some cases the injection can lead to an increase in hydraulic performance thereby effectively reducing the overall efficiency drop due to secondary flow paths. Further investigations on the location and angle at which the leakage flow injection takes place can lead to improved designs of thrust-balanced pumps. Roughness was not modeled in the course of this project, the wall roughness however plays a role when the shear stresses are evaluated. Higher roughness of the rotor wall for example can lead to larger rotational speeds in the side cavities and increase pressure drop and reduce axial thrust and leakage mass flows. Better understanding and trade off analysis between reduced leakage and increased disk friction can further improve the sidewall gap design. The main analysis in this project was performed on secondary flow paths which are open to the volute flow. It is shown that at partload the volute tongue leads to a large injection of secondary flow into the sidewall gaps thereby increasing losses. A better and more common design is presented in the second pump where the sidewall gaps attach directly to the impeller outflow. This allows for a steady increase in rotational velocities entering the sidewall gaps and lower leakage mass flows and disk friction. More impeller designs should be investigated in terms of impact on the sidewall gap flow. As Gülich points out [21] the immediate onset of recirculation can lead to a drastic change in rotation factor and an unbalanced behavior in terms of thrust at partload. The origins of recirculation and change in separation region need to be investigated to improve the inlet assumptions for the existing empirical correlations.

The effects investigated with the different numerical models need further validation with experimental data. Information on static pressure at various locations in the sidewall gaps and leakage mass flow as well disk friction on the rotating wall can give reassurance on the validity of the observed trends and quantities over the operation regime of the pumps.

Further reduction of the sidewall gap models can simplify the process towards estimations on thrust and losses even more. Possible reduced models can be: two-dimensional analysis of the sidewall gaps and sealing paths with adapted inlet and outlet conditions.

A

Appendix

A.1. Y^+-values

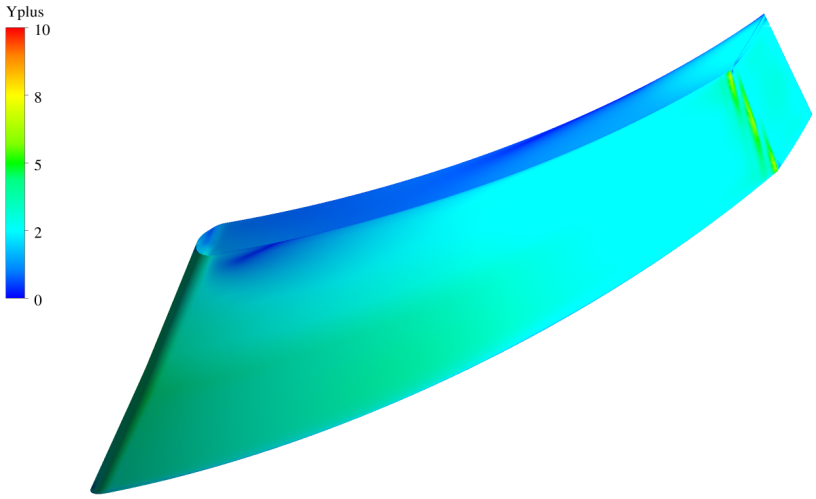

Figure A.1: y^+-value distribution for cell closest to wall at impeller blade pressure side

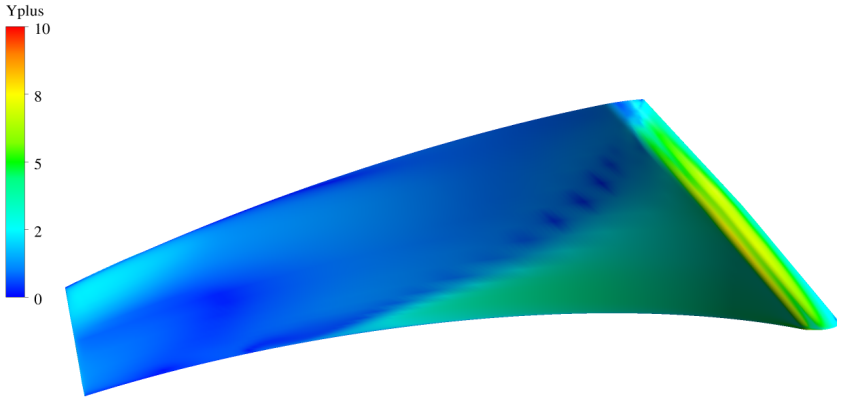

Figure A.2: y^+-value distribution for cell closest to wall at impeller blade suction side

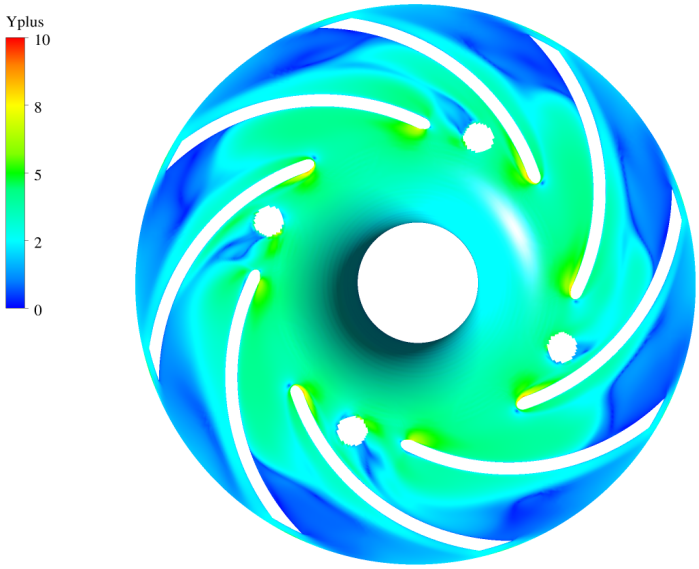

Figure A.3: y^+-value distribution for cell closest to wall at impeller hub

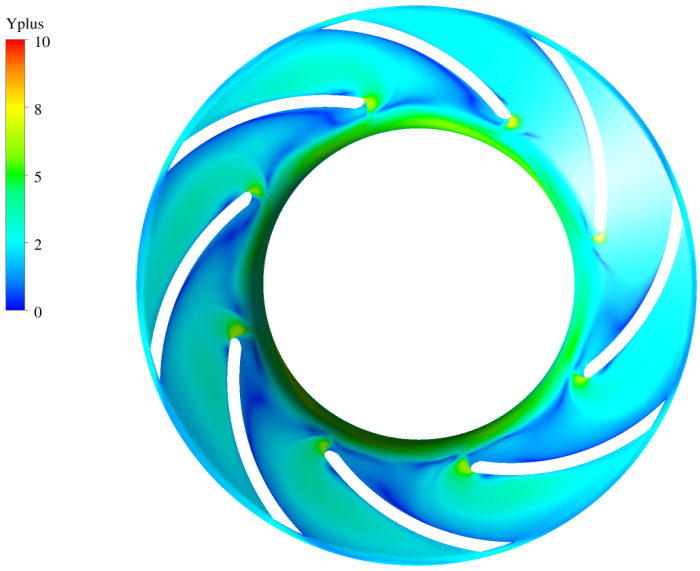

Figure A.4: y^+-value distribution for cell closest to wall at impeller shroud

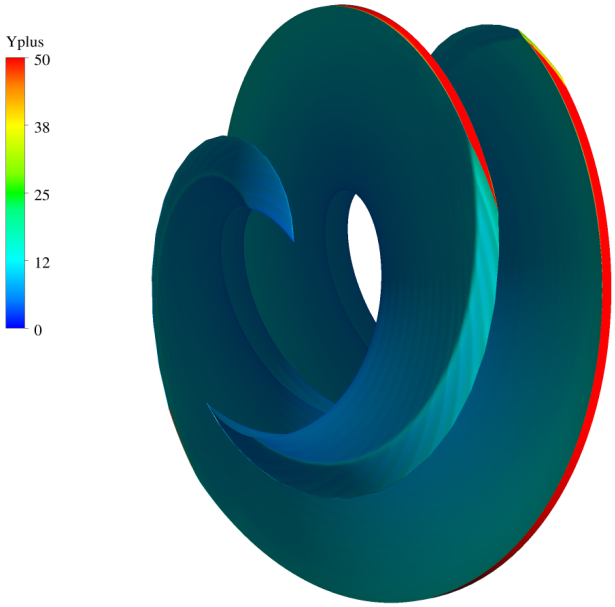

Figure A.5: y^+-value distribution for cell closest to wall at inducer blades

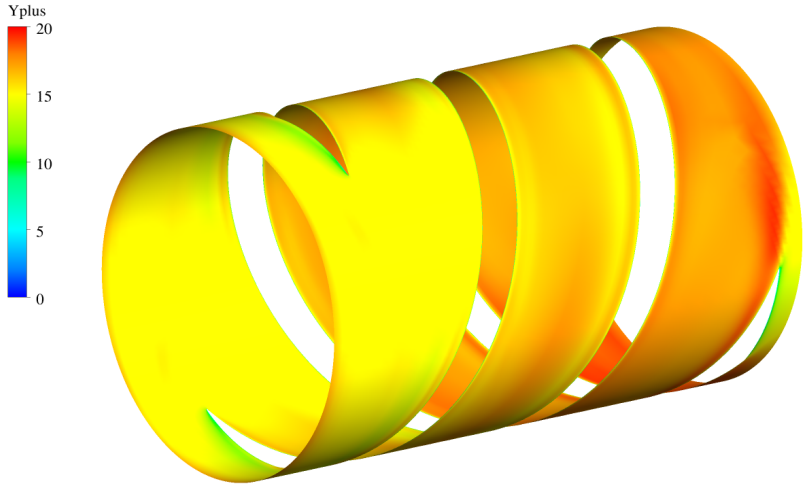

Figure A.6: y^+-value distribution for cell closest to wall at inducer hub

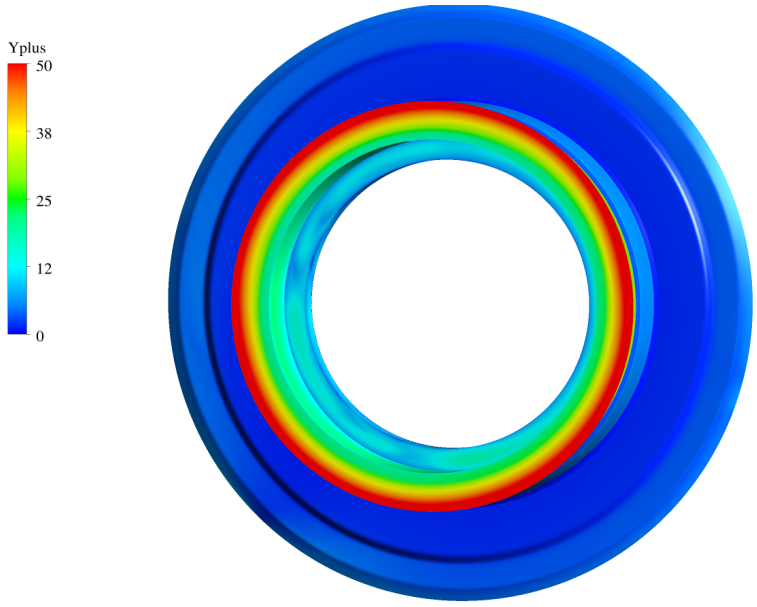

Figure A.7: y^+-value distribution for cell closest to wall at back side leakage path rotor wall

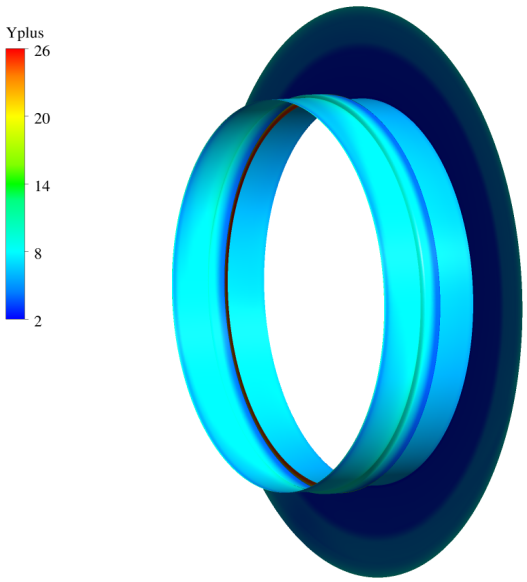

Figure A.8: y^+-value distribution for cell closest to wall at back side leakage path casing wall

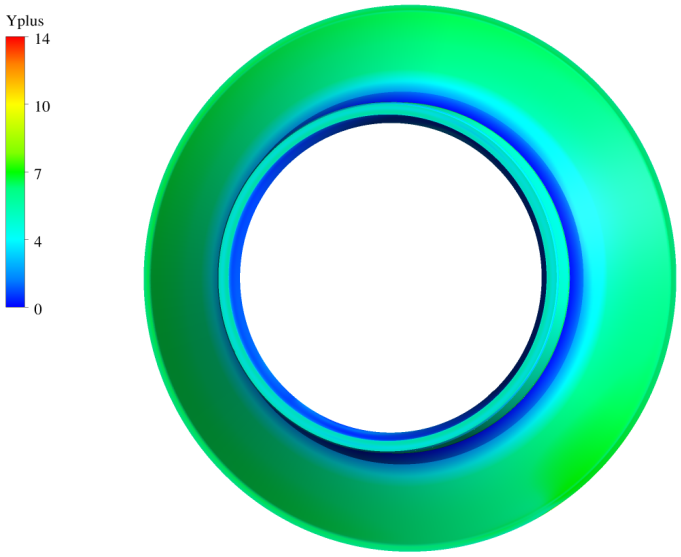

Figure A.9: y^+-value distribution for cell closest to wall at front side leakage path rotor wall

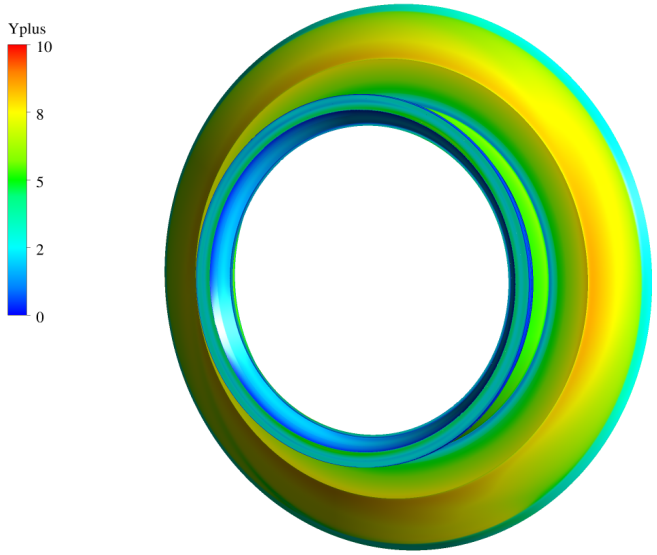

Figure A.10: y^+-value distribution for cell closest to wall at front side leakage path casing wall

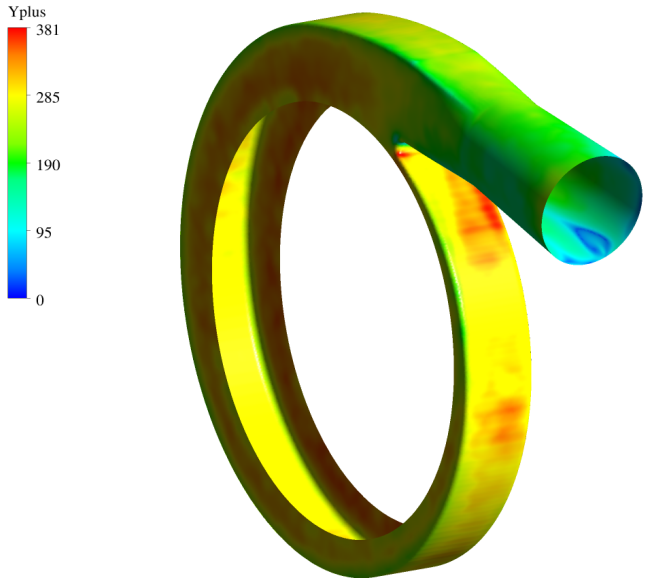

Figure A.11: y^+-value distribution for cell closest to wall at volute wall

Bibliography

[1] Cervone A, Torre L, Pasini A, and d'Agostino L. *Cavitation and Turbopump Hydrodynamics Research at Alta S.P.A. and Pisa University.* 4th International Symposium on Fluid Machinery and Fluid Engineering, 2008.

[2] Shapiro A, H. *The Dynamics and Thermodynamics of Compressible Fluid Flow.* New York, 1953.

[3] Stepanoff A, J. *Pompes centrifuges et pompes h'elices.* Trans. ASME, 1932.

[4] Hu B, Brillert D, Dohmen H, J, and Benra F. *Investigation on the Flow in a Rotor-Stator Cavity with Centripetal Through-Flow.* European Turbomachinery Conference, 2017.

[5] Wagner B. *Untersuchungen zu Sekundärsystemen in Turbopumpen für Flüssigkeitsraketenantriebe.* Deutscher Luft- und Raumfahrtkongress, 2016.

[6] Araz C. *Numerische Charakterisierung und Optimierung des Laufrades einer LOX-Turbopumpe.* TU Munich, 2016.

[7] Bramanti C. *Experimental Study of Cavitation and Flow Instabilities in Space Rocket Turbopumps and Hydrofoils.* Dipartimento di Ingegneria Aerospaziale, Pisa, 2006.

[8] Brennen C, E. *Hydrodynamics of Pumps.* Carlifornia Institute of Technology, 1994.

[9] Greitzer E, M, Tan C, S, and Graf M, B. *Internal Flow.* Cambridge University Press, 2004.

[10] Schneckenberg E. *Durchfluss von Wasser durch Drosselspalt.* Math. Mech, 1931.

[11] Bahm F, U. *Axialschubverhalten von einstufigen Kreiselpumpe mit Spiralgehäuse.* Dissertation University Hannover, 2000.

[12] Negishi H, Ohno S, Ogawa Y, Aoki K, Kobayashi T, Okita K, and Mizuno T. *Numerical Study of Flow Field Characteristics of a Liquid Hydrogen Unshrouded Impeller.* 53rd AIAA/SAE/ASEE Joint Propulsion Conference, 2018.

[13] Schlichting H. *Boundary layer theory, 5th edition.* Verlag Karl Braun, 1965.

[14] Wittel H, Muhs D, Jannasch D, and Voßiek J. *Maschinenelemente.* Springer-Verlag, 2009.

[15] Zilling H. *Untersuchungen des Axialschubes und der Strömungsvorgänge im Radseitenraum einer einstufigen Radialpumpe.* Strömungsmechanik und Strömungsmaschinen Heft 15, 1973.

[16] ANSYS Inc. *CFX-Solver Modeling Guide.* ANSYS Inc., 2018.

[17] Daily J, W and Nece R, E. *Chamber Dimension Effects on Induced Flow and Frictional Resistance of Enclosed Rotating Disks.* Journal of Basic Engineering 82, 1960.

[18] Daily J, W, Ernst W, D, and Asbedian V, V. *Enclosed rotating disks with superposed throughflow.* MIT, Department of Civil Engineering, 1964.

[19] Denton J, D. *Loss Mechanisms in Turbomachines.* IGTI Scholar Lecture, 1993.

[20] Gülich J, F. *Disk friction losses of closed turbomachine impellers.* Springer-Verlag, 2003.

[21] Gülich J, F. *Centrifugal Pumps.* Springer Verlag Berlin, 2010.

[22] Casey M, V and Marty F. *Centrifugal Compressors Design and Off-Design.* Institute of Refrigeration, 1986.

[23] Cumpsty N, A and Horlock J, H. *Averaging Nonuniform Flow for a Purpose.* Journal of Turbomachinery, ASME, 2006.

[24] Maier S. *Betrachtung von Axialschubausgleichsystemen in Turbopumpen für Flüssigkeitsraketenantriebe.* Technical University Munich, 2016.

[25] Poncet S, Chauve M, P, and Le Gal P. *Turbulent rotating disk flow with inward throughflow.* Journal of Fluid Mechanics, 2005.

[26] Zeller S. *Investigation on leakage flow injection on radial impellers.* Technical University Munich, 2016.

[27] Shimura, Kawasaki, Uchiumi, and Kimura. *Internal Flow and Axial Thrust Balancing of a Rocket Pump.* Journal of Fluids Engineering Vol. 134, 2012.

[28] NASA SP-8121. *liquid rocket engine turbopump rotating shaft seal.* Chemical Propulsion, 1978.

[29] Möhring U, K. *Untersuchung des radialen Druckverlaufes und des Drehmomentes im Radseitenraum von Kreiselpumpen bei glatter, ebener Radseitenwand und bei Anwendung von Rückenschaufeln.* TU Braunschweig, 1976.